Tunability of Gas Adsorption Enthalpies in Carbonaceous Materials for Energy-Related Applications

Thesis by
Cullen M. Quine

In Partial Fulfillment of the Requirements for the
Degree of
Doctor of Philosophy

Caltech

CALIFORNIA INSTITUTE OF TECHNOLOGY
Pasadena, California

2023
Defended May 15th, 2023

ACKNOWLEDGEMENTS

I owe most of my research development skills and exposure to the energy storage field to Dr. Jason Graetz and Dr. John Vajo, and I honestly could not have asked for better mentors at the time (who continue to this day to offer both sound scientific and career advice). My work with Jason, John, Adam, Elena, Talya, and Shuoqin shaped much of the way that I conduct research and pursue a positive research environment, and gave me the background I needed to decide to pursue academia. I am grateful to have such a supportive scientific team at Caltech, and especially thank Dr. Hillary Smith and Dr. Nicholas Weadock for mentoring me in the early days of my graduate program and Joel Chacko, Dr. David Boyd, Pedro Guzman for the help in the lab. I enjoyed the daily banter with Vladimir, Elizabeth, Ziyi, and Stefan, and with members of the Faber Lab (Sara, Kevin, Dr. Ben Herran, Dr. Celia Chari, and honorary member Will) during lunchtime and outside of work conversations.

I would not have been able to finish my thesis work without the support of my family (thanks Mom, Dad, Brit, and Nick for always believing in me and supporting my aspirations), and my fantastic friends. My dad also served as a great sounding board for most of my projects, papers, and research proposals. Sofi, Raven, Tom, Brianna, Charlotte, Jackie, and Gabriella, thank you for being there for me when I needed it the most and giving me the support necessary for finishing my program, I am so incredibly grateful for that. I also thank my therapist Dr. Lee Coleman for the time he spent teaching me the tools needed to process my experiences and to work on becoming the best human I can possibly be.

ABSTRACT

Carbonaceous materials provide a porous, high surface area framework for the adsorption of gases through physisorption. Physisorption operates through van der Waals forces, resulting in highly reversible, densified gas storage. The density of adsorbed gas species approaches the bulk liquid density, providing a method to increase the volumetric energy density of hydrogen and natural gas at conditions where the adsorbate is a non-liquid in the bulk phase. This dissertation explores the tunability of the strength of gas adsorption to surfaces of carbon adsorbents, known as the enthalpy of adsorption. Two methods are studied: modification of the surface atomic composition and microstructural changes to the carbon porosity. Applications are considered for both energy storage and carbon capture applications.

The first chapter presents a brief overview of the energy storage field, with emphasis on non-conventional methods to store gases efficiently. Chapter 2 provides the thermodynamic and statistical mechanical derivations used throughout this work, and the assumptions that go into the models used to analyze adsorption data. Chapter 3 reports work on a copper-modified commercial carbon MSC-30 for hydrogen storage, which exhibits an activated dissociative chemisorption desorption feature around ambient temperature. Chapter 4 presents the densification of a novel architected carbon structure, zeolite-templated carbon, for adsorbed natural gas storage. Through the pelletization process, the pore morphology of the underlying adsorbent framework is compressed, resulting in increased adsorption enthalpies with applied

pelletization pressure. Chapter 5 focuses on the tunability of pore structure through potassium hydroxide activation, and the resulting adsorption properties pertinent to carbon dioxide capture from a simulated flue-gas stream. The last chapter provides insight into the work as a whole and identifies areas of future work that would improve the fundamental understanding and broader impact of adsorbent materials.

PUBLISHED CONTENT AND CONTRIBUTIONS

[1] Cullen M. Quine, Hillary L. Smith, Channing C. Ahn, Ariel Hasse-Zamudio, David A. Boyd, and Brent T. Fultz. Hydrogen adsorption and isotope mixing on copper-functionalized activated carbons. *The Journal of Physical Chemistry C*, 126(39):16579–16586, 2022. doi: 10.1021/acs.jpcc.2c02960. URL https://doi.org/10.1021/acs.jpcc.2c02960.
C.M.Q characterized the synthesized materials, performed isotope mixing experiments, and completed the majority of the writing in the manuscript.

[2] Cullen M. Quine, Erin E. Taylor, Atsushi Gabe, Hirotomo Nishihara, Nicholas A. Strange, Channing C. Ahn, Brent T. Fultz, and Nicholas P. Stadie. Compact methane storage and unusual structural properties of ordered microporous carbon monoliths. In preparation. 2023.
C.M.Q conducted methane isotherm measurements, built and analyzed the software required for thermodynamic characterization, and contributed to writing the manuscript.

[3] Cullen M. Quine, Joel Chacko, David A. Boyd, Nicholas P. Stadie, and Brent T. Fultz. Improved multicomponent modelling of gas adsorption using a thermodynamically-consistent software package: REALIST. In preparation. 2023.
C.M.Q conceptualized the project, conducted gas isotherm measurements, synthesized the carbon materials, built and analyzed the software required for thermodynamic characterization, and completed the majority of the writing in the manuscript.

TABLE OF CONTENTS

LIST OF ILLUSTRATIONS

LIST OF TABLES

NOMENCLATURE

Terminology

Description	Definition
q_{st}	Isosteric heat of adsorption, the positive quantity of the enthalpy of adsorption, amount of energy per mole of gas released when gas is adsorbed to an adsorbent at constant uptake
Absolute uptake	The uptake quantity of interest for thermodynamic calculations, includes all of the adsorbed gas (the excess uptake and the gas phase contribution that is in the adsorption volume v_a)
Absorption	Bulk interaction of gas with material
Adsorbate	(Gas) molecule that is being adsorbed
Adsorbent	Material with high surface area that provides adsorption framework
Adsorption	Surface interactions of gas with material
Chemisorption	Chemical adsorption, chemical binding of adsorbate to adsorbent
Excess uptake	The additional adsorbate measured over the gas occupied in an empty vessel at the same thermodynamic conditions due to adsorption
Physisorption	Physical adsorption, non-chemical binding of adsorbate
Total uptake	The amount of gas that occupies a fixed volume completely filled by an adsorbent. Includes the absolute uptake and the void space in the adsorbent that can accomodate non-adsorbed gas molecules.

Symbols

Symbol	Description	Units
α	double-site Langmuir weighting factor	
α_p	electric dipole polarizabilities	cm^3
β	thermodynamic temperature $(1/k_\mathrm{B}T)$	$1/kJ$
χ_i	adsorbed gas mole fraction of species i	
Δh_{ads}	enthalpy of adsorption	kJ/mol
Γ_i	number of non-interacting adsorption sites of site i	
Γ_t	total number of non-interacting adsorption sites	

$\hbar\omega$	adsorption vibrational energy	meV
λ_g	ideal gas thermal de Broglie wavelength	Å
λ_ads	adsorbed thermal de Broglie wavelength	Å
μ_i	chemical potential of site i	kJ/mol
ϕ	fugacity coefficient	
Φ_{LJ}	Lennard-Jones potential	eV/atom
π	spreading pressure	J/m^2
ρ_skel	adsorbate skeletal density	$g\,mL^{-1}$
ρ_g	gas phase molar density	mmol/mL
σ_{LJ}	adsorbate-adsorbent van der Waals diameter	
θ	fraction of occupied lattice sites	
ε_i	binding energy of site i	kJ/mol
ε_{LJ}	Lennard-Jones binding energy	eV/atom
Ξ	total grand canonical partition function	
ξ_i	grand canonical partition function with adsorption site i	
$A_{\mathrm{B},i}$	adsorption area of binding site i	Å^2
A_i	specific surface area occupied by species i	m^2/g
A_T	adsorbed gas coverage of all adsorbed species	m^2/g
A_i	temperature-independent Langmuir constant prefactor of site i	$\sqrt{K}/MPa$
f	fugacity	MPa
G	Gibbs free energy	kJ
k_B	Boltzmann's constant	J/K
K_c	Langmuir constant of chemisorbed site	1/MPa
$K_{\mathrm{p},i}$ or K_i	Langmuir constant of physisorbed site i	1/MPa
N	number of particles	particles
n_a	specific absolute adsorption uptake	mmol/g
n_i	specific absolute adsorbed gas of species i	mmol/g

n_i^0	pure component absolute uptake	mmol/g
n_e	specific excess uptake	mmol/g
n_m	maximum specific absolute uptake	mmol/g
$n_{e,v}$	specific volumetric excess uptake	V_{STP}/V
$n_{t,v}$	specific volumetric total uptake	V_{STP}/V
P	pressure	MPa
p_i	partial presure of species i	MPa
p_i^0	pure component partial presure of species i	MPa
q_i	partition function of site i	
$q_{st,0}$	specific zero-coverage isosteric heat of adsorption	kJ/mol
s_a	adsorbed phase specific entropy	J/K
s_g	gas phase specific entropy	J/K
S_{mix}	entropy of mixing	J/K
T	temperature	K
v_{bulk}	specific bulk adsorbent volume	mL/g
$v_{g,\,STP}$	specific gas volume at 273K, 0.1 MPa	mL/g
v_{pore}	specific pore volume	mL/g
v_{skel}	specific skeletal volume	mL/g
v_a	adsorbed specific gas volume	mL/g
v_m	maximum adsorbed specific gas volume	mL/g
v_{N_2}	specific pore volume measured with 77 K nitrogen	mL/g
X_{pore}	void fraction of bulk adsorbent material	
y_i	gas phase mole fraction of species i	
m	mass	kg

C h a p t e r 1

INTRODUCTION

"As the saying goes, the Stone Age did not end because we ran out of stones; we transitioned to better solutions. The same opportunity lies before us with energy efficiency and clean energy."

— Dr. Steven Chu

The societal demand for higher energy density fuels and energy storage leads to an interesting set of challenges: the more densely the energy is stored, the bigger the risk of catastrophic (and spectacular) failure. For high pressure compressed gas systems in transportation, the DOE has required the tanks to pass bullet penetration tests to alleviate concerns. The ultimate challenge of energy storage is: how can we balance the competing requirements of safety and energy density for use in everyday service?

Gases are notoriously difficult to pack efficiently in volume, however they have the highest energy densities by mass of any conventional fuel. Most of the fuels (hydrocarbons) used for transportation work under combinations of two extremes of combustion reactions:

$$H_2(g) + 0.5O_2(g) = H_2O(g) \quad \Delta H^0 = -120 \, \text{kJ}/\text{g}_{\text{H2}} \tag{1.1}$$

$$C(s) + O_2(g) = CO_2(g) \quad \Delta H^0 = -32.7 \, \text{kJ}/\text{g}_{\text{C}}. \tag{1.2}$$
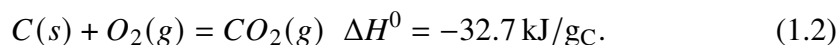
The second reaction involving the combustion of carbon in particular has attracted
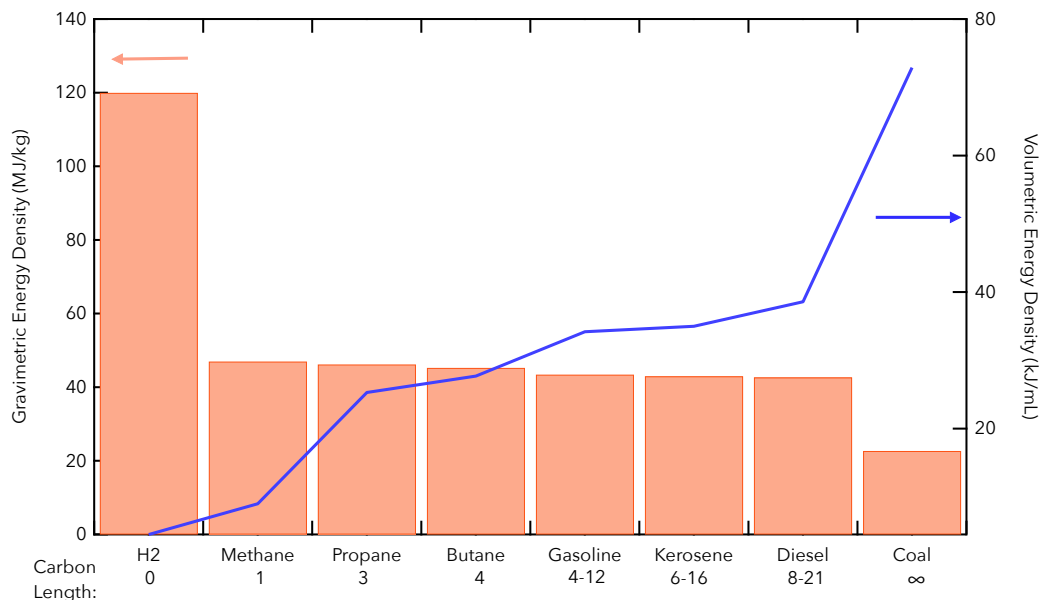
Figure 1.1: Gravimetric and volumetric energy density of conventional fuels plotted with increasing carbon content.

significant interest due to concern about climate change. Fuels that are commonly used for energy production or storage are shown in Figure 1.1, with increasing carbon content on the x-axis. Hydrogen has the highest gravimetric energy density of any conventional fuel, however one of the lowest volumetric energy densities at ambient conditions. Due to the nature of hydrogen molecules, hydrogen liquefies at much lower temperatures than other fuels, requiring high pressures to store densified hydrogen in gas cylinders. With increasing length of the linear hydrocarbon alkane chain, the carbon-to-hydrogen ratio approaches 2:1, reducing the gravimetric energy density of these fuels. However, with increasing hydrocarbon chain length, the interaction strength between molecules increases, resulting in raising the boiling point temperature. Most fuels used for terrestrial applications are either liquids or pressurized gases operating near their boiling point at ambient temperature ($\approx$ 298 K). Both propane and butane can be liquefied at reasonable pressures under

ambient temperature, resulting in a significant increase in volumetric energy storage because liquids generally having three orders of magnitude higher density than gases below the critical point. Gasoline, diesel, and kerosene are liquids under ambient temperature and pressure, making tank design significantly easier than for a pressurized gas, allowing ease of use for passenger vehicles.

While the higher carbon content hydrocarbons pack efficiently due to liquid densities, there has been increased concern with CO_2 emissions from these fuels. To mitigate the CO_2 emissions from fuels, two direct approaches can be implemented:

- Increase the energy density of lower-carbon content fuels (hydrogen, methane), resulting in less CO_2 per unit energy,

- Capture CO_2 from high carbon content fuels to prevent its release.

This thesis explores both of these approaches through thermodynamics of an interesting and versatile subset of materials: carbon adsorbents.

1.1 Adsorption for Energy-Related Applications

While hydrogen and methane suffer from low volumetric energy density in empty tanks due to weak molecular interactions, materials can be added to increase the volumetric packing of these fuels. Adsorption is the physical property concerned with the favorable interaction of molecules (adsorbates) with the surface of molecules (adsorbents). Some of the first recorded use of adsorbents dates back to before 1500 B.C, for the removal of vapors from infected wounds.[1] However, the main framework needed to describe the principles of adsorption accurately was

developed in the late nineteenth and early twentieth century. J. Willard Gibbs' work on defining phase equilibria boundaries was essential in defining experimentally measured adsorption uptake.[2] Irving Langmuir pioneered the thermodynamic framework used to model gas adsorption in materials that we still use today (to varying degrees and levels of success).[3–5] *Ad*sorption is purely a surface phenomenon (unlike bulk diffusion processes in *ab*sorption), which means that measured adsorption properties are highly sensitive to atomically thin layers of materials, their geometric structure, and surface chemical composition. It is this sensitivity and tunability of these porous materials which is the ultimate focus of this thesis.

Hydrogen for Renewable Energy Storage

Hydrogen has the highest gravimetric energy density of any chemical fuel, however high pressures or cryogenic temperatures are needed for vehicular applications. Some applications justify the high cryogenic costs to liquefy hydrogen (20 K), however most vehicle technologies have settled on high pressure tanks.[6, 7] Hydrogen is also one of the only fuels that has viable paths to being carbon neutral, including electrolysis of water (green hydrogen) or reforming of methane with carbon capture/utilization (blue/turquoise).[8] State-of-the-art storage mechanisms for vehicles involve costly high pressure gas cylinders that are resistant to armor-piercing bullets to ease public fears about the use of hydrogen in vehicles. Even with these feats of engineering, volumetric energy densities are still low compared to gasoline vehicles. Hydrogen has attracted recent interest as a sustainable clean-energy fuel for grid-scale backup and seasonal storage to transition away from fossil fuels.[9]

Novel adsorbent materials and metal hydrides have been studied extensively, which improve storage characteristics of hydrogen under certain conditions.

There are many studies of solid hydrogen storage materials to enhance storage densities at lower pressures than conventional pressure vessels.[10] Current hydrogen storage materials can be broken down into two main categories: absorbents and adsorbents. Absorption occurs upon bulk diffusion of hydrogen into the structures of materials, and has two subcategories: metal-hydrides, and chemical hydrides. Metal-hydrides systems have been shown to be reversible at ambient conditions. However, a reversible hydride that exhibits both high capacity and low desorption temperatures for hydrogen release has remained elusive. Iron-titanium metal-hydride systems and rare-earth hydrides (e.g., LaNiSn) are cyclable at ambient temperature and reasonable pressures, however low gravimetric uptake (3 wt. %) limit use to stationary applications.[11, 12] Magnesium-based hydrides have high gravimetric hydrogen uptake (7.6 wt%) but suffer from regenerability issues and require high desorption temperatures (700 K) due to sluggish kinetics.

Current work has focused on changing the structure and composition of magnesium-based hydride systems to address these challenges.[13] Chemical hydrides, such as the metastable hydride alane (AlH_3) or ammonia borane complexes are irreversible, but have high gravimetric energy densities (>10 wt% hydrogen storage) and have rapid hydrogen release temperatures near ambient conditions.[14]

Adsorbents, which include metal-organic frameworks (MOFs), covalent organic frameworks (COFs), zeolites, and carbonaceous materials, mostly suffer from weak interactions with hydrogen, limiting their use to cryogenic temperatures (77 K). While adsorption materials show a linear trend of uptake with surface area at low pressures (known as Chahine's rule)[15], hydrogen uptake in adsorbents near ambient temperature is much more sensitive to surface functionalization and pore structure than accessible surface area.[16] Metal-organic frameworks (such as MOF-5 and Ni_2(m-dobdc)) have some of the highest volumetric hydrogen uptake of any physisorbent at 77 K and 298 K.[17, 18]

Ironically, all of the studied materials surround the conditions needed for hydrogen storage for mobile applications on Earth, as shown in Figure 1.2. The few materials that do fall within the DOE system target range are either non-reversible or are chemical systems which can poison fuel cells with ammonia or diborane. There is a clear distinction in the plot, as adsorbents work at temperatures too low of relevance for vehicle hydrogen storage, and absorbents require high desorption temperatures above ambient conditions. Current work has focused on destabilization of metal hydrides to decrease the desorption temperature in metal hydride systems,[19, 20] or enhanced binding energy in adsorbents to increase the adsorption temperatures towards ambient conditions.

Methane for Heavy Duty Transportation

Compressed natural gas vehicles (CNG) have been commercially available for decades, but have much less range than their gasoline counterparts due to poor
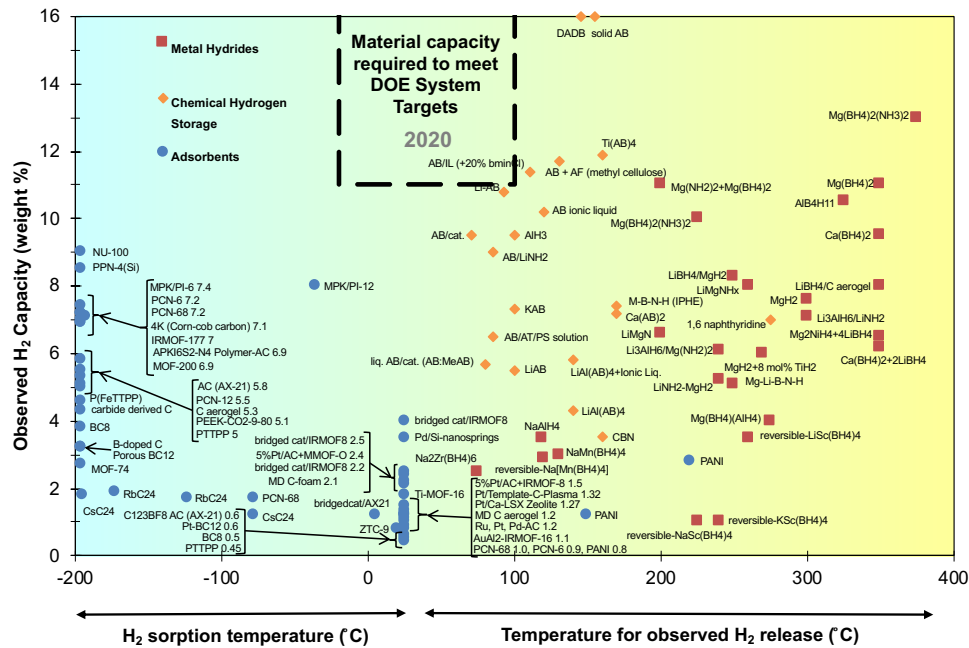
Figure 1.2: Plot of current hydrogen storage materials (Image courtesy of Dr. Channing Ahn and the U.S. Department of Energy).

volumetric storage densities. A typical CNG passenger vehicle (2012 Honda Civic) has less than half of the range of its gasoline counterpart.[21] Natural gas is in the unique position to be a "transition" fuel between fossil fuel and more carbon-neutral options due to the option of renewable natural gas (RNG) production.[22, 23] Methane, the primary component in natural gas, has the least amount of carbons per hydrogen of any hydrocarbon fuel, meaning that it releases the least amount of CO_2 per mass of fuel out of all carbon-containing fuels. CNG storage suffers from the main setbacks as hydrogen tanks: high storage pressures (250 bar) result in large compression costs, complex tank design, and potential safety risks. Liquefied natural gas at 111 K is more reasonable than the 20 K required for hydrogen storage, however it is still energy intensive and is not being considered for mobile applications.[24]

The primary issue with compressed natural gas (CNG) vehicles is the tank space required to store sufficient amounts of natural gas (see Figure 1.3). Lowering the fueling pressure lowers compression costs, and also reduces the size and complexity of the tank required. Adsorbed natural gas (ANG) technology provides liquid-like densities of methane at lower pressures than CNG and higher temperatures than LNG. Zeolites, while having high affinity for methane molecules, have low gravimetric micropore volume and specific surface area, as well as low volumetric capacities due to large void volumes. Carbon materials have reasonable methane uptake, but pore size variability, low packing density, and lack of tunability have historically limited carbons to low volumetric uptakes.[25, 26] Zeolite-templated carbons (ZTCs) have shown large specific surface areas and narrow distributions of pore sizes in the right range for methane storage, but still have low volumetric powder packing.[27, 28] MOFs have shown some of the highest adsorbed natural gas volumetric uptake numbers, especially at pressures up to 65 bar, and hold the highest records for methane storage, either with compacted powder monolithic pellets [29, 30] or assuming ideal crystal packing of the powder.[31, 32] However, many MOFs exhibit instabilities in the presence of moisture, a non-negligible component of real natural gas mixtures.[33–36]

Fuel Tank   Removable
Divider

Figure 1.3: Trunk of a Honda Civic showing an 8 gasoline gallon equivalent CNG tank with remaining space. (Source: Honda) [39]

The primary metric for volumetric methane storage is the deliverable volumetric uptake. This assumes a delivery pressure of 5 bar, meaning that any adsorbed gas below 5 bar is unusable in an actual system (without a system compressor). [37, 31] Research in this area of gas storage should be aimed at increasing uptake above 5 bar and minimizing uptake below this pressure. One group of novel materials being developed include flexible metal-organic frameworks, which minimize uptake below 5 bar through a reversible collapse of pore structure.[38]

Carbon Capture and Utilization

Due to energy consumption since the industrial revolution, carbon dioxide content in the atmosphere has increased. This has led to increasing calls for both the removal and sequestration of carbon dioxide to reduce atmospheric greenhouse gases. Power plants have remained one of the main sources as 1.5 gigatons of CO_2

Carbon Dioxide Flow Directions

| CO$_2$ source | CO$_2$ Capture route | Compression and Transport | CO$_2$ conversion site |

CO$_2$ source

- Pressure: 1 bar
- Temperature: 50-75°C
- CO$_2$ concentration: 3-30%
- Major impurities: N$_2$, O$_2$, H$_2$O
- Other impurities: NO$_x$, SO$_x$

- Coal-driven Power Plant
- Cement Plant
- Iron & Steel Plant
- Oil Refinery

- Pressure: 15-40 bar
- Temperature: 40-450°C
- CO$_2$ concentration: 15-40%
- Major impurities: CH$_4$, CO, H$_2$
- Other impurities: NO$_x$, H$_2$S, SO$_x$

- Natural Gas Field
- Gasification Plant
- H$_2$ production plant

- Pressure: 1 bar
- Temperature: 50-75°C
- CO$_2$ concentration: 75-80%
- Major impurities: H$_2$O
- Other impurities: NO$_x$, SO$_x$

- Oxy-combustion Plant

CO$_2$ capture from stationary points

- Pressure: 1 bar
- Temperature: Ambient temperature
- CO$_2$ concentration: ~400ppm
- Major impurities: N$_2$, O$_2$
- Other impurities: -

- Atmosphere

Air CO$_2$ capture

CO$_2$ Capture route

CO2 absorption
- Ammonia
- Ionic liquid
- Piperazine
- Alkaline solutions
- Amine based solvents

CO2 adsorption
- MOFs
- Zeolites
- Metal oxides
- Amine-grafted solids

CO2 membrane separation
- Organic membranes
- Inorganic membranes
- Mixed matrix membranes
- Composite membranes

CO$_2$

Other gases

CO$_2$ conversion site

Thermochemical conversion plants

Biochemical Plants

Photochemical Plants

Electrochemical Plants

Figure 1.4: Overview of some of the currently investigated CO$_2$ technologies and input gas compositions for carbon capture.[41]

were released in 2021 solely from coal and natural gas power plants.[40] While many developed countries have focused on mitigation through cleaner energy production, the use of coal, oil, and natural gas remains the predominant form of global energy production.

The development of any technology at the scale required for carbon capture on a statistically meaningful level requires the use of low cost and sustainable materials or engineered materials that are highly reusable. Carbon dioxide is similar to hydrogen in that there are adsorbents that can chemically or physically bond (and release) the gas. However, the challenge is significantly different owing to the need for high CO$_2$ uptake at very low partial pressures in the case of carbon capture.

Unlike other adsorption applications, carbon capture systems have the unique challenge of requiring selective adsorption of one species in a multi-component mixture of gases. Technologically relevant gas mixtures with CO_2 capture technologies are shown in Figure 1.4. Direct air capture (DAC) focuses on removing the 420 ppm of carbon dioxide from ambient conditions using such chemically selective materials. This capture technology is some of the only commercialized systems currently deployed for carbon capture, however it is very energy intensive due to the high entropic penalty of concentrating such a dilute gas stream. Point sources, such as power plants, offer much higher CO_2 concentrations (3-40%) over a large range of pressures and temperatures. The trade-off is requiring technology to be used in a specific place or setting, making adoption more challenging. Unlike dilute atmospheric capture, point source capture has lower demands for selectivity. MOFs are also being considered for point source capture, however due to the high water content of the gas stream, careful selection and design of MOFs must be made to use these materials for point source capture. Recent advances in MOFs for carbon dioxide capture have focused on reducing water uptake, scalability, and cost, such as CALF-20 [42] or aluminum formate [43]. While having the lowest uptake of the adsorbents, zeolite-based materials are low cost options with high selectivity for carbon dioxide.

Adsorption of carbon dioxide using carbon materials is much weaker than the chemically-bonded equivalents such as amine solvents. However, amines require significant energy input for regeneration, and activated carbon-based adsorbents

show promising characteristics for post-combustion carbon capture applications.[44]
The interaction potential of CO_2 with carbon is much stronger than for other gases,
increasing the gas binding energy in carbon adsorbents. Carbon materials have the
additional benefit over other capture technologies of being potentially sustainable
(and carbon-negative) with the right starting bio-derived material. The activation
of biochar to produce porous carbon adsorbents is a very mature and well studied
field.[45] Commercial activated carbons are generally physically activated with
CO_2 or steam due to cost and scalability, however chemically-activated carbons
exhibit higher specific surface areas, tunable pore structure, and higher yields.[46]
Chemical activation uses activation agents such as potassium hydroxide, potassium
chloride, potassium carbonate, sodium hydroxide, or phosphoric acid to react with
the carbon to form porous materials.[47, 46] The alkali hydroxides in particular,
such as KOH, remove graphitic carbon layers through an intercalation process,[48]
allowing for the selective development and tunability of micropores with varying
activation conditions.[49]

Summary of Adsorption Applications

Due to the interaction of gases with the surfaces of materials, it is possible
to either increase the volumetric density of gases at lower pressures, or adsorb
preferentially certain gas species over others. Reducing the system pressure to store
a fixed amount of gas reduces the complexity and cost of tank design. For low-
carbon fuels such as hydrogen and methane, this directly corresponds to increased
energy densities. The selective capture of certain gas species has applications for

carbon capture, where a dilute concentration of CO_2 needs to be removed from a gas stream. The strength of the gas binding to the adsorbent affects both the gas storage and the degree of gas selectivity. This thesis explores the tunability of binding energy in adsorbents through metal additions and microstructural changes in carbon to optimize gas storage and carbon capture. Improved statistical mechanical models are developed to characterize the thermodynamic properties, and to predict adsorption phenomena.

References

[1] Ferhan Çeçen and Özgür Aktaş. Water and Wastewater Treatment: Historical Perspective of Activated Carbon Adsorption and its Integration with Biological Processes. In *Activated Carbon for Water and Wastewater Treatment*, pages 1–11. 2011. doi: 10.1002/9783527639441.ch1. URL `https://onlinelibrary.wiley.com/doi/10.1002/9783527639441.ch1`.

[2] Josiah Willard Gibbs. On the equilibrium of heterogeneous substances. *American Journal of Science and Arts*, s3-16:441–458, 1878.

[3] Hans Swenson and Nicholas P. Stadie. Langmuir's theory of adsorption: A centennial review. *Langmuir*, 2019. ISSN 15205827. doi: 10.1021/acs.langmuir.9b00154. URL `https://pubs.acs.org/doi/full/10.1021/acs.langmuir.9b00154`.

[4] Irving Langmuir. The constitution and fundamental properties of solids and liquids. II. Liquids. *Journal of the American Chemical Society*, 39(9):1848–1906, 11 1917. ISSN 15205126. doi: 10.1021/ja02254a006. URL `https://pubs.acs.org/doi/abs/10.1021/ja02268a002`.

[5] Irving Langmuir. The adsorption of gases on plane surfaces of glass, mica and platinum. *Journal of the American Chemical Society*, 40(9):1361–1403, 1918. ISSN 15205126. doi: 10.1021/ja02242a004. URL `https://pubs.acs.org/doi/10.1021/ja02242a004`.

[6] Daigoro Mori and Katsuhiko Hirose. Recent challenges of hydrogen storage technologies for fuel cell vehicles. *International Journal of Hydrogen Energy*, 34(10):4569–4574, 5 2009. ISSN 03603199. doi: 10.1016/j.ijhydene.2008.07.115. URL `https://www.sciencedirect.com/science/article/pii/S0360319908009439`.

[7] Ulrich Eberle, Michael Felderhoff, and Ferdi Schüth. Chemical and physical solutions for hydrogen storage. *Angewandte Chemie - International Edition*, 48(36):6608–6630, 8 2009. ISSN 14337851. doi: 10.1002/anie.200806293. URL https://onlinelibrary.wiley.com/doi/full/10.1002/anie.200806293.

[8] Jad Diab, Laurent Fulcheri, Volker Hessel, Vandad Rohani, and Michael Frenklach. Why turquoise hydrogen will be a game changer for the energy transition. *International Journal of Hydrogen Energy*, 47(61):25831–25848, 7 2022. ISSN 03603199. doi: 10.1016/j.ijhydene.2022.05.299. URL https://www.sciencedirect.com/science/article/pii/S0360319922024983.

[9] Jacqueline A. Dowling, Katherine Z. Rinaldi, Tyler H. Ruggles, Steven J. Davis, Mengyao Yuan, Fan Tong, Nathan S. Lewis, and Ken Caldeira. Role of Long-Duration Energy Storage in Variable Renewable Electricity Systems. *Joule*, 4 (9):1907–1928, 9 2020. ISSN 25424351. doi: 10.1016/j.joule.2020.07.007.

[10] Yijing Huang, Yonghong Cheng, and Jinying Zhang. A review of high density solid hydrogen storage materials by pyrolysis for promising mobile applications. *Industrial and Engineering Chemistry Research*, 60(7): 2737–2771, 2 2021. ISSN 15205045. doi: 10.1021/acs.iecr.0c04387. URL https://pubs.acs.org/doi/full/10.1021/acs.iecr.0c04387.

[11] James J. Reilly and Richard H. Wiswall. Formation and properties of iron titanium hydride. *Inorganic Chemistry*, 13(1):218–222, 1 1974. ISSN 1520510X. doi: 10.1021/ic50131a042. URL https://pubs.acs.org/doi/abs/10.1021/ic50131a042.

[12] Mykhaylo V. Lototskyy, Volodymyr A. Yartys, Bruno G. Pollet, and Robert C. Bowman. Metal hydride hydrogen compressors: A review. *International Journal of Hydrogen Energy*, 39(11):5818–5851, 4 2014. ISSN 03603199. doi: 10.1016/j.ijhydene.2014.01.158. URL https://www.sciencedirect.com/science/article/pii/S0360319914002389.

[13] Indra P. Jain, Chhagan Lal, and Ankur Jain. Hydrogen storage in Mg: A most promising material. *International Journal of Hydrogen Energy*, 35 (10):5133–5144, 5 2010. ISSN 03603199. doi: 10.1016/j.ijhydene.2009.08.088. URL https://www.sciencedirect.com/science/article/pii/S0360319909013615.

[14] Jason Graetz, James J. Reilly, Volodymyr A. Yartys, Jan P. Maehlen, Boris M. Bulychev, Vladimir E. Antonov, Boris P. Tarasov, and Igor E. Gabis. Aluminum hydride as a hydrogen and energy storage material: Past, present and future. *Journal of Alloys and Compounds*, 509(SUPPL. 2):S517–S528, 9 2011. ISSN 09258388. doi: 10.1016/j.jallcom.2010.11.115. URL https://www.sciencedirect.com/science/article/pii/S0925838810028781.

[15] Richard Chahine and Tapan K. Bose. Characterization and optimization of adsorbents for hydrogen storage. *Hydrogen Energy Progress*, 2:1259–1264, 1996.

[16] Seung Jae Yang, Ji Hyuk Im, Hirotomo Nishihara, Haesol Jung, Kunsil Lee, Takashi Kyotani, and Chong Rae Park. General relationship between hydrogen adsorption capacities at 77 and 298 K and pore characteristics of the porous adsorbents. *Journal of Physical Chemistry C*, 116(19):10529–10540, 5 2012. ISSN 19327447. doi: 10.1021/jp302304w. URL `https://pubs.acs.org/doi/abs/10.1021/jp302304w`.

[17] Alauddin Ahmed, Saona Seth, Justin Purewal, Antek G. Wong-Foy, Mike Veenstra, Adam J. Matzger, and Donald J. Siegel. Exceptional hydrogen storage achieved by screening nearly half a million metal-organic frameworks. *Nature Communications*, 10(1), 2019. ISSN 20411723. doi: 10.1038/s41467-019-09365-w. URL `http://dx.doi.org/10.1038/s41467-019-09365-w`.

[18] Matthew T. Kapelewski, Tomče Runčevski, Jacob D. Tarver, Henry Z.H. Jiang, Katherine E. Hurst, Philip A. Parilla, Anthony Ayala, Thomas Gennett, Stephen A. Fitzgerald, Craig M. Brown, and Jeffrey R. Long. Record High Hydrogen Storage Capacity in the Metal-Organic Framework Ni2(m-dobdc) at Near-Ambient Temperatures. *Chemistry of Materials*, 30(22):8179–8189, 11 2018. ISSN 15205002. doi: 10.1021/acs.chemmater.8b03276. URL `https://pubs.acs.org/doi/full/10.1021/acs.chemmater.8b03276`.

[19] John J. Vajo, Florian Mertens, Channing C. Ahn, Robert C. Bowman, and Brent Fultz. Altering hydrogen storage properties by hydride destabilization through alloy formation: LiH and MgH 2 destabilized with Si. *Journal of Physical Chemistry B*, 108(37):13977–13983, 9 2004. ISSN 15206106. doi: 10.1021/jp040060h. URL `https://pubs.acs.org/doi/full/10.1021/jp040060h`.

[20] John J. Vajo, Tina T. Salguero, Adam F. Gross, Sky L. Skeith, and Gregory L. Olson. Thermodynamic destabilization and reaction kinetics in light metal hydride systems. *Journal of Alloys and Compounds*, 446-447:409–414, 10 2007. ISSN 09258388. doi: 10.1016/j.jallcom.2007.02.080. URL `https://www.sciencedirect.com/science/article/pii/S0925838807005063`.

[21] US Department of Energy. Compare Side-by-Side, 2015. URL `https://www.fueleconomy.gov/feg/Find.do?action=sbs&id=31186&id=32336`.

[22] Thomas Amon, Barbara Amon, Vitaliy Kryvoruchko, Andrea Machmüller, Katharina Hopfner-Sixt, Vitomir Bodiroza, Regina Hrbek, Jürgen Friedel, Erich Pötsch, Helmut Wagentristl, Matthias Schreiner, and Werner Zollitsch. Methane production through anaerobic digestion of various energy crops grown in sustainable crop rotations. *Bioresource Technology*, 98(17): 3204–3212, 12 2007. ISSN 09608524. doi: 10.1016/j.biortech.2006.07.

007. URL `https://www.sciencedirect.com/science/article/pii/S0960852406003117`.

[23] Heng Rao, Luciana C. Schmidt, Julien Bonin, and Marc Robert. Visible-light-driven methane formation from CO2 with a molecular iron catalyst. *Nature*, 548(7665):74–77, 8 2017. ISSN 14764687. doi: 10.1038/nature23016. URL `http://www.nature.com/articles/nature23016`.

[24] Alternative Fuels Data Center: Natural Gas Fuel Basics. *US Department of Energy*, 2013. URL `https://afdc.energy.gov/fuels/natural_gas_basics.html`.

[25] D. Lozano-Castelló, J. Alcañiz-Monge, M. A. De La Casa-Lillo, D. Cazorla-Amorós, and A. Linares-Solano. Advances in the study of methane storage in porous carbonaceous materials. *Fuel*, 81(14):1777–1803, 9 2002. ISSN 00162361. doi: 10.1016/S0016-2361(02)00124-2. URL `https://www.sciencedirect.com/science/article/pii/S0016236102001242`.

[26] V. C. Menon and S. Komarneni. Porous adsorbents for vehicular natural gas storage: A review. *Journal of Porous Materials*, 5(1):43–58, 1 1998. ISSN 13802224. doi: 10.1023/A:1009673830619. URL `https://link.springer.com/article/10.1023/A:1009673830619`.

[27] Nicholas P. Stadie, Maxwell Murialdo, Channing C. Ahn, and Brent Fultz. Unusual entropy of adsorbed methane on zeolite-templated carbon. *Journal of Physical Chemistry C*, 119(47):26409–26421, 11 2015. ISSN 19327455. doi: 10.1021/acs.jpcc.5b05021. URL `https://pubs.acs.org/doi/abs/10.1021/acs.jpcc.5b05021`.

[28] Nicholas Stadie. *Synthesis and thermodynamic studies of physisorptive energy storage materials*. PhD thesis, 2013. URL `http://thesis.library.caltech.edu/7198/`.

[29] Tian Tian, Zhixin Zeng, Diana Vulpe, Mirian E. Casco, Giorgio Divitini, Paul A. Midgley, Joaquin Silvestre-Albero, Jin Chong Tan, Peyman Z. Moghadam, and David Fairen-Jimenez. A sol-gel monolithic metal-organic framework with enhanced methane uptake. *Nature Materials*, 17(2):174–179, 2 2018. ISSN 14764660. doi: 10.1038/NMAT5050. URL `https://www.nature.com/articles/nmat5050`.

[30] B. M. Connolly, M. Aragones-Anglada, J. Gandara-Loe, N. A. Danaf, D. C. Lamb, J. P. Mehta, D. Vulpe, S. Wuttke, J. Silvestre-Albero, P. Z. Moghadam, A. E.H. Wheatley, and D. Fairen-Jimenez. Tuning porosity in macroscopic monolithic metal-organic frameworks for exceptional natural gas storage. *Nature Communications*, 10(1):1–11, 2019. ISSN 20411723. doi: 10.1038/s41467-019-10185-1. URL `http://dx.doi.org/10.1038/s41467-019-10185-1`.

[31] Yang Peng, Vaiva Krungleviciute, Ibrahim Eryazici, Joseph T. Hupp, Omar K. Farha, and Taner Yildirim. Methane storage in metal-organic frameworks: Current records, surprise findings, and challenges. *Journal of the American Chemical Society*, 135(32):11887–11894, 8 2013. ISSN 00027863. doi: 10.1021/ja4045289. URL `https://pubs.acs.org/doi/abs/10.1021/ja4045289`.

[32] Zhijie Chen, Mohammad Rasel Mian, Seung Joon Lee, Haoyuan Chen, Xuan Zhang, Kent O. Kirlikovali, Sarah Shulda, Patrick Melix, Andrew S. Rosen, Philip A. Parilla, Thomas Gennett, Randall Q. Snurr, Timur Islamoglu, Taner Yildirim, and Omar K. Farha. Fine-tuning a robust metal-organic framework toward enhanced clean energy gas storage. *Journal of the American Chemical Society*, 143(45):18838–18843, 11 2021. ISSN 15205126. doi: 10.1021/jacs.1c08749. URL `https://pubs.acs.org/doi/abs/10.1021/jacs.1c08749`.

[33] Katie A. Cychosz and Adam J. Matzger. Water stability of microporous coordination polymers and the adsorption of pharmaceuticals from water. *Langmuir*, 26(22):17198–17202, 11 2010. ISSN 07437463. doi: 10.1021/la103234u. URL `https://pubs.acs.org/doi/full/10.1021/la103234u`.

[34] Alternative Fuels Specifications | California Air Resources Board. URL `https://ww2.arb.ca.gov/resources/documents/alternative-fuels-specifications`.

[35] Farhana Gul-E-Noor, Bettina Jee, Andreas Pöppl, Martin Hartmann, Dieter Himsl, and Marko Bertmer. Effects of varying water adsorption on a Cu3(BTC)2 metal-organic framework (MOF) as studied by 1H and 13C solid-state NMR spectroscopy. In *Physical Chemistry Chemical Physics*, volume 13, pages 7783–7788. The Royal Society of Chemistry, 4 2011. doi: 10.1039/c0cp02848g. URL `https://pubs.rsc.org/en/content/articlelanding/2011/cp/c0cp02848g`.

[36] J. Raziel Álvarez, Elí Sánchez-González, Eric Pérez, Emilia Schneider-Revueltas, Ana Martínez, Adriana Tejeda-Cruz, Alejandro Islas-Jácome, Eduardo González-Zamora, and Ilich A. Ibarra. Structure stability of HKUST-1 towards water and ethanol and their effect on its CO2 capture properties. *Dalton Transactions*, 46(28):9192–9200, 7 2017. ISSN 14779234. doi: 10.1039/c7dt01845b.

[37] Jarad A. Mason, Mike Veenstra, and Jeffrey R. Long. Evaluating metal-organic frameworks for natural gas storage. *Chemical Science*, 5(1):32–51, 11 2014. ISSN 20416520. doi: 10.1039/c3sc52633j. URL `https://pubs.rsc.org/en/content/articlelanding/2014/sc/c3sc52633j`.

[38] Jarad A. Mason, Julia Oktawiec, Mercedes K. Taylor, Matthew R. Hudson, Julien Rodriguez, Jonathan E. Bachman, Miguel I. Gonzalez, Antonio

Cervellino, Antonietta Guagliardi, Craig M. Brown, Philip L. Llewellyn, Norberto Masciocchi, and Jeffrey R. Long. Methane storage in flexible metal-organic frameworks with intrinsic thermal management. *Nature*, 527 (7578):357–361, 10 2015. ISSN 14764687. doi: 10.1038/nature15732. URL `https://www.nature.com/articles/nature15732`.

[39] Inc American Honda Motor Co. Emergency Response Guide: Honda Natural Gas Vehicles. 2012. ISSN 15337502. URL `https://techninfo.honda.com`.

[40] EIA. Total Energy Monthly Data - U.S. Energy Information Administration (EIA), 2021. URL `https://www.eia.gov/totalenergy/data/monthly/`.

[41] Zhihong Yuan, Mario R. Eden, and Rafiqul Gani. Toward the Development and Deployment of Large-Scale Carbon Dioxide Capture and Conversion Processes. *Industrial and Engineering Chemistry Research*, 55(12):3383–3419, 12 2016. ISSN 15205045. doi: 10.1021/acs.iecr.5b03277. URL `https://pubs.acs.org/doi/10.1021/acs.iecr.5b03277`.

[42] Jian Bin Lin, Tai T.T. Nguyen, Ramanathan Vaidhyanathan, Jake Burner, Jared M. Taylor, Hana Durekova, Farid Akhtar, Roger K. Mah, Omid Ghaffari-Nik, Stefan Marx, Nicholas Fylstra, Simon S. Iremonger, Karl W. Dawson, Partha Sarkar, Pierre Hovington, Arvind Rajendran, Tom K. Woo, and George K.H. Shimizu. A scalable metal-organic framework as a durable physisorbent for carbon dioxide capture. *Science*, 374(6574):1464–1469, 12 2021. ISSN 10959203. doi: 10.1126/science.abi7281. URL `https://www.science.org/doi/10.1126/science.abi7281`.

[43] Hayden A. Evans, Dinesh Mullangi, Zeyu Deng, Yuxiang Wang, Shing Bo Peh, Fengxia Wei, John Wang, Craig M. Brown, Dan Zhao, Pieremanuele Canepa, and Anthony K. Cheetham. Aluminum formate, Al(HCOO)3: An earth-abundant, scalable, and highly selective material for CO2 capture. *Science Advances*, 8(44):1473, 11 2022. ISSN 23752548. doi: 10.1126/sciadv.ade1473. URL `https://www.science.org/doi/10.1126/sciadv.ade1473`.

[44] Anne Elise Creamer and Bin Gao. Carbon-based adsorbents for postcombustion CO2 capture: A critical review. *Environmental Science and Technology*, 50(14):7276–7289, 7 2016. ISSN 15205851. doi: 10.1021/acs.est.6b00627. URL `https://pubs.acs.org/doi/full/10.1021/acs.est.6b00627`.

[45] Sadashiv Bubanale and M Shivashankar. History, Method of Production, Structure and Applications of Activated Carbon. *International Journal of Engineering Research and Technology*, 6(06), 2017. doi: 10.17577/ijertv6is060277. URL `www.ijert.org`.

[46] Yuan Gao, Qinyan Yue, Baoyu Gao, and Aimin Li. Insight into activated carbon from different kinds of chemical activating agents: A review. *Science*

of the Total Environment, 746:141094, 12 2020. ISSN 18791026. doi: 10. 1016/j.scitotenv.2020.141094.

[47] Joseph Jjagwe, Peter Wilberforce Olupot, Emmanuel Menya, and Herbert Mpagi Kalibbala. Synthesis and Application of Granular Activated Carbon from Biomass Waste Materials for Water Treatment: A Review, 11 2021. ISSN 23699698.

[48] E. Raymundo-Piñero, P. Azaïs, T. Cacciaguerra, D. Cazorla-Amorós, A. Linares-Solano, and F. Béguin. KOH and NaOH activation mechanisms of multiwalled carbon nanotubes with different structural organisation. *Carbon*, 43(4):786–795, 1 2005. ISSN 00086223. doi: 10.1016/j.carbon.2004.11.005.

[49] Marta Sevilla and Antonio B. Fuertes. Sustainable porous carbons with a superior performance for CO2 capture. *Energy and Environmental Science*, 4(5):1765–1771, 4 2011. ISSN 17545706. doi: 10.1039/c0ee00784f. URL https://pubs.rsc.org/en/content/articlehtml/2011/ee/ c0ee00784fhttps://pubs.rsc.org/en/content/articlelanding/ 2011/ee/c0ee00784f.

Chapter 2

ADSORPTION FUNDAMENTALS

"If you want to find the secrets of the universe, think in terms of energy, frequency and vibration."

— Nikola Tesla

2.1 Types of Adsorption

Physisorption and Disperson Forces

The following sections on the descriptions of the two types of adsorption have been adapted from Rouquerol.[1] The primary mechanism for physical gas adsorption (physisorption) between neutral species without a permanent dipole moment is through London dispersion forces, which are the weakest type of van der Waals forces. Dispersion forces result from charge interactions through induced dipoles. These forces are the reason why noble gases can liquify without chemical reactions, and many properties of physisorption have analogues to the condensation of a gas into a liquid phase. Adsorbents provide a structural framework for gases (adsorbates) to adhere to, providing a binding energy which generally increases the adsorbates density and lowers the Gibbs free energy relative to the bulk fluid phase. Physisorption always is exothermic (negative enthalpy) on adsorption, the magnitude of which is known as the heat of adsorption. Dispersion forces are non-local in nature, decaying as r^{-6} with distance, making adsorption properties highly sensitive to the microstructure and topology of the adsorbent. The fundamental property

of physisorption is that the adsorbate is not chemically altered on adsorption or desorption, and as such does not chemically react with the adsorbent.

The Lennard-Jones potential (L-J), also known as the 12-6 potential, is often used with empirical parameters to describe physisorption, and has the form

$$\Phi_{LJ} = 4\varepsilon_{LJ}\left[\left(\frac{\sigma_{LJ}}{r}\right)^{12} - \left(\frac{\sigma_{LJ}}{r}\right)^{6}\right] \tag{2.1}$$

where ε_{LJ} is the adsorbate-adsorbent binding energy, σ_{LJ} is the effective diameter of the adsorbate-adsorbent system, and r is distance from the surface. While the 6 term (r^{-6}) is based on the dispersion interactions, the 12 power is not fundamentally rigorous, and is used to account for the atomic repulsion originating from the Pauli exclusion principle. The 12-6 potential, while empirical, sets up the basis of tunability of the adsorption potential: repulsion acts against attraction in a characteristic way for an adsorbent/adsorbate pair.

The direct method for increasing binding energy is to increase the polarizability of either the adsorbent or adsorbate. For a fixed gas application, this requires functionalization of the adsorbent with dopants. The ultimate compositional tuning is achieved by changing the bulk composition of the adsorbing surface. An indirect method also exists for increasing binding energy in a pore, where two overlapping potentials from a slit pore can increase the depth of the potential well. The binding strength of gas in adsorbents is therefore sensitive to the microstructure of the adsorbent, especially in pores near the size of the van der Waals radius of the gas. In Figure 2.1, several conditions with an arbitrary Lennard-Jones potential are shown where the surface potentials completely overlap (a), mostly overlap (b), have some
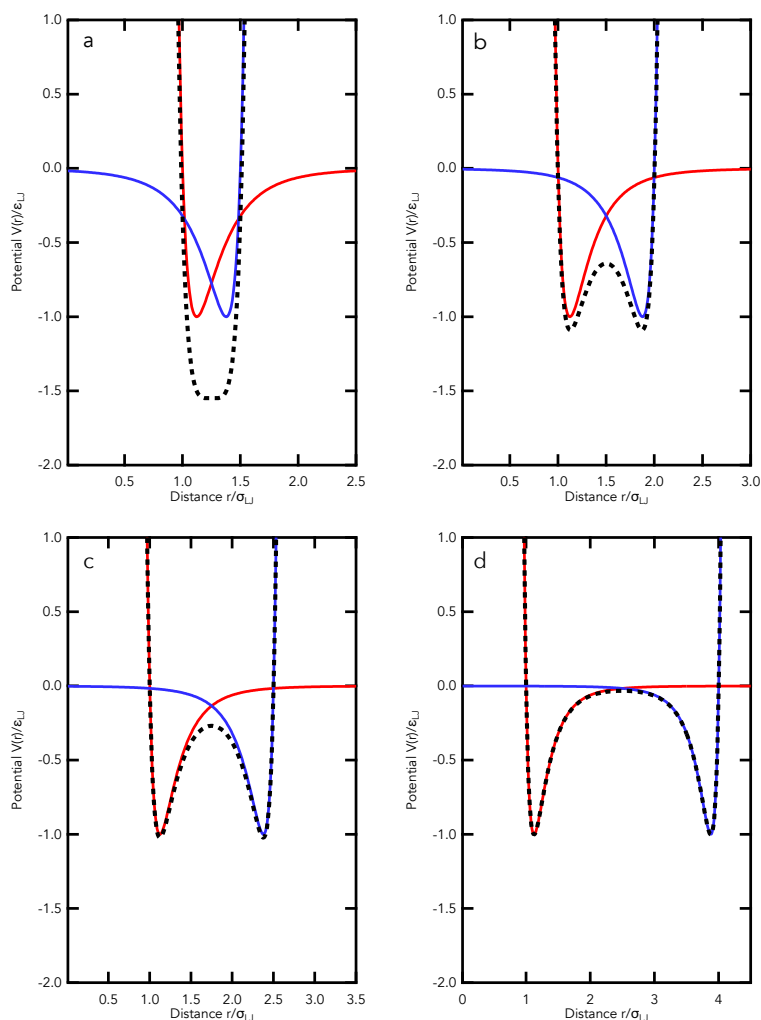
Figure 2.1: Lennard-Jones potential curves in pores of two identical infinite surfaces with separation distance $2.5\sigma_{LJ}$ (a), $3\sigma_{LJ}$ (b), $3.5\sigma_{LJ}$ (c), and $4.5\sigma_{LJ}$ (d).

overlap (c), and are two independent physisorption sites (d). The depth and shape of the potential well changes with degree of overlap.

Chemisorption and Chemical Bonding

The second type of adsorption is known as chemical adsorption (chemisorption) where adsorbates chemically bind and react to surface sites in the adsorbent.

These bonds are generally one or more orders of magnitude stronger than the weaker forces that describe physisorption. Due to the nature of chemical bonds (and particularly with diatomic gases such as hydrogen which dissociatively bind to surfaces), chemisorption is less reversible than physisorption and is often associated with an activation energy required for adsorption. Chemisorption often requires enough thermal energy to overcome this energy barrier, and results in long equilibration times. Since physisorption can occur to some extent at all temperatures and pressures, chemisorbitive systems also have some level of physisorption. If an adsorbate needs to dissociate before chemisorbing, a potential energy barrier can exist separating the physisorption process from the chemisorption one. In this case, the chemisorption is an activated process if this barrier is above the potential energy of the molecule existing an infinite distance away from the surface (see Figure 2.2 for an illustration of this phenomenon).

2.2   Statistical Mechanical Modelling of Adsorption Phenomena

Hydrogen gas is the prototypical example of an adsorbate which can both physisorb (as molecular H_2) or chemisorb (as atomic H) onto adsorbates. Generally hydrogen adsorbs molecularly on carbonaceous materials, and atomically through dissociation on catalytic metal surfaces. A depiction of the two types of adsorption, as applied to hydrogen on the surface of a material is shown from an energy standpoint in Figure 2.2 and depicted in Figure 2.3. Protium and deuterium can be used as "isotopic tracers" to identify the type of adsorption as molecular hydrogen dissociates during chemisorption, and random recombination is observed.
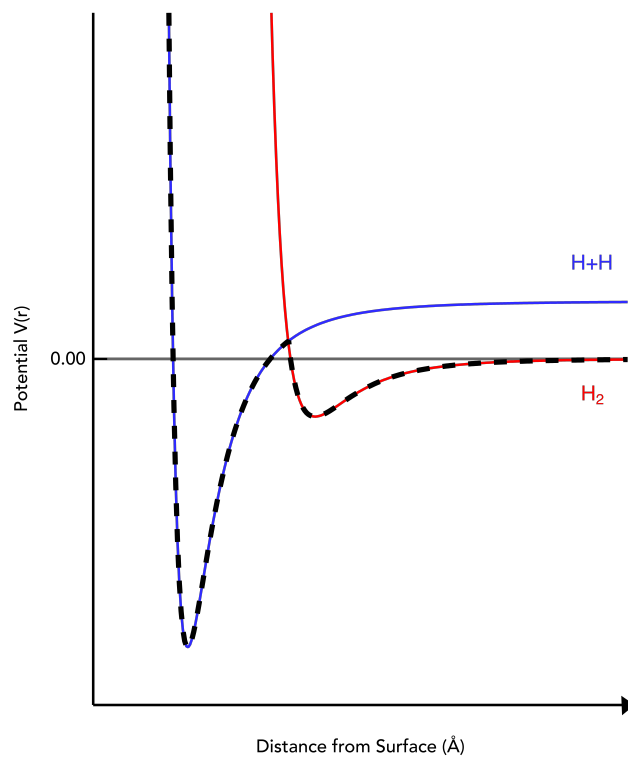
Figure 2.2: Diagram showing physisorption (red) and dissociative chemisorption (blue) of hydrogen adsorption. The black dashed trace shows the overall path for chemisorption, involving physisorption and a dissociation activation barrier. Zero energy is defined as the potential of molecular hydrogen an infinite distance from the surface. The offset of the blue curve at large distances is due to energy of molecular dissociation. Adapted from Zangwill.[2]

To extract thermodynamic information from empirical data on adsorption, it is necessary to have a thermodynamic model which describes adsorption uptake as a function of temperature and pressure. Irving Langmuir's original derivation of the Langmuir isotherm was done using kinetics arguments.[3, 4] However, adsorption phenomena can also be derived using statistical mechanics from the grand canonical partition function (thermodynamic derivations adapted from references). [2, 5]

Single-Site Physisorption Langmuir Model

The molecular physisorption single-site Langmuir is shown for hydrogen to compare with the dissociative version, however the derivation is not unique for hydrogen.

A lattice site assumption is made where each site is non-interacting with other sites and can be either unoccupied (E=0) or occupied (E= ε_i), which is shown in the left of Fig 2.3 with adsorption energy ε_{H_2}. The Gibbs factor is defined as

$$e^{\beta(\mu N_i - \varepsilon_i)} \tag{2.2}$$

with thermodynamic temperature $\beta = \frac{1}{k_B T}$, Boltzmann constant k_B, temperature T, number of particles N_i, chemical potential μ_i and energy ε_i. Note that for an unoccupied site, $N_i = 0$ and $\varepsilon_i = 0$ such that the Gibbs factor is 1.

The following single-site grand canonical partition function is obtained by the summation of the unoccupied and occupied Gibbs factors (including the partition function of the adsorbed site):

$$\xi_{H_2}(\mu, V, T) = 1 + q_p(T)e^{-\beta\varepsilon_{H_2}}e^{\beta\mu_{H_2}}. \tag{2.3}$$
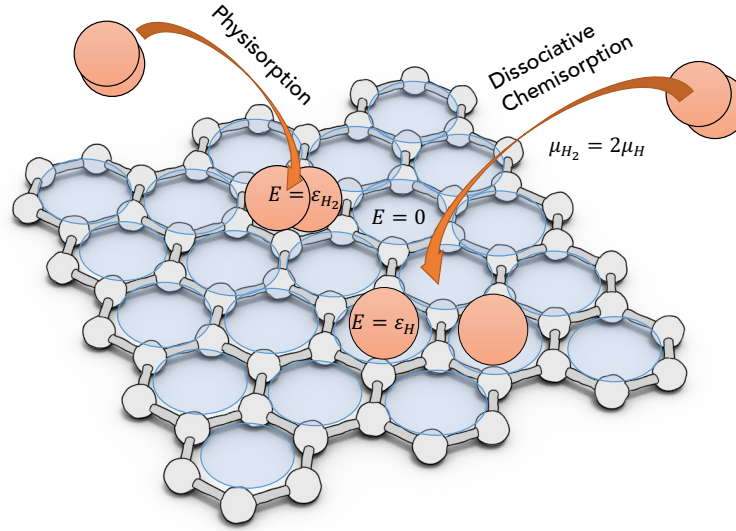
Figure 2.3: Physisorption (left) of a diatomic gas molecule on a lattice site with adsorption energy ε_{H_2} relative to the unoccupied sites where energy is defined to be 0. Chemisorption and dissociation of a diatomic molecule (right) on a lattice site with adsorption energy ε_H. Note that for dissociation, the adsorbed chemical potential is half of the gas phase chemical potential.

In the above equation, μ_{H_2} is the molecular hydrogen chemical potential, ε_{H_2} is the molecular hydrogen binding energy, and $q_p(T)$ is the partition function of the physisorbed site.

For most gases near ambient conditions on carbon-based surfaces, we assume that the partition function is that of a 2D liquid-like adsorbed state (2D translational freedom with an out-of-plane vibrational component) such that

$$q_p(T) = q_{p,\text{trans}} q_{p,\text{vib}} = \frac{A_B}{\lambda_{\text{ads}}^2} \frac{k_B T}{\hbar \omega} \tag{2.4}$$

$$\lambda_{\text{ads}} = \left(\frac{2\pi \hbar^2}{m k_B T} \right)^{1/2} \tag{2.5}$$

where A_B is the binding site area of adsorption site, $\hbar$ is Planck's constant, ω is the vibrational frequency and λ_{ads} is the thermal de Broglie wavelength of the adsorbed molecule with mass m. Here we assume that we are in the classical vibrational
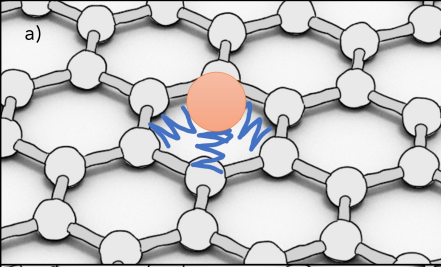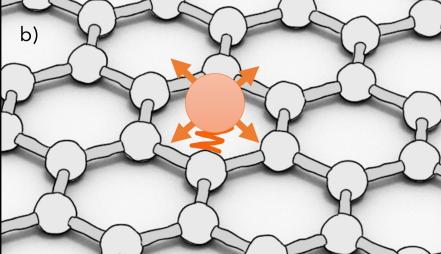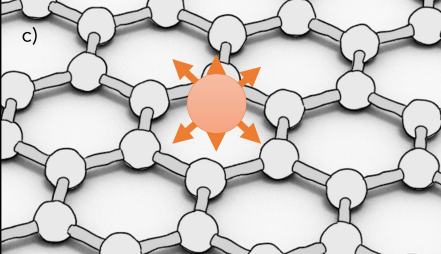
a)	Adsorbed State Approximation:	Partition Function (q):	Prefactor Temperature Dependence: $K = \frac{A}{T^x} e^{-\beta\varepsilon}$
	3D Vibrational: $\hbar\omega \gg k_B T$ "Chemisorption"	$q = q_{3D,vib} \approx 1$	$x = 5/2$
b)	1D Vibrational: $\hbar\omega \ll k_B T$ 2D Translational "2D Liquid Physisorption"	$q = q_{1D,vib} q_{2D,trans}$ $q = \frac{kT}{\hbar\omega} \frac{A_B}{\lambda_{ads}^2} \propto T^2$	$x = 1/2$
c)	3D Translational "3D Gas Physisorption"	$q = q_{3D,trans}$ $q = \frac{V_B}{\lambda_{ads}^3} \propto T^{3/2}$	$x = 1$

Figure 2.4: Adsorption partition functions and the underlying dimensional assumptions. A 3D vibrational state with oscillations in the ground state (a) is assumed for strongly-bound adsorption sites, particularly at low temperatures or chemisorption systems. A 2D in-plane translational liquid-like state with an out-of-plane perpendicular vibrational mode (b) is assumed for most physisorbed systems near ambient conditions. A 3D binding volume with translational freedom and no vibrational modes (c) is assumed for high temperature adsorption.

limit ($k_B T \gg \hbar\omega$). The total grand partition function for an adsorbent with Γ_t non-interacting sites is:

$$\Xi(\mu, V, T) = \xi_{H_2}^{\Gamma_t}. \tag{2.6}$$

The average number of adsorbed species is:

$$<n_a> = \left(\frac{\partial \ln \Xi}{\partial \beta\mu}\right) = \Gamma_t \frac{q_p(T) e^{-\beta\varepsilon_{H_2}} e^{\beta\mu_{H_2}}}{1 + q_p(T) e^{-\beta\varepsilon_{H_2}} e^{\beta\mu_{H_2}}}. \tag{2.7}$$

In equilibrium, the chemical potential for all adsorbates is the same. When the bulk fluid is an ideal gas:

$$\mu = \frac{\ln(\lambda_g^3 \beta P)}{\beta} \equiv \mu^{g,0}(T) + \frac{\ln P}{\beta} \tag{2.8}$$

where λ_g is the thermal de Broglie wavelength of the bulk gas. Here we assume that the adsorbed thermal de Broglie wavelength is equal to that of the bulk gas such that $\lambda_g = \lambda_{\mathrm{ads}}$, which means that the adsorbed atoms are not trapped in a potential well in x-y.

Therefore:

$$< n_a > = \Gamma_t \theta = \Gamma_t \frac{K_p P}{1 + K_p P} \tag{2.9}$$

$$K_p = A_B \frac{\lambda_g}{\hbar \omega} e^{-\beta \varepsilon_{H_2}} \tag{2.10}$$

which is the single-site physisorption Langmuir isotherm where θ is the fraction of occupied sites and K_p is known as the physisorption Langmuir constant.

Extension to Double-Site Physisorption Langmuir Model

The single-site physisorption Langmuir isotherm can be extended to a double-site Langmuir model, which increases the goodness of fit for materials that have a distribution of sites. The total number of sites Γ_t are split into two sites $i = \{1, 2\}$, each with energy ε_i and number of sites Γ_i, such that Eq. 2.9 and Eq. 2.10 become:

$$< n_a > = \Gamma_t \theta = \Gamma_t \left((1 - \alpha) \frac{K_{p,1} P}{1 + K_{p,1} P} + \alpha \frac{K_{p,2} P}{1 + K_{p,2} P} \right) \tag{2.11}$$

$$K_{p,i} = A_{B,i} \frac{\lambda_g}{\hbar \omega_i} e^{-\beta \varepsilon_i} \tag{2.12}$$

where α is defined such that $\Gamma_1 = \Gamma_t (1 - \alpha)$ and $\Gamma_2 = \Gamma_t \alpha$.

Langmuir Constant Temperature Dependence

For ease of fitting to experimental data without explicit values for vibrational components, $K_{p,i}$ is defined as:

$$K_{p,i} = \frac{A_i}{\sqrt{T}} e^{-\beta \varepsilon_i} \tag{2.13}$$

where $K_{p,i}$ is the Langmuir constant for physisorption site i and A_i is the temperature-independent Langmuir constant prefactor used for fitting. In general, the temperature dependence of the Langmuir constant varies depending on the partition function that is used for the adsorbed gas.

Reasonable assumptions can be made based on the temperature and pressure of the adsorption isotherms relative to the vibrational modes of the adsorbate with the surface (see Fig. 2.4). The nature of the adsorbed phase has been known to change with temperature and pressure,[1] and the partition function must be valid over the thermodynamic range of isotherm measurements. Fig. 2.4a shows the lowest temperature condition (assumed for chemisorption), where the adsorbed molecule is fixed to a specific site, with no translational freedom, in the vibrational ground state. Fig. 2.4b is the assumed case for physisorption of gases near ambient temperature, with two-dimensional translational freedom and an out-of-plane vibrational mode in the classical limit. Fig. 2.4c is similar to the previous case, except the vibrational mode is converted into another translational degree of freedom, which is the case for a three-dimensional adsorbed gas.

Most commonly, a $\frac{1}{T}$ or $\frac{1}{\sqrt{T}}$ has been used in past studies, and both of these assumptions have been shown to fit experimental data sufficiently. However, it

should be noted that changing the prefactor temperature dependence will result in changes to the temperature dependence of the isosteric heat of adsorption. Detailed adsorption calorimetry studies or quasielastic/inelastic neturon studies for an adsorbent/adsorbate combination would need to be conducted to justify a proper choice in the partition function used for a certain temperature and pressure range. Unfortunately, such studies are often out of the scope of basic adsorption research.

Double-Site Dissociative Langmuir Isotherm Derivation

The derivation for the dissociative adsorption isotherm is similar to that of the simple physisorption isotherm.[2] One major difference is that there are now two atoms instead of one on the surface, so the chemical potential (which must be equal for the gas and adsorbed phases in equilibrium) is

$$2\mu_H = \mu_g. \tag{2.14}$$

In the case of a single adsorbed atom of gas, (for a double-site Langmuir model where the first site is for physisorption only and the second site is for chemisorption), the grand canonical partition function for the chemisorption site is:

$$\xi_2(\mu, V, T) = 1 + q_c(T)e^{-\beta\varepsilon_H}e^{\beta\mu_H}. \tag{2.15}$$

where ε_H is the chemisorption binding energy and q_c is the chemisorption partition function.

For chemisorption, we assume localized bonding to the site, so the translational component of the adsorbed phase is negligible and we assume a high vibrational

energy of hydrogen. The vibrational entropy is not temperature dependent (the quantum oscillator is primarily in the ground state) and $q_{vib}(T) \simeq 1$. This assumption is supported by $\hbar\omega \approx 129$ meV perpendicular and $\hbar\omega \approx 100$ meV in-plane vibrational energy of atomic hydrogen on copper, determined using EELS.[6] The translational and vibrational partition function will be assumed to be independent of temperature ($q_2(T) = q_2$)).

Using Eq. 2.8 and Eq. 2.14,

$$\mu_H = \frac{\mu_g}{2} = k_B T \ln(\sqrt{\lambda_g^3 \beta P}) \tag{2.16}$$

and substituting Eq. 2.15 as the second site in Eq. 2.7

$$< n_a > = \Gamma_1 \frac{q_p(T)e^{-\beta\varepsilon_1}e^{\beta\mu}}{1 + q_p(T)e^{-\beta\varepsilon_1}e^{\beta\mu}} + \Gamma_2 \frac{\sqrt{\lambda_g^3 \beta P}q_c e^{-\beta\varepsilon_H}}{1 + \sqrt{\lambda_g^3 \beta P}q_c e^{-\beta\varepsilon_H}}. \tag{2.17}$$

If we define

$$K_{p,1} = A_{B,1} \frac{\lambda_g}{\hbar\omega} e^{-\beta\varepsilon_1} = \frac{A_1}{\sqrt{T}} e^{-\beta\varepsilon_{H_2}} \tag{2.18}$$

$$K_c(T) \equiv \frac{\lambda_g^3(T)q_2^2}{k_B T} e^{-2\varepsilon_H/k_B T} = \frac{A_2}{T^{5/2}} e^{-\beta\varepsilon_H} , \tag{2.19}$$

$$< n_{a,\text{dlDis}} > = \Gamma_t \theta = \Gamma_t \left((1-\alpha)\frac{K_{p,1}P}{1 + K_{p,1}P} + \alpha\frac{\sqrt{K_c P}}{1 + \sqrt{K_c P}} \right) \tag{2.20}$$

where K_p and K_c are the physisorption and chemisorption Langmuir constants, respectively, and α is defined as the fraction of chemisorption sites such that $\Gamma_2 = \Gamma_t \alpha$ and $\Gamma_1 = \Gamma_t(1-\alpha)$.

Limitations to the Langmuir Model

The Langmuir model has many built-in assumptions. The first and foremost is that it assumes monolayer coverage, while many systems show multilayer adsorption at high pressures and low temperatures. The second is that it is only concerned with adsorbate-adsorbent interactions (the interactions of the gas molecule with the surface), and has no corrections for gas-gas interactions (non-ideal gas behavior) or adsorbate-adsorbate interactions (adsorption sites are assumed to be independent and non-interacting). Hydrogen has minimal gas-gas interactions in the bulk phase, however with heavier gases (such as methane and carbon dioxide) these interactions are non-negligible at high pressures and low temperatures.

Real-Gas Corrections to Langmuir Model

To account for gas-gas interactions, fugacity can be introduced as

$$f = P\phi(P,T) \tag{2.21}$$

where P is pressure and ϕ is the fugacity coefficient. An ideal gas has a fugacity coefficient of 1, which is reasonable for most gases at low pressures and high temperatures. Rewriting the chemical potential using fugacity

$$\mu = \frac{log(\lambda^3 \beta P)}{\beta} + \frac{log(\phi)}{\beta} \tag{2.22}$$

and using the same definition of K (Eq. 2.12), this new chemical potential can be substituted back into the thermodynamic definition of n_a in Eq. 2.7 to obtain the fugacity-equivalent version of Eq. 2.11:

$$< n_a > = \Gamma_1 \frac{P\phi A_{B,1} \frac{\lambda}{\hbar\omega} e^{-\beta\varepsilon_1}}{1 + P\phi A_{B,1} \frac{\lambda}{\hbar\omega} e^{-\beta\varepsilon_1}} + \Gamma_2 \frac{P\phi A_{B,2} \frac{\lambda}{\hbar\omega} e^{-\beta\varepsilon_2}}{1 + P\phi A_{B,2} \frac{\lambda}{\hbar\omega} e^{-\beta\varepsilon_2}} \tag{2.23}$$

Adsorption Definitions

Absolute Uptake
n_a in volume v_a

Adsorbate
skeletal
density

Gibbs Excess n_e

Gas in Dead Space at
density $\rho(P,T)$
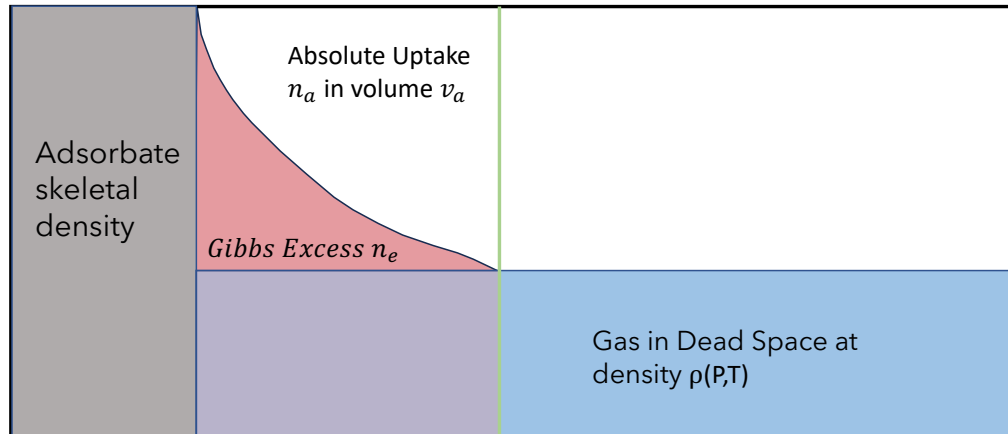
"Total" Uptake= Absolute Uptake + Dead Space Gas

Figure 2.5: Diagram of adsorption uptake definitions. The Gibbs excess uptake, which is directly measured by the Sieverts technique, is shown in pink, and is the amount of gas measured in the sample removing the amount of gas assumed to be in the empty volume (shown in blue and purple). The empty volume is determined by subtracting the adsorbent skeletal volume (grey) from the total empty reactor volume. The absolute uptake, which is needed for thermodynamic calculations, is the measured excess uptake plus the bulk gas density in adsorbed volume v_a, which is the sum of the gas to the left of the green line (known as the adsorption volume v_a). The total uptake is the absolute uptake plus the non-adsorbed volume "void space" in the reactor.

$$< n_a >= \Gamma_t \theta = \Gamma_t \left((1 - \alpha) \frac{K_1 f}{1 + K_1 f} + \alpha \frac{K_2 f}{1 + K_2 f} \right). \tag{2.24}$$

2.3   Adsorption Measurements

Sieverts Apparatus

To discuss adsorption measurements, strict definitions must be made to describe what uptake quantity and adsorption metric is being used. Gibbs in 1878 defined what would be known as the "Gibbs dividing surface," [7] which is an invisible line that is drawn at the boundary between the adsorbate and the bulk fluid. The
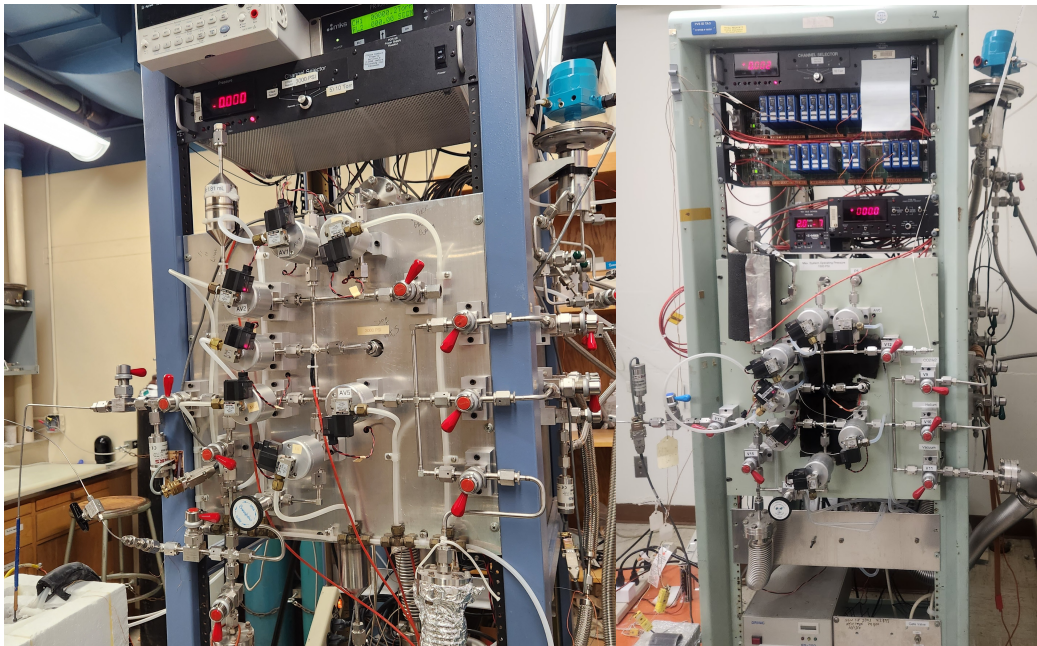
Figure 2.6: Custom automated Sieverts apparatuses used for high pressure (100 bar) adsorption measurements on methane and hydrogen (left) and nitrogen and carbon dioxide (right).

adsorbent itself takes up volume, and the volume per mass adsorbent is known as the skeletal density of the adsorbent. From an experimental standpoint, all experiments measure what is known as the "Gibbs excess uptake," or simply as "excess uptake," which is the measured adsorbate quantity in addition to what is expected if no adsorbate were present (not including the adsorbent skeletal volume). The thermodynamic quantity of interest (as discussed above) is the absolute uptake which includes the excess uptake and the portion of adsorbed gas that has the same density bulk fluid density, in adsorption volume v_a. Unfortunately, the adsorbed fluid volume is needed to obtain the absolute uptake, and it cannot be measured directly. A diagram of the relationship of these different uptake quantities is shown in Fig. 2.5. The Sieverts apparatus is a device designed to measure the excess uptake. There are two types of adsorption measurement systems: a gravimetric balance and

a volumetric Sieverts. A gravimetric balance system applies gas pressure to a sample suspended by a weighing apparatus. The machine measures the change in adsorbent weight with pressure (carefully accounting for the buoyant force acting on the sample mass) at a fixed temperature T. A volumetric Sieverts system has a carefully calibrated manifold volume, and doses incremental quantities of gas into the sample reactor (with known volume). The amount of gas is determined from the bulk fluid density at a given pressure and temperature (which are experimentally measured after gas equilibration) based on the experimental equation of state for the gas.[8] These uptake measurements as a function of pressure at fixed temperatures are called "excess isotherms," and are the raw experimental data measured in this work. The skeletal density is a property unique to each adsorbent, and is physically measured using helium pycnometry near ambient temperature. This measurement is very similar to a volumetric Sieverts measurement, except the working assumption is that no helium is adsorbed meaning that the change in volume normalized by the sample mass is the skeletal density:

$$\rho_{\text{skel}} = \frac{V_{\text{empty}} - V_{\text{filled}}}{m_{\text{sample}}}. \tag{2.25}$$

Adsorption Microstructural Characterization

A specialized volumetric Sieverts system designed for high-resolution pressure measurements up to atmospheric pressure is used for microstructural sample characterization. These adsorption measurements are usually conducted at the atmospheric boiling point of the probe gas molecule (in this work, N_2 or Ar) as a method to measure the pore volume in the material. The Brunauer–Emmett–Teller

(BET) method is used as a metric for the probe-accessible specific surface area of the material. This method, while straightforward to use, generally overestimates the actual surface area of a material (especially for microporous materials) due to strong interactions of gas molecules on the adsorbent. Nonetheless, it serves as a good metric for comparison with other adsorbents and literature results. New emerging surface area metrics such as the non-local density functional theory (NLDFT) surface area, which is determined from pore size distributions of the adsorbent, offer more realistic surface area metrics and are a current field of research (see appendix for details).

Fitting of Experimental Isotherms

The experimentally measured Gibbs excess uptake can be written in terms of the absolute uptake

$$n_e = n_a - \rho_g v_a = (n_m - \rho_g v_m)\theta \tag{2.26}$$

where n_m, n_e, n_a, ρ_g, v_m, v_a and θ are the max absolute gas uptake, excess uptake, absolute uptake, gas density, maximum adsorbed volume, adsorbed volume, and fraction of occupied sites, respectively. The total number of sites $\Gamma_t = n_m N_A$, where N_A is Avogadro's number. This equation has the implicit assumption that the adsorption *volume* v_a dynamically changes with the fraction of filled sites θ, or that the adsorbed phase *density* is constant. The above assumption is consistent with a filling model where small pores get filled first, and a site is either empty or filled with an adsorbed phase density similar to the bulk liquid phase density for most adsorbates (this can be compared with the alternative assumption of a stagnant
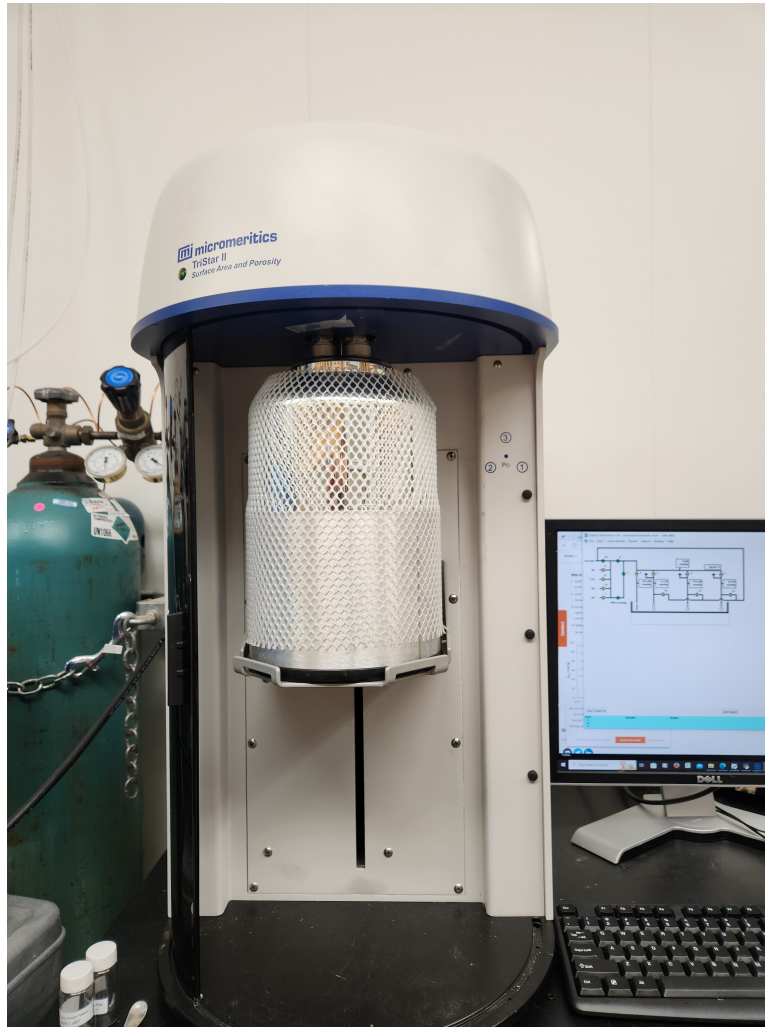
Figure 2.7: Micromeritics Tristar II system used for BET measurements, low pressure isotherm measurements (1 bar), and microstructural characterization.

adsorbed phase volume (dynamic adsorption density)

$$n_e = n_m\theta - \rho_g v_m \tag{2.27}$$

where the adsorbed gas occupies the same *volume* independent of site occupancy.

Each set of isotherms corresponding to a particular adsorbent was universally fitted to a double-site Langmuir equation with seven fitting parameters (see equations 2.12, 2.24, and 2.26) :

$$n_e(P,T) = (n_m - \rho_g(P,T)v_m)\left((1-\alpha)\frac{K_1(T)f}{1+K_1(T)f} + \alpha\frac{K_2(T)f}{1+K_2(T)f}\right). \quad (2.28)$$

Fugacity is only used for thermodynamic calculations. While both fugacity and pressure are needed for the real-gas Langmuir equation in Eq. 2.28, the resulting uptakes are plotted only against the experimentally measured pressures.

2.4 Volumetric Uptake

While gravimetric uptake is straightforward to define experimentally, volumetric uptake is challenging due to adsorbent packing efficiencies. The most general case for the total volume of a material is defined as

$$v_{\text{void}} + v_{\text{skel}} = v_{\text{bulk}} \quad (2.29)$$

where v_{void}, v_{skel}, and v_{bulk} are the specific void volume, adsorbent skeletal volume, and bulk sample volume, respectively. Two extremes are immediately apparent, which are $v_{\text{void}} = v_{\text{bulk}}$ (empty tank) and $v_{\text{skel}} = v_{\text{bulk}}$ (tank completely filled with non-adsorbing material).

For an ideal packing scenario, such as a single crystal of microporous material, all of the void volume contributes to adsorption:

$$v_{\text{pore}} + v_{\text{skel}} = v_{\text{bulk}} \quad (2.30)$$

where v_{pore} is the specific pore volume of the adsorbent. A packed powder adsorbent always has void volume, or dead space, that does not directly contribute to

adsorption, such that $v_{\mathrm{pore}} + v_{\mathrm{skel}} < v_{\mathrm{bulk}}$. To convert measured gravimetric excess uptake to volumetric excess uptake the following equation is used

$$n_{e,v}(P,T) = n_e(P,T)\rho_{\mathrm{bulk}}v_{\mathrm{g,STP}} \tag{2.31}$$

where ρ_{bulk} is the bulk density of the adsorbent, and $v_{\mathrm{g,STP}}$ is the molar volume of the adsorbate at STP. Volumetric uptake is unitless and is defined as V_{STP}/V, which is the amount of equivalent gas at STP adsorbed normalized by the adsorbent volume.

The total volumetric uptake is the sum of excess volumetric uptake and the bulk gas phase in the adsorbent

$$n_{t,v} = n_{e,v} + (\rho_g v_g X_{\mathrm{pore}}). \tag{2.32}$$

It is necessary to know the void fraction of the bulk material, X_{pore}, to calculate the total volumetric uptake. Physically, this is the ratio of empty void volume to the physical volume of the sample. A commonly used approximation in literature is

$$X_{\mathrm{pore,common}} = \frac{v_{N_2}}{v_{\mathrm{bulk}}} = \rho_{\mathrm{bulk}}v_{\mathrm{pore}}. \tag{2.33}$$

This is accurate for an ideal pellet of a single crystal adsorbent with no macropores or surface roughness. We will be using this metric to compare with other results from literature, as this is the most prevalent one used. Theoretically, a better metric for accounting for the void fraction is

$$X_{\mathrm{pore,best}} = \frac{v_{\mathrm{bulk}} - v_{\mathrm{skel}}}{v_{\mathrm{bulk}}} = 1 - \frac{\rho_{\mathrm{bulk}}}{\rho_{\mathrm{skel}}}. \tag{2.34}$$

However, the challenges in measuring the skeletal density with a high enough degree of precision makes this metric hard to use accurately in practice.

2.5 Adsorption Thermodynamic Properties

Derivation of Isoexcess and Isosteric Enthalpy of Adsorption

From the absolute uptake obtained in Eq. 2.28 it is possible to calculate thermodynamic properties such as the adsorption enthalpy Δh_{ads}.[9, 5] In equilibrium, the chemical potentials of the gas phase and adsorbed phase are equal:

$$\mu_g = \mu_a. \tag{2.35}$$

Using the Gibbs-Duhem relation:

$$d\mu = -sdT + vdP \tag{2.36}$$

for both the gas and adsorbed phase, Eq. 2.35 can be combined as:

$$-s_a dT + v_a dP = -s_g dT + v_g dP\big|_{n_a=\text{const}}. \tag{2.37}$$

Rearranging terms:

$$\left(\frac{\partial P}{\partial T}\right)_{n_a} = \frac{s_a - s_g}{v_a - v_g}. \tag{2.38}$$

with the definition of enthalpy at constant pressure, temperature ($dP, dT = 0$):

$$\Delta h = T\Delta s \tag{2.39}$$

the Clapeyron equation is obtained:

$$\left(\frac{\partial P}{\partial T}\right)_{n_a} = \frac{\Delta h}{T\Delta v} \tag{2.40}$$

where $\Delta v = v_a - v_g = \frac{v_m}{n_m} - v_g$.

With Eq. 2.40 and the molar ideal gas equation:

$$Pv = k_B T \tag{2.41}$$

if the approximation $\Delta v \approx -v_g$ is employed (the volume of the gas is much greater

than the adsorbed phase volume), and Eq. 2.41 is substituted into Eq. 2.40,

$$\left(\frac{\partial P}{\partial T}\right)_{n_a} = -\frac{P\Delta h}{k_B T^2} \tag{2.42}$$

is obtained. Solving for Δh,

$$\Delta h = -\frac{k_B T^2}{P}\left(\frac{\partial P}{\partial T}\right)_{n_a} \tag{2.43}$$

which can be rewritten as (using the chain rule):

$$\Delta h = k_B \frac{\partial \ln(P)}{\partial(1/T)}_{n_a}. \tag{2.44}$$

If two isotherms that are close in temperature are used, approximate values for

Δh are obtained by setting the derivative to a discrete slope:

$$\Delta h = k_B \frac{\ln(P_2) - \ln(P_1)}{(1/T_2) - (1/T_1)} \tag{2.45}$$

$$\Delta h = k_B \frac{T_2 T_1}{T_1 - T_2} \ln \frac{P_2}{P_1} \tag{2.46}$$

which is the Clausius-Clapeyron equation. Pressures and temperatures are taken at

a given uptake. For the isosteric heat of adsorption, this is n_a however for isoexcess

this is n_e. At low coverage (dilute gas limit) it is relatively safe to assume $n_a \approx n_e$.

This assumption begins to fail when the excess uptake starts to reach a maximum,

indicating that the gas phase is non-negligible.

Returning to Eq. 2.40 and substituting in $v_g = 1/\rho_g$, the enthalpy of adsorption

can be obtained:

$$-\Delta h = -T\left(\frac{\partial P}{\partial T}\right)_{n_a}\left(\frac{v_m}{n_m} - \frac{1}{\rho_g}\right). \tag{2.47}$$

The $\left(\frac{\partial P}{\partial T}\right)_{n_a}$ is dependent on the adsorption model used (specifically θ), and can be determined with the following relationships

$$-\left(\frac{\partial P}{\partial T}\right)_{n_a} = \frac{\left(\frac{\partial \theta}{\partial T}\right)_{P,n_a}}{\left(\frac{\partial \theta}{\partial P}\right)_{T,n_a}}. \tag{2.48}$$

For the double-site physisorption Langmuir model:

$$\frac{\partial \theta}{\partial P} = (1 - \alpha)\left(\frac{K_{p,1}}{(1 + K_{p,1}P)^2}\right) + \alpha\left(\frac{K_{p,2}}{(1 + K_{p,2}P)^2}\right) \tag{2.49}$$

$$\frac{\partial \theta}{\partial T} = (1 - \alpha)\frac{\partial \theta}{\partial K_{p,1}}\frac{\partial K_{p,1}}{\partial T} + \alpha\frac{\partial \theta}{\partial K_{p,2}}\frac{\partial K_{p,2}}{\partial T} \tag{2.50}$$

$$\frac{\partial \theta}{\partial K_i}\frac{\partial K_i}{\partial T} = -\left(\frac{P}{(1 + K_{p,i}P)^2}\right) * (xRT + \varepsilon_i)\frac{K_{p,i}}{RT^2}. \tag{2.51}$$

For the double-site dissociative Langmuir model:

$$\frac{\partial \theta}{\partial P} = (1 - \alpha)\left(\frac{K_{p,1}}{(1 + K_{p,1}P)^2}\right) + \alpha\left(\frac{K_c}{2\sqrt{K_cP}(1 + \sqrt{K_cP})^2}\right) \tag{2.52}$$

$$\frac{\partial \theta}{\partial T} = (1 - \alpha)\frac{\partial \theta}{\partial K_{p,1}}\frac{\partial K_{p,1}}{\partial T} + \alpha\frac{\partial \theta}{\partial K_c}\frac{\partial K_c}{\partial T} \tag{2.53}$$

$$\frac{\partial \theta}{\partial K_c}\frac{\partial K_c}{\partial T} = -\left(\frac{P}{2\sqrt{K_cP}(1 + \sqrt{K_cP})^2}\right)(xRT + 2\varepsilon_H)\frac{K_c}{RT^2} \tag{2.54}$$

where the gas constant R has been substituted in for k_B to get energy per mole of adsorbate, and the binding energies ε_i and ε_H are negative for adsorption. The power of the prefactor temperature dependence is determined from the adsorbate partition function, and in our case, $x = 0.5$ for the physisorption terms and $x = 2.5$ for the chemisorption term.

2.6 Mixed Gas Adsorption

Ideal Adsorption Solution Theory (IAST), developed by Myers and Praunsnitz in 1965,[10] is based around an adsorption equivalent to Raoult's law. Raoult's law

states that the partial pressure of component i in an ideal solution mixture is equal to the pure component i partial pressure at the same thermodynamic conditions multiplied by its solution concentration. The following derivation is summarized from Simon's implementation of IAST in their pyIAST Python package.[11]

The main assumptions of this theory are:

- The adsorbed species form an ideal mixture (enthalpy of mixing is zero);

- Each lattice site is equally accessible by each adsorbed species (no sites exist that can be occupied only by a specific adsorbate).

Derivation of Adsorbed Raoult's Law

The Gibbs free energy for a 2D surface is defined as:

$$dG = -SdT + Ad\pi + \sum_{i=1}^{N} \mu_i dn_i \tag{2.55}$$

where A is the adsorbent surface area and π is the spreading pressure, the 2D equivalent of volume and pressure, respectively, with the 2D ideal gas law $\pi A = nk_B T$. Although the fluid is three-dimensional in the bulk phase, the loss of the out-of-plane translational freedom on the adsorbent results in a phase that can be modelled as two-dimensional.

Since $\Delta G_{mix} = \Delta H_{mix} - T\Delta S_{mix}$ and $\Delta H_{mix} = 0$ (ideal solution assumption), the Gibbs free energy is

$$G(T, \pi, n_j) = \sum_{i=1}^{N} G_i^0(T, \pi, n_i) - T\Delta S_{mix} \tag{2.56}$$

which is the Gibbs free energy of each adsorbate's pure state and an entropy of mixing component $\Delta S_{mix} = -k_B \sum_i n_i \ln \chi_i$, where χ_i is the adsorbed gas mole fraction of species i.

Chemical potential is defined as

$$\mu_i = \left(\frac{\partial G}{\partial n_i}\right)_{T,\pi,n_j} \tag{2.57}$$

such that, with Eq. 2.56

$$\mu_i(T,\pi,\chi_i) = \mu_i^0(T,\pi) + k_B T \ln \chi_i \tag{2.58}$$

where μ_i^0 is the pure adsorption chemical potential of gas species i. The ideal gas phase chemical potential for a partial component in a mixture (from Eq. 2.8) is defined as:

$$\mu_i^g(T,P,y_i) = \mu_i^{g,0}(T) + k_B T \ln p_i \tag{2.59}$$

where $p_i = y_i P$.

In equilibrium, the adsorption chemical potential equals the gas phase chemical potential and the pure component chemical potential ($\mu_i = \mu_i^g$). Equating Eq. 2.58 to Eq. 2.59, and solving for p_i:

$$p_i = \chi_i e^{\beta(\mu_i(\pi,T)-\mu_i^{g,0}(T))}. \tag{2.60}$$

For a pure gas, $\chi_i = 1$ such that

$$p_i^0 = e^{\beta(\mu_i(\pi,T)-\mu_i^{g,0}(T))} \tag{2.61}$$

$$p_i = \chi_i p_i^0(\pi,T) \tag{2.62}$$

which states that the partial pressure of an adsorbed gas species is the the pure component pressure multiplied by the molar adsorbed fraction. Note that this is for an ideal gas in that no gas-gas interactions are accounted for. The fugacity coefficient $\phi_i(P, T)$ can be introduced to account for the real-gas chemical potential (as in Eq. 2.22)

$$\mu_i^g(T, P, y_i) = \mu_i^{g,0}(T) + k_B T \ln p_i + k_B T \ln \phi_i \tag{2.63}$$

which leads to the following expression for the Raoult's Law:

$$f_i = \phi_i p_i = \chi_i \phi_i p_i^0(\pi, T). \tag{2.64}$$

Equivalence and Functional Form of Spreading Pressures

In the adsorbed phase, the pure component chemical potentials are equal $\mu_i^0(T, \pi_i) = \mu_j^0(T, \pi_j)$. Since the temperature is the same for all adsorbed species, and from the 2D ideal gas law $\pi(p_i^0, T)$, the spreading pressures are all equal:

$$\pi = \pi_a(p_a^0) = \pi_b(p_b^0)... = \pi_n(p_n^0). \tag{2.65}$$

From the Gibbs-Duhem equation for spreading pressure in a pure component adsorption system (dT=0)

$$-Ad\pi_i + n_i^0 d\mu_i^0 = 0 \tag{2.66}$$

and $d\mu_i^0$ can be written in terms of pressure from Eq. 2.59 as $d\mu_i = k_B T d \ln p_i^0$.

Combining the above equations and rearranging terms

$$d\pi = \frac{k_B T}{A} n_i^0 p_i^0 d \ln p_i^0. \tag{2.67}$$

Integrating both sides, and removing the integration constant as $\pi(P=0)=0$, the spreading pressure can be written as a function of pressure (based on the isotherm theta model that is used):

$$\pi_i(p_i^0) = \frac{k_{\mathrm{B}}T}{A} \int_0^{p_i^0} \frac{n_i^0(P)}{P} \, dP \tag{2.68}$$

$$\pi_i(p_i^0) = \frac{k_{\mathrm{B}}Tn_m}{A} \int_0^{p_i^0} \frac{\theta_i^0(P)}{P} \, dP. \tag{2.69}$$

As shown for the adsorption model, fugacity can be substituted in for pressure through the chemical potential in Eq. 2.63 to account for nonidealities in the gas phase. The double-site Langmuir model used in this work (from Eq. 2.24) gives the following form for the spreading pressure

$$\pi_i(f_i^0, T) = \frac{k_{\mathrm{B}}Tn_m}{A} \left[(1-\alpha)\ln(1+K_1(T)f_i) + \alpha\ln(1+K_2(T)f_i) \right]. \tag{2.70}$$

Since the same area A is accessible to all adsorbates, and all adsorbates experience the same thermal energy $k_{\mathrm{B}}T$, the $\frac{k_{\mathrm{B}}T}{A}$ term can be ignored when setting the spreading pressures of each gas component equal to each other.

Determination of Total Mixed Component Uptake

An expression for the total uptake n_T can be derived using the 2D ideal gas law and the definition of adsorbed mole fractions. The area of all of the adsorbed gas molecules must equal the total area of adsorption at a given pressure, temperature:

$$A_{\mathrm{T}}(P,T) = \sum_{i=1}^{N} A_i(P,T). \tag{2.71}$$

The adsorbed gas mole fraction can be written in terms of the fractional coverage (using the ideal gas law and the spreading pressure equivalence)

$$\sum_{i=1}^{N} \chi_i = \frac{\sum_{i=1}^{N} A_i}{A_T} = \sum_{i=1}^{N} \frac{\frac{n_i k_B T}{\pi_i}}{\frac{n_T k_B T}{\pi_T}} = \frac{\sum_{i=1}^{N} n_i}{n_T} \tag{2.72}$$

and solving for n_T the following equation is obtained:

$$\frac{1}{n_T} = \sum_{i}^{N} \frac{\chi_i}{n_i}. \tag{2.73}$$

References

[1] F. Rouquerol, J. Rouquerol, and Kenneth S. W. Sing. *Adsorption by Powders and Porous Solids*. Elsevier, 1999. doi: 10.1016/b978-0-12-598920-6.x5000-3.

[2] Andrew Zangwill. *Physics at Surfaces*. Cambridge University Press, 3 1988. ISBN 9780521321471. doi: 10.1017/cbo9780511622564. URL `https://www.cambridge.org/core/product/identifier/9780511622564/type/book`.

[3] Irving Langmuir. The constitution and fundamental properties of solids and liquids. II. Liquids. *Journal of the American Chemical Society*, 39(9):1848–1906, 11 1917. ISSN 15205126. doi: 10.1021/ja02254a006. URL `https://pubs.acs.org/doi/abs/10.1021/ja02268a002`.

[4] Irving Langmuir. The adsorption of gases on plane surfaces of glass, mica and platinum. *Journal of the American Chemical Society*, 40(9):1361–1403, 1918. ISSN 15205126. doi: 10.1021/ja02242a004. URL `https://pubs.acs.org/doi/10.1021/ja02242a004`.

[5] Nicholas Stadie. *Synthesis and thermodynamic studies of physisorptive energy storage materials*. PhD thesis, 2013. URL `http://thesis.library.caltech.edu/7198/`.

[6] Geunseop Lee and E. W. Plummer. High-resolution electron energy loss spectroscopy study on chemisorption of hydrogen on Cu(111). *Surface Science*, 498(3):229–236, 2 2002. ISSN 00396028. doi: 10.1016/S0039-6028(01)01765-4. URL `https://www.sciencedirect.com/science/article/pii/S0039602801017654`.

[7] Josiah Willard Gibbs. On the equilibrium of heterogeneous substances. *American Journal of Science and Arts*, s3-16:441–458, 1878.

[8] Ian H. Bell, Jorrit Wronski, Sylvain Quoilin, and Vincent Lemort. Pure and pseudo-pure fluid thermophysical property evaluation and the open-source thermophysical property library coolprop. *Industrial and Engineering Chemistry Research*, 53(6):2498–2508, 2014. ISSN 08885885. doi: 10.1021/ie4033999. URL `https://pubs.acs.org/doi/10.1021/ie4033999`.

[9] S. J. Gregg and Kenneth S. W. Sing. *Adsorption, Surface Area and Porosity*. Academic Press, London, 2nd edition, 1982. doi: https://doi.org/10.1002/bbpc.19820861019. URL `https://onlinelibrary.wiley.com/doi/abs/10.1002/bbpc.19820861019`.

[10] A. L. Myers and J. M. Prausnitz. Thermodynamics of mixed-gas adsorption. *AIChE Journal*, 11(1):121–127, 1 1965. ISSN 15475905. doi: 10.1002/aic.690110125. URL `https://onlinelibrary.wiley.com/doi/full/10.1002/aic.690110125`.

[11] Cory M. Simon, Berend Smit, and Maciej Haranczyk. PyIAST: Ideal adsorbed solution theory (IAST) Python package. *Computer Physics Communications*, 200:364–380, 3 2016. ISSN 00104655. doi: 10.1016/j.cpc.2015.11.016. URL `https://www.sciencedirect.com/science/article/pii/S0010465515004403`.

Chapter 3

HYDROGEN ADSORPTION ON COPPER MODIFIED ACTIVATED CARBON

"I believe that water will one day be employed as fuel, that hydrogen and oxygen which

constitute it, used singly or together, will furnish an exhaustible source of heat and light, of

an intensity of which coal is not capable... Water will be the coal of the future."

— Jules Verne*: The Mysterious Island (1874)*

This chapter has been adapted from:

Cullen M. Quine, Hillary L. Smith, Channing C. Ahn, Ariel Hasse-Zamudio, David A. Boyd, and Brent T. Fultz. Hydrogen adsorption and isotope mixing on copper-functionalized activated carbons. 2022. URL `https://doi.org/10.1021/acs.jpcc.2c02960`.

3.1 Chapter Overview

Hydrogen storage in physisorbent materials is fast, reversible, and highly efficient, yet the weak nature of adsorbate-adsorbent interactions with dispersion forces results in low hydrogen uptake at ambient temperatures. The figure of merit for physisorbent materials has generally been high specific surface area (SSA), with state-of-the-art materials currently around 3,000 m^2/g. Surface excess of H_2 adsorbed on carbon materials is assumed to be linearly proportional to SSA with a constant of proportion of 500 m^2/g per wt % at 77 K, resulting in about 6 wt % of H_2 for high surface area carbons.[1] Further increasing the hydrogen storage density requires materials with higher micropore volume, surface features, or surface

functionalization. To assess hydrogen storage in adsorbents, adsorption isotherms determine uptake capacity while the isosteric heat, known as the heat of adsorption, describes the adsorbate-adsorbent (hydrogen) interaction strength.

Recent work has focused on enhancing hydrogen uptake by increasing the isosteric heat by physical modification of pore structure or chemical modification of surface features. Synthesis of hierarchical carbons, such as templated carbon with near-optimal pore sizes for hydrogen storage, have raised the enthalpy of hydrogen adsorption of carbon materials above the 4-6 kJ/mole of bare graphite surfaces.[2, 3] Yang et al., showed that hydrogen adsorption at 298 K is dependent on micropore volume below 1 nm, further demonstrating the importance of pore morphology.[4] The modification of carbon materials with metals also has the potential to increase isosteric heat, and to increase packing density of H_2 on the surface. Chemical modifications result in enthalpies that are initially high, of order 15-16 kJ/mol, but decline with coverage as the less favorable sorption sites are filled. Modifications to MOF-74, a Zn-based material, showed an increase in Henry's law uptake of hydrogen along the $3d$ transition series, with the maximum heat of sorption for a Ni compound, for reasons yet unclear.[5] In the Henry's Law regime, the isosteric heat of adsorption is high, maintaining a quantity of adsorbed gas that is proportional to the partial pressure of adsorbent in the gas phase. High Henry's Law values are typically caused by deeper potential energy wells from micropores or coordinatively unsaturated metal centers in coordination polymers such as metal organic frameworks.[6–8] Additional work on functionalization of

high surface area carbons with precious metals [9–13] and transition metals [14–16] have mixed reports of improvement of adsorption capacity from functionalization. Studies reporting metal-doping of activated carbon have demonstrated improved hydrogen uptake at ambient temperatures, but open questions remained about how the dispersity of the metal affected adsorption capacity.[15]

This work determines the nature of hydrogen uptake enhancement at various temperatures in metal modified adsorbents with three approaches. First, the impact of transition metal functionalization on adsorption capacity in high SSA carbons as a function of temperature is quantitatively assessed. This is achieved through measurements of adsorption isotherms at temperatures ranging from 77-343 K and up to 10 MPa, at high resolution up to 0.1 MPa, and comparison of these isotherms to models. Second, the mechanism of adsorption of H_2 on these metal-functionalized carbons is determined, including how this mechanism differs as a function of temperature. This is achieved with temperature-programmed desorption measurements quantifying desorption temperatures and relative quantities of adsorbed species in pristine high SSA carbon and metal-functionalized carbon. Third, the decline in enthalpies in the Henry's Law regime observed in metal-functionalized materials as a function of pressure is explained from isotope-mixing experiments which discriminate between chemisorption and physisorption as a function of temperature.

Two distinct sorption behaviors are observed, corresponding to high temperature chemisorption and low temperature physisorption on the metal-functionalized carbons. By comparing isotherm results of the metal-functionalized and pristine

carbons, conditions are determined where copper modification of carbon adsorbents may be beneficial for hydrogen storage. In particular, these materials have potential for applications of hydrogen storage where cryogenic temperatures are not possible, or where gravimetric capacity is a lower priority. This work shows that copper functionalization offers enhanced uptake properties over unmodified carbons due to the unique binding properties of hydrogen on copper. The enthalpy of adsorption of chemisorbed hydrogen on nanoclusters of copper is lower than that of typical metal hydrides, making an unusual carbon-based material that shows both dissociative and molecular sorption behavior at ambient temperatures and pressures.

3.2   Methods

Metal-functionalized carbon was synthesized by wet chemical deposition of copper onto MSC-30, a super-activated carbon from Kansai Coke & Chemical Co. $Cu(NO_3)_2*2.5H_2O$ from Sigma-Aldrich was dissolved in water with different concentrations and centrifuged with the activated carbon at 3000 RPM for 1 hour. The solution was then evaporated overnight, leaving dried material with deposited metal salt. For each batch, the material was heated under flowing H_2 gas for 3 hours at 200°C. Thermal gravimetric analysis (TGA) was performed on the precursor salts to determine salt dissociation temperature. X-ray fluorescence spectroscopy was used to determine carbon-to-copper atomic ratios in the synthesized material.

A Micrometrics Tristar II 3020 was used for specific surface area (SSA) measurements using the BET method and was modified to conduct high precision H_2 isotherm measurements at sub-atmospheric pressures between 77 K and 343 K. The

as-received activated carbon, denoted as "pristine MSC-30," has a specific surface area of 3350 m^2/g. "MSC-30 High Cu" denotes material with SSA of 2174 m^2/g and C:Cu ratio of 36:1. "MSC-30 Low Cu" has a SSA of 2943 m^2/g and C:Cu of 43:1. MSC-30 Low Cu is a high surface area material with lower copper content, while MSC-30 High Cu has a higher copper content and lower surface area (see Table 3.1). Control samples of copper nanoparticles (denoted as Cu NP, 20 nm particle size) were purchased from Sigma-Aldrich with a SSA of 8.18 m^2/g.

For higher-pressure isotherm measurements, a custom Sieverts apparatus was used with the Helmholtz equation of state for normal hydrogen in REFPROP NIST Standard Reference Database to determine excess hydrogen uptake.[17, 18] The sample was pre-treated between each measurement with 0.2 MPa ultra high purity hydrogen (used throughout, unless otherwise specified) at ambient temperature for at least 12 hours, evacuated, and heated to 150°C for 30 minutes (3 hours for initial run) under active pumping.

The temperature programmed desorption (TPD) measurement protocol was adapted from Panella et al., who conducted TPD experiments on physisorbitive carbon materials.[19] The TPD measurements used a residual gas analayzer (RGA), a Stanford Research System RGA100, to determine desorption temperatures and relative adsorption quantities. Isotope exchange experiments were used to determine the mechanism for gas-surface binding. Previous studies have shown HD formation after protium and deuterium exposure on metal surfaces due to dissociative adsorption.[20, 21]. After the sample was cooled to ambient temperature under

active pumping, it was dosed with hydrogen at 0.2 MPa at ambient temperature for at least 12 hours. The reactor was submerged in liquid nitrogen for 15 minutes, and evacuated to ~1 mPa, leaving only hydrogen that was adsorbed onto the surface. The reactor was then transferred under liquid nitrogen to a residual gas analyzer, where it was passively heated to 229 K by removal from LN_2 and actively heated to 420 K using a heater controller at a ramp rate of 5 K per minute under active pumping. Partial pressures of gases in the residual gas analyzer chamber were measured simultaneously with temperature as a function of time. Temperature was linearly interpolated to determine gas signal strength as a function of temperature. Temperature corrections were applied to the results using an internal thermocouple to account for thermal lag through the stainless steel reactor using pure activated carbon as the calibration medium (see SI).

3.3   Results

Figure 3.1 shows scanning electron microscopy (SEM)and transmission electron microscopy (TEM) images of MSC-30 High Cu at two magnifications. Brightly colored circles in the bottom micrograph are copper, indicating clusters of size 10-20 nm.

Figure 3.2 shows hydrogen signals from TPD runs for pristine MSC-30, MSC-30 High Cu, as received pure copper nanoparticles, and a copper surface TPD study from Genger et al.[22] The pristine MSC-30 has one peak centered at 118 K, the copper nanoparticles and copper surface runs from Genger et al., have peaks at 312 K and 298 K, respectively, and MSC-30 High Cu has two peaks, one at 121 K
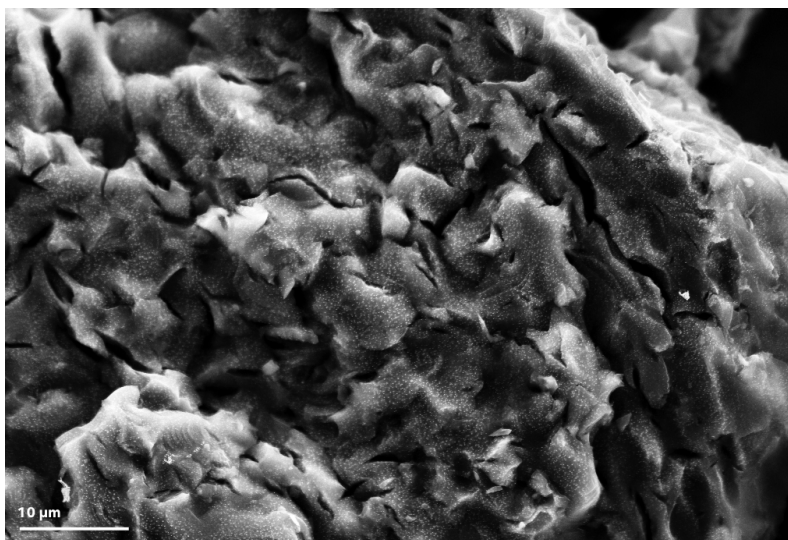
(a) 5 kX SEM
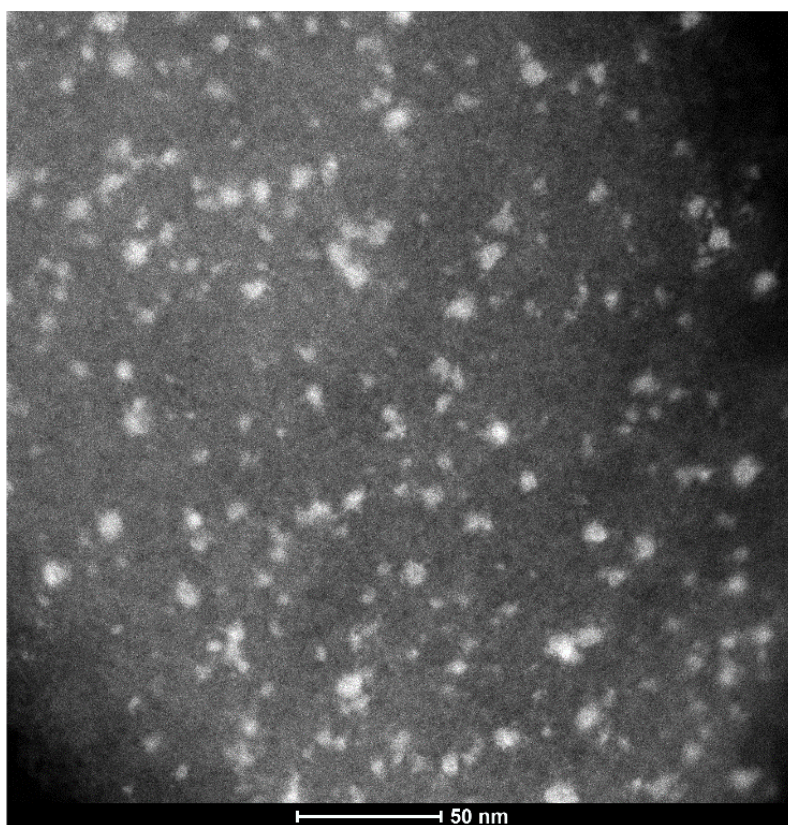
(b) TEM

Figure 3.1: SEM (top) and TEM (bottom) micrographs of MSC-30 High Cu at two magnifications. Bright spots show copper particles.
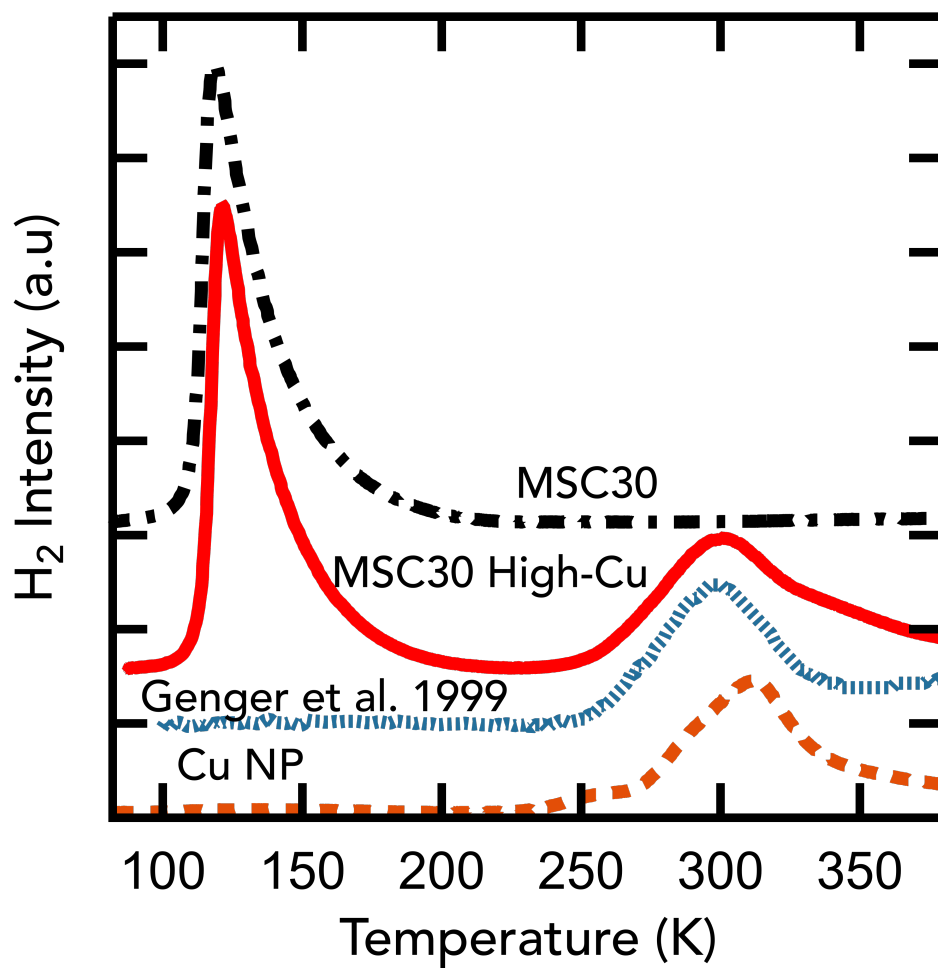
Figure 3.2: TPD runs on an activated carbon (pristine MSC-30), a metal modified activated carbon (MSC-30 High Cu), copper nanoparticles (Cu NP), and copper surfaces from Genger, et al.[22] The magnitude of the signals are scaled to the MSC-30 High Cu run, normalized to the low temperature peak height. Traces are offset vertically for clarity.
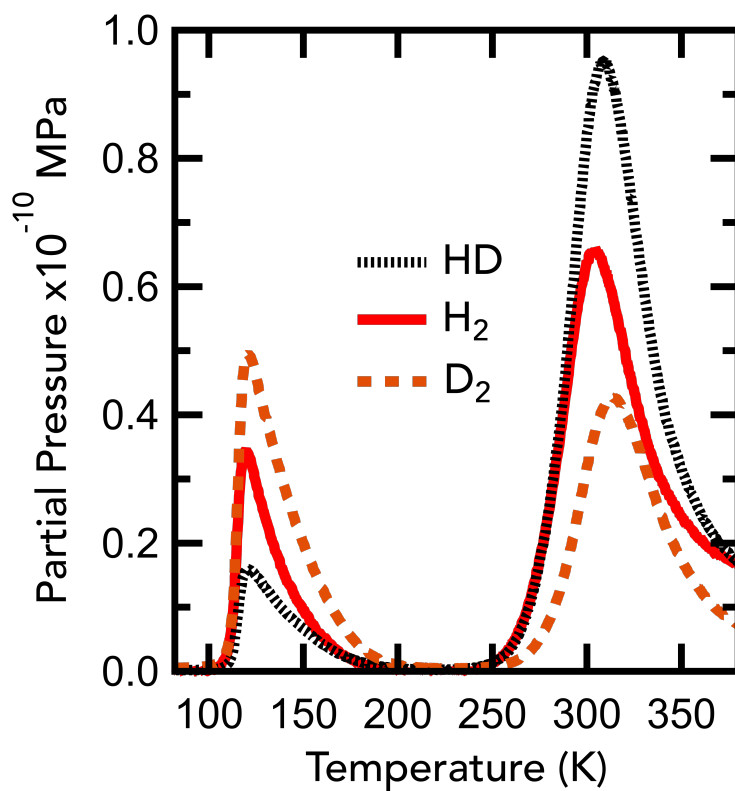
Figure 3.3: TPD isotope mixing experiment with a gas loading of 2.1:1 hydrogen to deuterium on MSC-30 Low Cu.

and 302 K. Reference copper sample was loaded at atmospheric pressure and other materials were loaded at 0.2 MPa.

Figure 3.3 shows results from an isotope mixing experiment, where a sample of MSC-30 Low Cu was dosed with a 2.1:1 hydrogen to deuterium mixture at a loading pressure of 0.2 MPa. For the lower temperature desorption event, more deuterium molecules were released than hydrogen and hydrogen-deuterium molecules, while the higher temperature gave primarily hydrogen-deuterium molecules. The peak temperatures for the high temperature desorption events were 304 K, 309 K, and 314 K for hydrogen, hydrogen-deuterium, and deuterium, respectively.
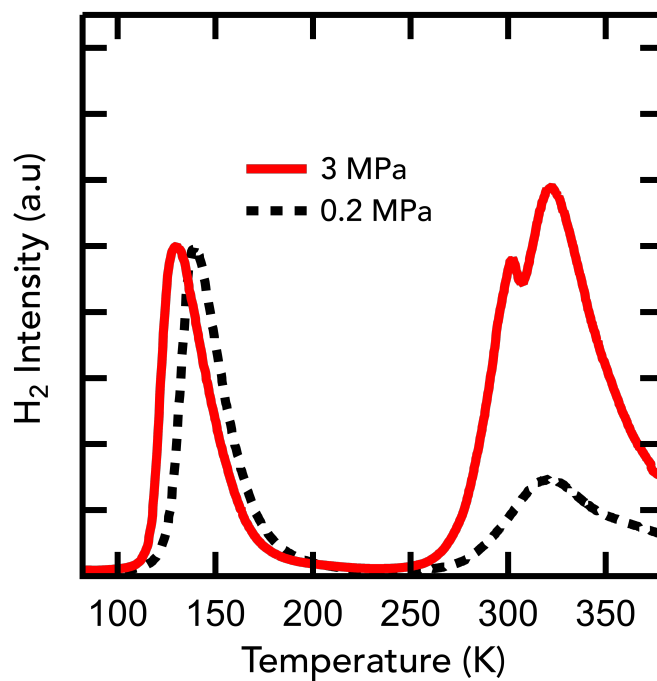
Figure 3.4: TPD experiment on MSC-30 High Cu with two different gas loading pressures of hydrogen. Data were normalized to the maximum value of the low temperature peak.

Figure 3.4 shows MSC-30 High Cu sample under an initial gas loading pressure of 0.2 MPa and 3 MPa. The ratio of the area of the high temperature peak to the area of the lower temperature peak increases with dose pressure, even with both samples being evacuated to similar baseline pressures after cooling with liquid nitrogen, indicating a larger desorption of hydrogen from higher initial gas pressure.

Figures 3.5 and 3.6 are high pressure and cryogenic (77 K) adsorption measurements on a Sieverts apparatus, compared to pristine MSC-30 and copper nanoparticles (Cu NP). MSC-30 High Cu has 68% of the specific surface area of pristine MSC-30, and has less uptake at 77 K and 298 K. Nevertheless, at 298 K MSC-30 High Cu has greater excess uptake per surface area than MSC-30.
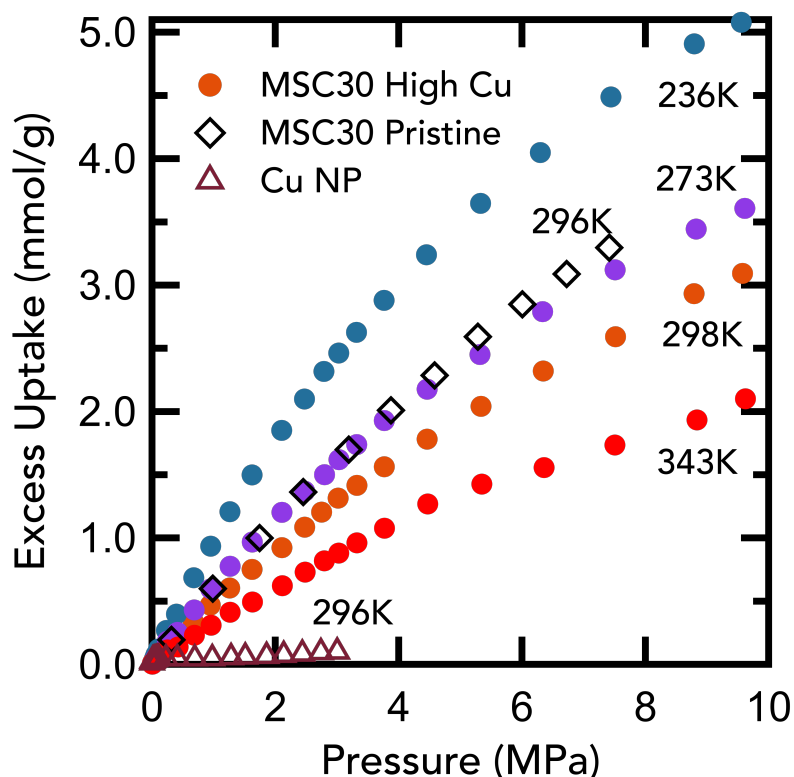
Figure 3.5: Sieverts isotherm measurements on MSC-30 High Cu (solid circles) and copper nanoparticles (open triangles) at 296 K up to 10 MPa at temperatures labelled on graph. Data are compared to pristine MSC-30 at 296 K (open diamonds) from Stadie, et al.[13]

Figure 3.7 shows low pressure (<0.1 MPa) excess uptake isotherms on MSC-30 High Cu at different temperatures, and an ambient temperature pristine MSC-30 run. The data are fit with a power law with the exponent for each curve indicated on the plot. Most values are near 1, but MSC-30 High Cu deviates significantly from 1 at 296 K.

MSC-30 High Cu has significantly lower specific surface area than the pristine MSC-30. Since the excess uptake of hydrogen on carbon scales with specific surface area, a comparison was made with MSC-30 High Cu to pristine MSC-30
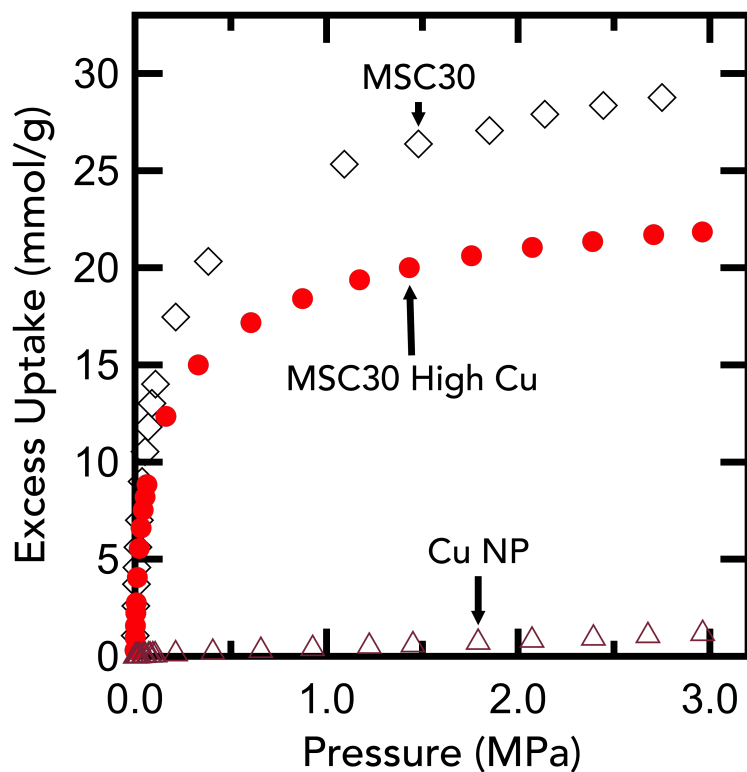
Figure 3.6: Sieverts isotherm measurements on MSC-30 High Cu (solid circles), pristine MSC-30 (open diamonds), and copper nanoparticles (open triangles) at 77 K up to 3 MPa.

with reduced specific surface area. Figure 3.8 shows improvements of the hydrogen excess uptake of MSC-30 High Cu over pristine MSC-30 uptake renormalized based on MSC-30 High Cu surface area. The percentage improvement ranges from 80% at 300 K to 15% at 77 K.
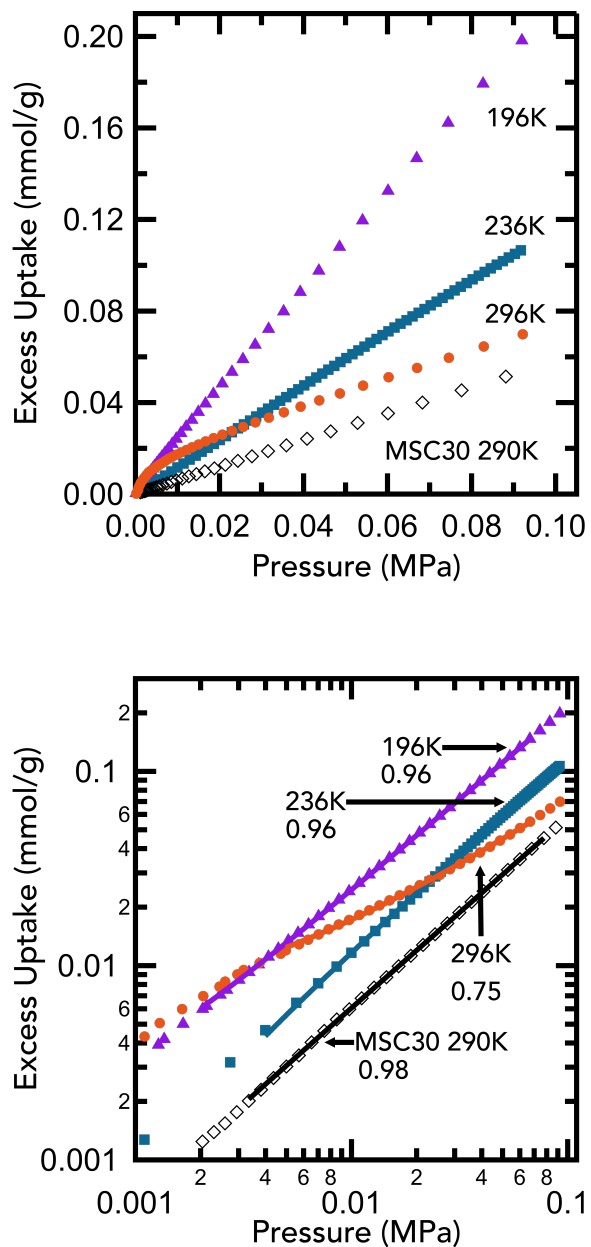
Figure 3.7: Low pressure isotherm measurements on MSC-30 High Cu at different temperatures relative to pristine MSC-30 at ambient conditions. Data plotted on a linear scale (top) and log-log plot (bottom) with temperature and power denoted from a power law fit (solid lines).
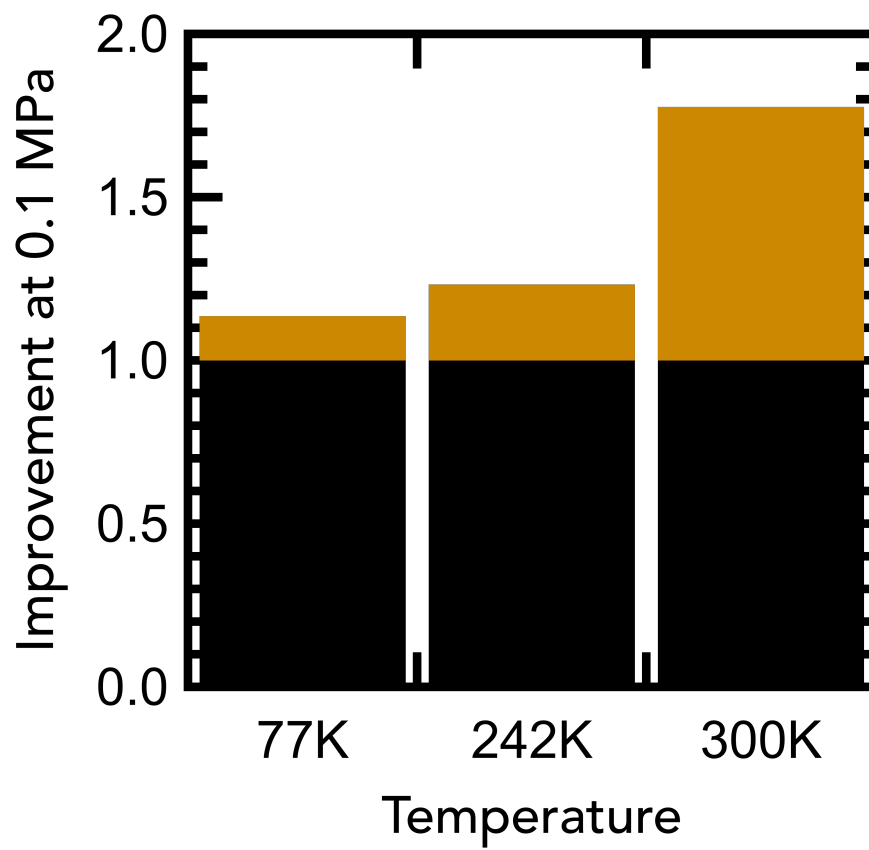
Figure 3.8: Hydrogen excess uptake improvement of MSC-30 High Cu at 0.1 MPa pressure (gold) over pristine MSC-30 with uptake normalized based on SSA of MSC-30 High Cu (black).

3.4   Discussion

Langmuir Isotherms

The primary binding mechanism for gas adsorption on carbonaceous adsorbents is through "dispersion forces," or van der Waals interactions, known as physisorption. These forces are relatively weak, resulting in low desorption temperatures. The thermodynamic "Langmuir isotherm" describes the adsorption behavior of physisorbed species at fixed temperature, based on the assumptions:

1. There is only one energy, ε_{H_2}, which is the binding energy of one gas molecule to one surface site. Binding is favorable, so $\varepsilon_{H_2} < 0$.

2. The sorbent material has a fixed number of surface sites, and the adsorbed molecules have a random distribution over these sites.

3. There is no interaction between the molecules adsorbed on the surface.

4. The gas is assumed an ideal gas, simplifying the treatment of the chemical potential of molecules in the gas phase.

These assumptions give the Langmuir isotherm [23]

$$\theta = \frac{K_{p,1}(T)P}{1 + K_{p,1}P} \, , \tag{3.1}$$

where

$$K_{p,1}(T) = \frac{\lambda_g^3(T)q(T)}{k_B T} e^{-\beta\varepsilon_{H_2}} \tag{3.2}$$

and $\beta = \frac{1}{k_B T}$. Here ε_{H_2}, p, T, $\lambda_g^3(T)$, k_B, and $q(T)$ are the molecular binding energy, pressure, temperature, quantum volume, Boltzmann's constant, and the

vibrational and translational adsorbent partition function, respectively. Both the
quantum volume and the partition function are temperature dependent (see SI for
details). Because the surface sites are non-interacting, all sites have the same
probability of occupancy, θ. Therefore θ is the surface coverage, or the fraction
of sites occupied by gas molecules. The surface coverage increases with pressure,
reaching an asymptotic value of 1.

Carbon materials are known to physisorb gases, but metals can have chemisorption phenomena. Many metals readily form metal-hydrides, reacting with H_2 to
absorb hydrogen into the metal. However, hydrogen does not diffuse into bulk
copper at ambient temperature, preventing the formation of bulk copper hydrides.
Instead, molecular H_2 readily dissociates to chemically bond with copper surfaces in
the form of atomic hydrogen, in an independent dissociation process that is assumed
not to affect the surface coverage. At ambient conditions, the ratio of surface to bulk
hydrogen species in copper is 8000:1. [24].

For dissociative adsorption, there are two atoms instead of one that need to
have probabilities of surface sorption. The Langmuir isotherm for dissociative
chemisorption now has the form (see Chapter 2 for derivation):

$$\theta = \frac{\sqrt{K_c(T)P}}{1 + \sqrt{K_c(T)P}} \tag{3.3}$$

where

$$K_c(T) \equiv \frac{\lambda_g^3(T)q_2^2}{k_BT}e^{-2\varepsilon_H/k_BT} \tag{3.4}$$

and ε_H is the binding energy of a dissociative hydrogen site.

A Comparison of Isotherms

The Langmuir isotherm used to describe physisorption (Eq. 3.1), and dissociative isotherm used to describe chemisorption (Eq. 3.3), were combined into a double-site Langmuir equation (Eq. 3.12 in SI). Sieverts isotherms from MSC-30 High Cu and the low pressure 296 K isotherm were fitted to this equation, showing good agreement with the experimental isotherms over 5 orders of magnitude in pressure. The low pressure 296 K isotherm data is shown with the individual components of adsorption in Fig. 3.9. At low pressures and low coverage, the coverage θ goes as P for the molecular Langmuir isotherm, and as $\sqrt{P}$ for the dissociative case. In this limit, the Langmuir isotherm has a linear slope, while the slope in the dissociative case has an infinite slope at infinitesimal coverage. At low coverage, the dissociative hydrogen adsorption is a significant portion of the excess uptake, and a crossover between molecular and dissociative excess uptake is observed at 45 kPa, 296 K in Fig. 3.9. The dissociative component of θ reaches saturation at lower pressures than the molecular component. Only 0.4% of the total sites are dissociative, based on the fitting parameters (see Table 3.2), and at high pressures the chemisorbed sites are an insignificant portion of the excess uptake. Using the fitting parameters and Eq. 3.14 and Eq. 3.15 in the SI, there are 14:1 copper per hydrogen atoms at full coverage on chemisorption sites, with a copper specific surface area of 86 m^2/g.
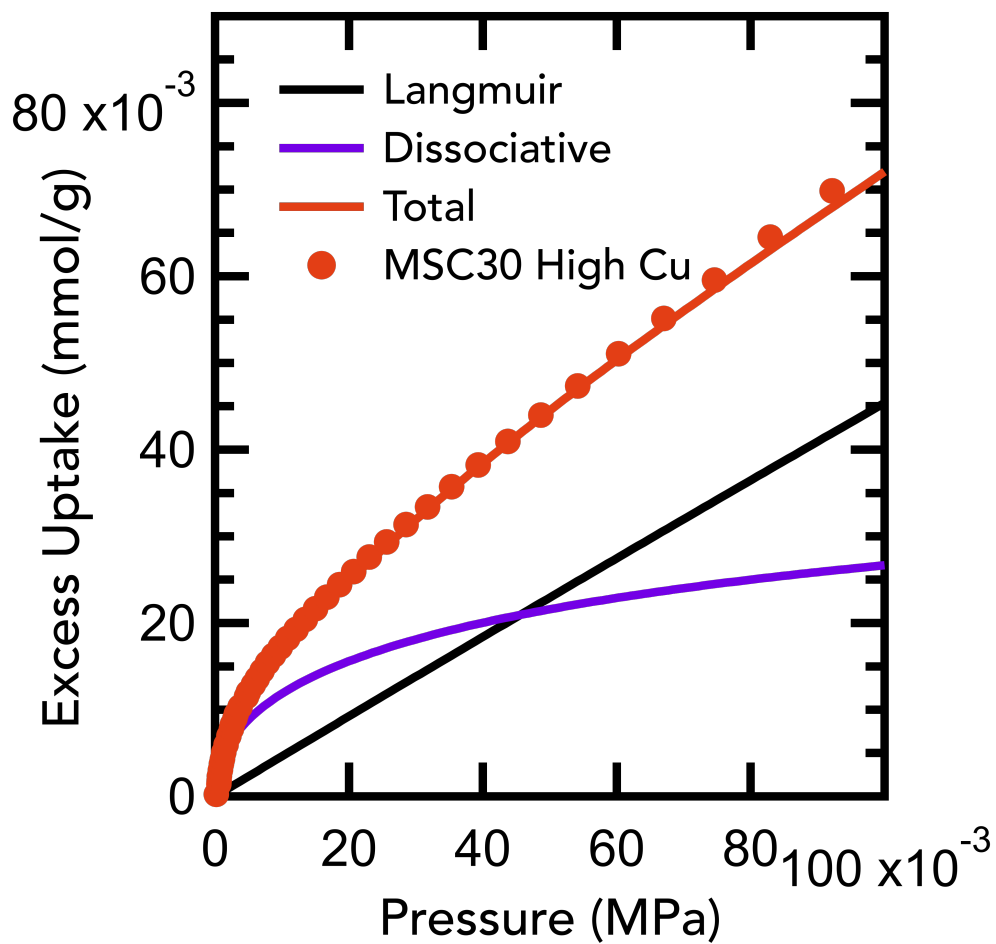
Figure 3.9: MSC-30 High Cu Excess uptake (solid circles) with total double-site dissociative Langmuir fit partitioned into the normal molecular Langmuir and dissociative components (solid lines) at 296 K. Fitting parameters are provided in Table 3.2

Mechanisms of Adsorption

The temperature programmed desorption (TPD) experiments help elucidate both the binding strength of hydrogen in these materials and the mechanisms of H_2 adsorption. Fig. 3.2 indicates that in pristine carbon, hydrogen is primarily released at a low temperature, while pure copper releases surface hydrogen near ambient temperature. For our copper modified samples, we see a superposition of these two behaviors. At equilibrium, the difference in Gibbs free energy between the adsorbed species and the gas phase, ΔG, is zero, where

$$\Delta G = \Delta H - T\Delta S, \tag{3.5}$$

where ΔH and ΔS are the change in the enthalpy and entropy between the adsorbed and gas phase, respectively. A commonly used approximation is that the gas phase entropy is much larger than the adsorbed phase entropy, so that $\Delta S \approx S_{gas}$. With this approximation, the desorption temperature is determined by the difference in the adsorption enthalpy and the energy required for the transition desorption state. With similar transition states, a higher desorption temperature observed from TPD measurements indicates a higher adsorption enthalpy, which is characteristic of stronger binding of adsorbed gas species. The presence of a high temperature peak near 310 K in MSC-30 High Cu indicates the presence of hydrogen binding sites with increased adsorption enthalpies that are not present in unmodified carbon.

The mechanism of adsorption in these materials is revealed by the isotope experiment shown in Fig. 3.3. The copper-modified carbon sample (MSC-30 Low Cu) was dosed with D_2 and H_2 at room temperature and allowed to interact with

the sample for 12 hours, when hydrogen and deuterium can absorb to the surface as molecules, and also dissociate during absorption. The sample is then cooled to 77 K and evacuated to remove H_2 and D_2 in the gas phase. The evolved gas species are observed as the temperature is increased.

The low temperature desorption event gives mostly D_2, with HD molecules being the least abundant species. This indicates physisorption behavior, where molecular hydrogen does not dissociate during adsorption on the carbon surfaces. Curiously, there is more D_2 observed than H_2, even though the sample was dosed with a 2:1 ratio of H_2 to D_2. This can be attributed to a quantum sieving effect in porous carbons, where nanoporous structures preferentially store more D_2 than H_2 based on adsorption kinetics and zero point energies of the heavier molecule[25, 26]. The zero point energy differences between H_2 and D_2 can also be seen by the slight increase in the peak desorption temperature as molecular mass increases, indicating that D_2 has a slightly higher enthalpy of adsorption than H_2.

The high temperature desorption event gives primarily HD molecules. This peak is associated with hydrogen adsorption onto copper, which is characteristic of recombination of dissociated species in chemisorption. This is consistent with hydrogen storage on pure copper surfaces, as noted in the literature. Yasumori et al., claim that there is complete isotope mixing of H_2 and D_2 on copper surfaces, and reversible hydrogen adsorption of temperatures from 273-333 K and 7 KPa pressures.[27] The clustering of copper atoms in our materials prevented the formation of unsaturated metal surface sites. MSC-30 High Cu has an adsorption

enthalpy of 7.5 kJ/mole H_2 determined from excess isotherm data (see Fig. 3.19 and 3.20 in SI). Binding energies of 6 kJ/mole H_2 and 20 kJ/mole H for molecular and dissociative sites, respectively, were obtained using a double-site Langmuir fit to experimental isotherms (Eq. 3.12 in SI). This is significantly less than the 78 kJ/mole H_2 observed for bulk copper surfaces.[22]. A recent study on a copper-loaded covalent organic framework (COF) showed a desorption event near 323 K attributed to molecular hydrogen binding on Cu^{1+} sites (determined using XANES), with an adsorption enthalpy 15 kJ/mole H_2.[28] From our results, even though hydrogen is dissociating on the copper metal clusters, there is no significant isotope mixing measured for the underlying carbon material. Adsorption on carbon only occurs when the sample is cooled to 77 K (very little at ambient temperature). Our measurements began by cooling the H_2/D_2 mixture from 298 K, so some dissociation may be expected. However, the hydrogen pressure was under 0.2 MPa so few recombination events of chemisorbed hydrogen occur at 298 K. A prior study of isotope mixing on copper in the gas phase at 273 K reported an insignificant amount of HD formation.[29] Braunecker et al., also reported that dosing their copper COF below 273K resulted in no high temperature desorption due to a thermal activation barrier.[28] From the results shown in Fig. 3.4, the copper adsorbs more hydrogen at high loading pressure, demonstrating that the amount of chemisorbed hydrogen increases with loading pressure.

Sorption Enhancement from Copper Functionalization

There is evidence that the copper has enhanced the storage on the underlying carbon structure, depending on pressure. However, there is no significant improvement of MSC-30 High Cu in Sieverts measurements at high pressures compared to the pristine carbon material (Fig. 3.5, even with accounting for surface area differences). This lack of enhancement at high pressure was also observed with platinum doped activated carbons.[13] Nevertheless, there is a substantial improvement at ambient pressure. Fitting MSC-30 High Cu adsorption data to a simple power law in Fig. 3.7 (following Henry's Law), gives a power of 1 for the 196 K and 236 K adsorption data, and 1 at ambient temperature for the pristine MSC-30. Fitting the MSC-30 High Cu 296K isotherm gives a power of 0.7. This shows the presence of both dissociative and standard Langmuir isotherms, as discussed with Fig. 3.9. An increase in the contribution from the chemisorption sites with temperature is expected from an energetically favorable chemisorption event with a dissociative activation energy.

From the systematics of standard physisorption, we expect that hydrogen uptake should be directly proportional to the SSA of the sample. We therefore normalized the 0.1 MPa pristine MSC-30 data to the SSA of our MSC-30 High Cu sample in Fig. 3.8 to compare our modified sample to an activated carbon with a similar surface area. There is a systemic improvement at all temperatures over a carbon with similar SSA, and the improvement is highest at ambient temperature. This is consistent with an activated chemisorption process as the copper in the sample

adsorbs more hydrogen at higher temperatures. The TPD results show hydrogen readily desorbs from MSC-30 High Cu at temperatures above 350 K. There is a temperature window above the thermally activated dissociation and below the desorption temperature which is optimal for hydrogen storage. This window of hydrogen adsorption for copper particles is centered around ambient temperature, making copper a promising metal for functionalization for ambient temperature, low pressure hydrogen storage.

3.5 Conclusion

The H_2 adsorption onto copper-functionalized high surface area carbon is assessed and compared to the adsorption properties of pristine high SSA carbon. Copper functionalization enhances storage by increasing H_2 binding enthalpy at ambient temperatures and low pressures, above what is achievable with pristine carbon materials of the same SSA. There is a window of enhanced adsorption behavior where gas molecules have enough thermal energy to overcome a dissociation activation energy barrier, yet low enough energy to still adsorb to the copper clusters. This occurs around ambient temperature. The expected low temperature desorption observed in pristine high SSA is also observed in the metal-functionalized material, and attributed to conventional physisorption on carbon. Near-ambient temperature desorption was observed in our functionalized material and in pure copper. Isotope mixing studies show that this sorption is dissociative in nature.

This work establishes the specific mechanism for adsorption of H_2 on metal-functionalized carbon is both physisorption and chemisorption at ambient pressures.

Binding energies of 6 kJ/mole and 20 kJ/mole for H_2 physisorption and H chemisorption, respectively, were extracted from double-site Langmuir fits on copper modified MSC-30 isotherms, resulting in 14:1 Cu:H. These results provide the specific conditions under which metal-functionalized materials may provide opportunities for hydrogen storage applications, such as in catalytic processes requiring dissociated hydrogen on surfaces or for metal hydrides that are kinetically limited by dissociation. Future development of metal-functionalization, by reducing the sizes of copper clusters may be a promising direction for use of these composite materials in some hydrogen storage applications.

3.6   Acknowledgements
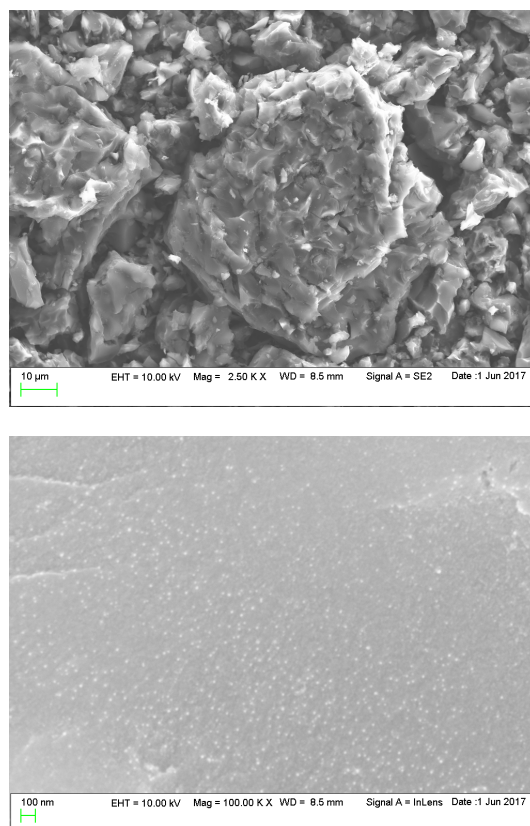
Figure 3.10: SEM micrographs of MSC-30 Low Cu at 2.5 kX (top) and 100 kX (bottom) magnification. Bright spots show copper particles.

Sample	BET SSA	Expected		XRF				TGA
	m²/g	C:Cu	Cu:C	C:Cu	Cu:C	at% Cu	wt% Cu	wt% Cu
Standard	-	111	0.00901	112.6	0.00888	0.88	4.5	5.4
MSC-30 High Cu	2174	150	0.00667	36.4	0.0275	2.67	12.7	12.0
MSC-30 Low Cu	2943	178	0.00562	42.76	0.0234	2.28	11.0	11.8

Table 3.1: Summary of physical and XRF measurement results. A standard sample of Graphimet (Alfa Aesar, No. 89688, Lot H22X034) is specified to have 4.5% copper on graphite. This sample was used as a calibration standard to baseline the Cu-$K_{\alpha2}$ fluorescence intensity with respect to the bremsstrahlung background. Copper wt% in the Cu-functionalized MSC-30 materials was determined from sampling over multiple areas of the material and averaging the fluorescence intensity. The wt% Cu is then calculated relative to the total sample mass. BET SSA determined from 77 K N_2 isotherms.

3.7 Supporting Information
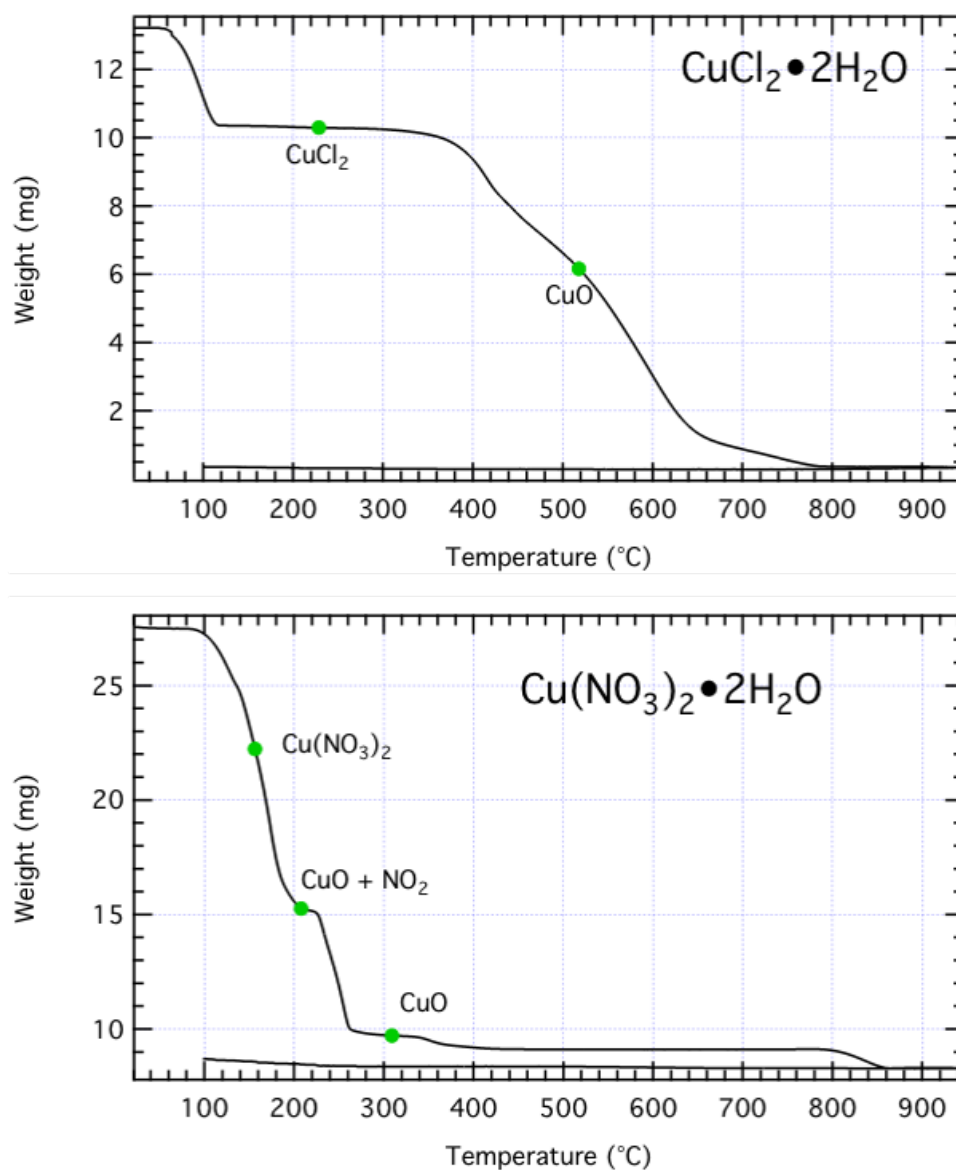
Figure 3.11: TGA (thermogravimetric analysis) under argon gas of the two salts used for copper functionalization was performed to determine what temperatures are necessary for removal of excess salt from functionalized carbons. $Cu(NO_3)_2 * 2.5H_2O$ has lower decomposition temperatures than $CuCl_2 * H_2O$, enabling lower temperature processing.
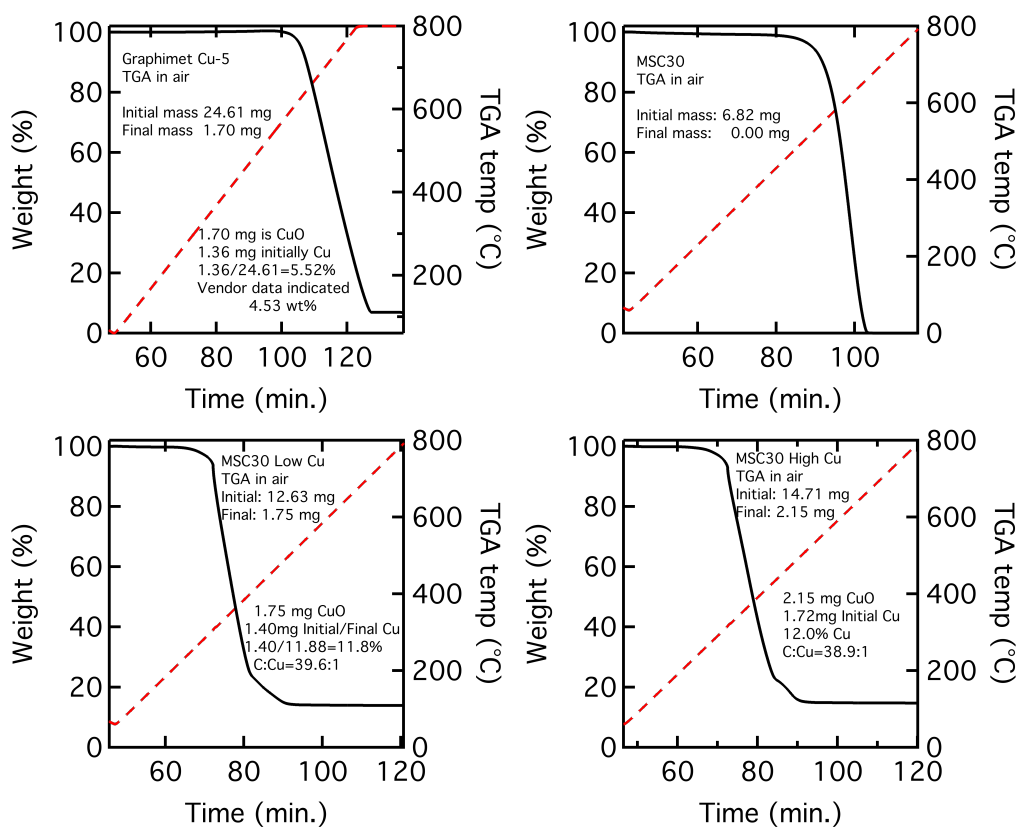
Figure 3.12: TGA (thermogravimetric analysis) under air of 5% copper on graphite sample (top left), pristine MSC-30 (top right), MSC-30 Low Cu (lower left) and MSC-30 High Copper (lower right) at 10 K/min to 800 °C. Samples were preheated under nitrogen to 400 K to remove adsorbed water. The calibration sample of Graphimet (Alfa Aesar) contains 4.5% copper on graphite and was assumed to be initally pure copper. The Cu-containing MSC-30 materials were assumed to be initally CuO after air exposure. All samples were treaded as fully oxidized after heating to 800 °C.
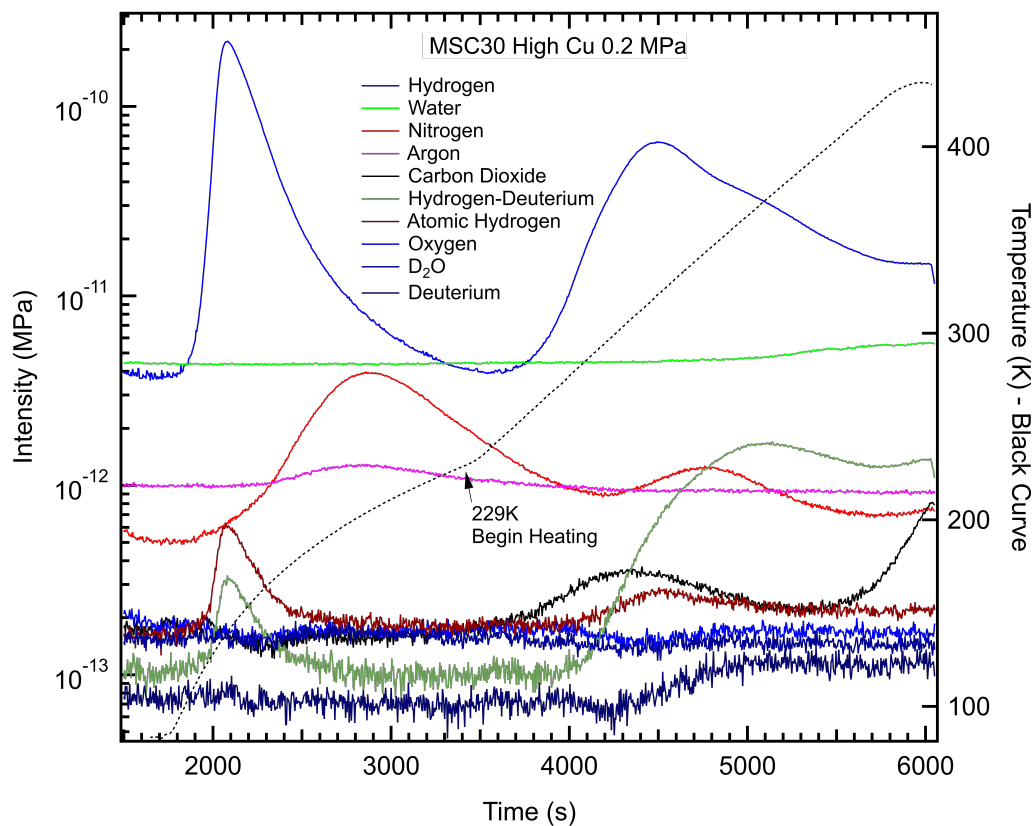
Figure 3.13: Partial pressure signals vs time for MSC-30 High Cu 0.2 MPa TPD run. The molecular hydrogen peak is approximately two orders of magnitude above all other measured gas species, demonstrating the purity of the adsorbed gas species from UHP hydrogen dosing.
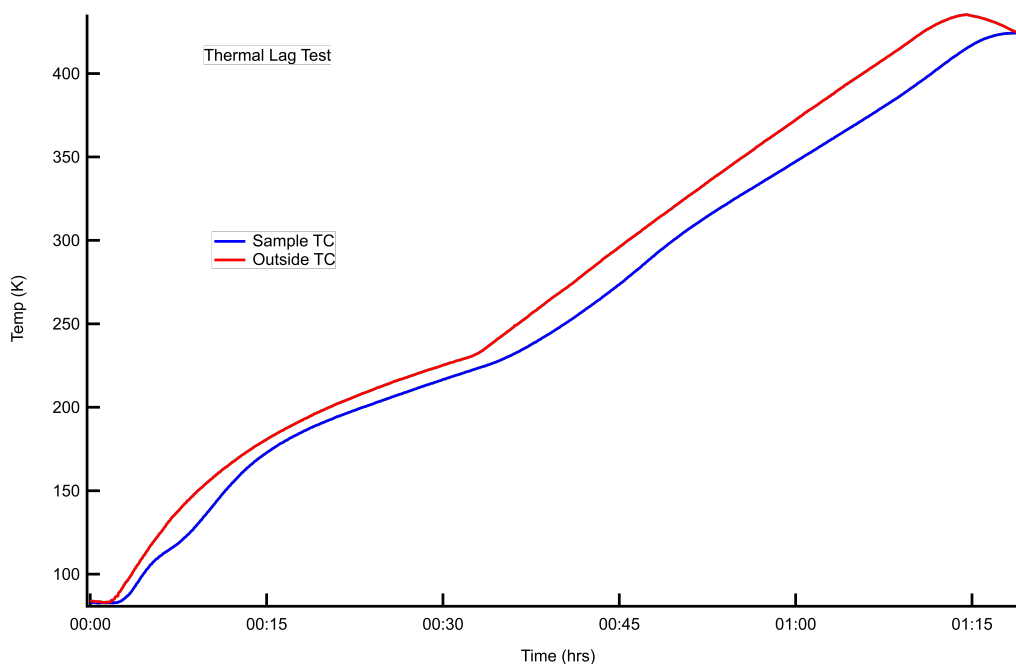
Figure 3.14: All of the temperature programmed desorption (TPD) runs were conducted using a thermocouple attached to the bottom of the stainless steel reactor. Both the temperature and the gas signals are collected as a function of time, which is then plotted as gas signal vs temperature. To take into account the thermal lag across the stainless steel, a calibration run was conducted by inserting a thermocouple into MSC-30 powder in the same evacuated reactor. The sample was heated using the same procedure as the TPD runs, and a mapping of the outer thermocouple to the powder bed was obtained as a function of time. This temperature calibration run was applied to the low temperature (<239 K, passive heating) and the high temperature (>239 K, active heating), obtaining gas signal as a function of temperature. The temperature dip around 120 K in the blue curve most likely corresponds to the desorption of hydrogen from MSC-30, which is endothermic.
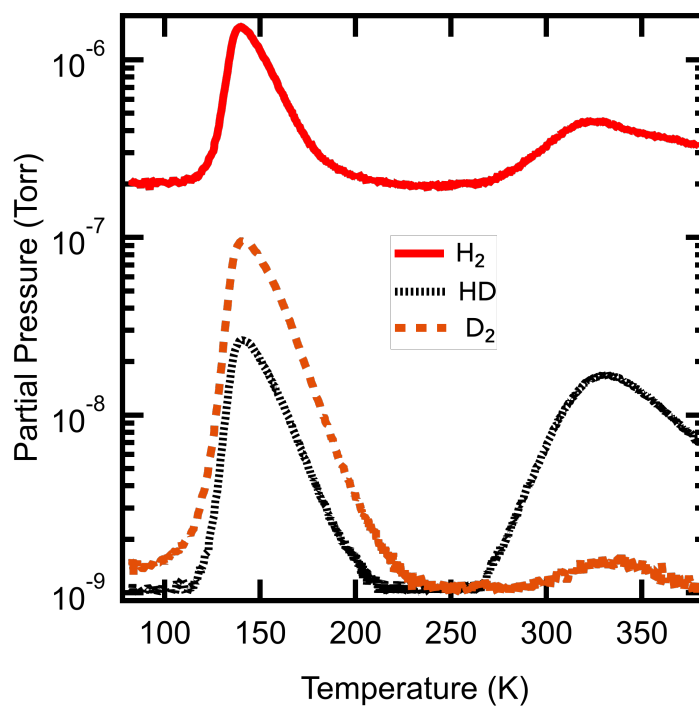
Figure 3.15: TPD isotope mixing experiment with a gas loading of 2.1:1 hydrogen to deuterium on MSC-30 High Cu.
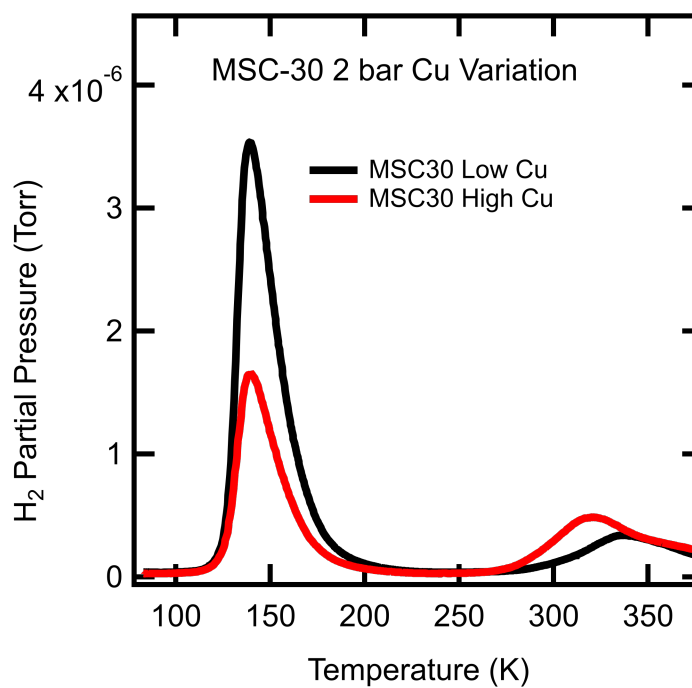
Figure 3.16: TPD H_2 experiments of both MSC-30 Low Cu and MSC-30 High Cu before normalization and temperature lag corrections.
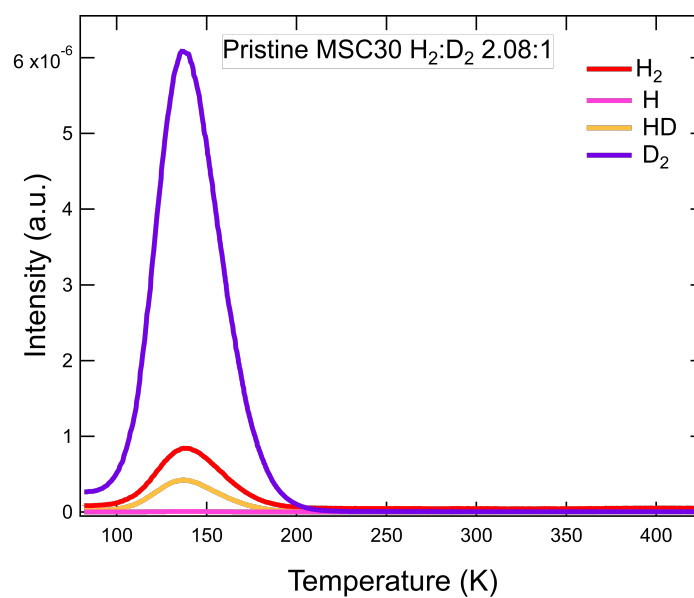
Figure 3.17: TPD isotope mixing experiment with a gas loading of 2.1:1 hydrogen to deuterium on pristine MSC-30. No significant dissociation is observed based on the low magnitude of the HD peak relative to other hydrogen species.

Double-Site Dissociative Langmuir Isotherm

The full Langmuir isotherm derivation for both physisorption and chemisorption is shown in Chapter 2, with relevant text reproduced here. The main assumptions made in this chapter for hydrogen adsorption is the partition function $q_1(T)$ is a product of a translational and vibrational component:

$$q = q_{vib}q_{trans}. \tag{3.6}$$

For molecular adsorption, if we assume a 2D adsorbed gas phase with an out of plane vibrational component (with the high temperature approximation for the vibrational component):[23]

$$q_{vib} = \frac{kT}{\hbar\omega} \tag{3.7}$$

$$q_{trans} = \frac{A_{B,1}}{\lambda_{ads}^2} \tag{3.8}$$

$$\lambda_{ads} = \left(\frac{2\pi\hbar^2}{m^* k_B T}\right)^{1/2} \tag{3.9}$$

where $\hbar$ is Planck's constant, ω is the vibrational frequency, $A_{B,1}$ is the effective binding area of an adsorption site, and λ_{ads} is the thermal de Broglie wavelength of the adsorbed molecule with effective adsorbed mass m^* such that $q(T) \propto T^2$. The thermal de Broglie wavelength of the adsorbed molecule is assumed to be negligibly different than the gas phase such that $\lambda_g = \lambda_{ads}$. The 2D translational model with a perpendicular vibrational mode is supported by quasi-elastic neutron scattering data on molecular hydrogen in activated carbon, showing fully mobile liquid-like hydrogen species on the surface above 150 K and an empirically-determined 15 meV vibrational mode of the center of mass of an adsorbed hydrogen molecule.[30, 31]

The vibrational internal degrees of freedom for hydrogen molecules are too high in energy to be excited at the temperature range of interest and are therefore ignored.

For the chemisorption partition function $q_2(T)$, we assume localized bonding to a simple site, so the translational component of the adsorbed phase is negligible and we assume a high vibrational energy of hydrogen on copper. The vibrational entropy is not temperature dependent (the quantum oscillator is primarily in the ground state) and $q_{vib}(T) \simeq 1$. This assumption is supported by $h\nu \approx 129$ meV perpendicular and $h\nu \approx 100$ meV in-plane vibrational energy of atomic hydrogen on copper determined using EELS.[32] The translational and vibrational partition function will be assumed to be independent of temperature.

With these assumptions for the partition functions, the physisorption and chemisorption Langmuir constants become (from Eq. 2.18 and Eq. 2.19):

$$K_{p,1} = A_{B,1} \frac{\lambda_g}{\hbar\omega} e^{-\beta\varepsilon_1} = \frac{A_1}{\sqrt{T}} e^{-\beta\varepsilon_{H_2}} \tag{3.10}$$

$$K_c(T) \equiv \frac{\lambda_g^3(T)q_2^2}{k_B T} e^{-2\varepsilon_H/k_B T} = \frac{A_2}{T^{5/2}} e^{-2\beta\varepsilon_H} . \tag{3.11}$$

Experimentally, excess hydrogen uptake n_e is measured, which is the amount of gas that the material adsorbs over the gas phase with the same empty space.[33] To fit excess data to an absolute isotherm, the gas phase contribution in adsorbed volume $v_m\theta$ must be added back into the excess data (using the gas density ρ_g). The full double-site Langmuir molecular-dissociative isotherm model (combining Eq. 2.20 and Eq. 2.26) is

$$n_e(P,T) = (n_m - \rho_g(P,T)v_m)\left((1-\alpha)\frac{K_{p,1}(T)P}{1 + K_{p,1}(T)P} + \alpha \frac{\sqrt{K_c(T)P}}{1 + \sqrt{K_c(T)P}}\right) \tag{3.12}$$

where K_p and K_c are the physisorption and chemisorption Langmuir constants defined above, respectively, P is pressure, T is temperature, ρ_g is the gas phase density, n_m is the maximum absolute uptake at full coverage, and α is defined as the fraction of chemisorption sites.

Adsorption Enthalpies from Double-Site Langmuir Fits

From the absolute uptake it is possible to calculate thermodynamic properties such as the adsorption enthalpy Δh.[34] We can use Eq. 2.47 to get the heat of adsorption -Δh_{ads}:

$$q_{st} \equiv -\Delta h_{ads} = -T \left(\frac{\partial P}{\partial T}\right)_{n_a} \left(\frac{v_m}{n_m} - \frac{1}{\rho_g}\right) \tag{3.13}$$

$$-\left(\frac{\partial P}{\partial T}\right)_n = \frac{\left(\frac{\partial \theta}{\partial T}\right)_{P,n}}{\left(\frac{\partial \theta}{\partial P}\right)_{T,n}} \tag{3.14}$$

$$\frac{\partial \theta}{\partial P} = (1 - \alpha)\left(\frac{K_{p,1}}{(1 + K_{p,1}P)^2}\right) + \alpha\left(\frac{K_c}{2\sqrt{K_cP}(1 + \sqrt{K_cP})^2}\right) \tag{3.15}$$

$$\frac{\partial \theta}{\partial T} = (1 - \alpha)\frac{\partial \theta}{\partial K_{p,1}}\frac{\partial K_{p,1}}{\partial T} + \alpha\frac{\partial \theta}{\partial K_c}\frac{\partial K_c}{\partial T} \tag{3.16}$$

$$\frac{\partial \theta}{\partial K_{p,1}}\frac{\partial K_{p,1}}{\partial T} = -\left(\frac{P}{(1 + K_{p,1}P)^2}\right)(xRT + \varepsilon_{H_2})\frac{K_{p,1}}{RT^2} \tag{3.17}$$

$$\frac{\partial \theta}{\partial K_c}\frac{\partial K_c}{\partial T} = -\left(\frac{P}{2\sqrt{K_cP}(1 + \sqrt{K_cP})^2}\right)(xRT + 2\varepsilon_H)\frac{K_c}{RT^2} \tag{3.18}$$

where the gas constant R has been substituted in for k_B to get energy per mole of adsorbate, and the binding energies ε_H and ε_{H_2} are negative for adsorption. The power of the prefactor temperature dependence is determined from the adsorbate partition function, and in our case, $x = 0.5$ for the physisorption terms and $x = 2.5$ for the chemisorption term.
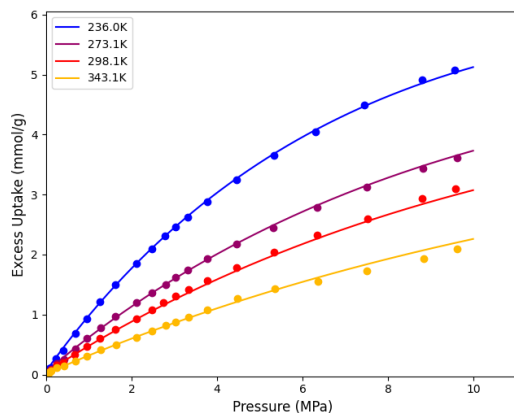
Figure 3.18: Double-site Langmuir isotherm fits for MSC-30 High Cu using Eq. 3.12 and parameters from Table 3.2. Experimental data shown in markers with excess uptake fit in solid lines.

n_m	v_m	α	A_1	ε_{H_2}	A_2	ε_H
mmol/g	mL/g		$K^{1/2}$/MPa	kJ/mol	$K^{5/2}$/MPa	kJ/mol
18.0	0.778	0.00373	0.035	-6.3	0.69	-19.8

Table 3.2: Fitting parameters for double-site molecular and dissociative Langmuir on MSC-30 High Cu.

From the fitting parameters the amount of copper per adsorbed hydrogen Cu:H is

$$\text{Cu:H} = \frac{wt\%_{Cu}}{2\alpha n_m M_{Cu}} \tag{3.19}$$

where M_{Cu} is the molar mass of copper (63.546u), a factor of 2 for atomic hydrogen, and the weight percent of copper $wt\%_{Cu}$. Using the values from Tables 3.1 and 3.2, there are 14:1 copper to hydrogen atoms for MSC-30 High Cu at saturation.

The copper-specific surface area SSA_{Cu} is determined from the chemisorbed hydrogen uptake:[22]

$$\text{SSA}_{Cu} = \frac{4\alpha n_m N_A}{A_{Cu} wt\%_{Cu}} \tag{3.20}$$

where hydrogen saturation on surface copper is 2:1 Cu:H, N_A is Avogadro's number, A_{Cu} is the surface packing density of copper atoms ($1.47*10^{19}$ Cu atoms/m^2).[22]

Using the values from Tables 3.1 and 3.2, MSC-30 High Cu has a copper specific surface area of 86 m^2/g Cu.
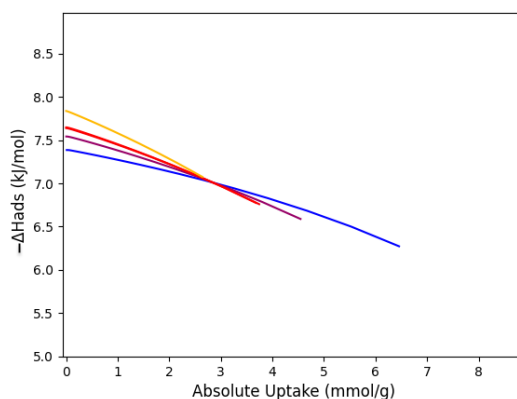
Figure 3.19: Isosteric heat of adsorption of MSC-30 High Cu vs absolute adsorbed uptake calculated from the double-site Langmuir fit using Eq. 2.47 with the same temperatures as Fig. 3.18.

Determination of Isoexcess Enthalpy of Adsorption

If two isotherms that are close in temperature are used, approximate values for Δh are obtained by setting the derivative to a discrete slope

$$\Delta h = k_B \frac{\ln(p_2) - \ln(p_1)}{(1/T_2) - (1/T_1)} \tag{3.21}$$

$$\Delta h = k_B \frac{T_2 T_1}{T_1 - T_2} \ln \frac{p_2}{p_1} \tag{3.22}$$

which is the Clausius Clapeyron equation. Pressures and temperatures are taken at a given uptake n, for isosteric heat of adsorption, this is n_a however for isoexcess this is n_e. At low coverage (dilute gas limit) it is relatively safe to assume $n_a \approx n_e$. This assumption begins to fail when the excess uptake starts to reach a maximum, indicating that the gas phase is non-negligible.
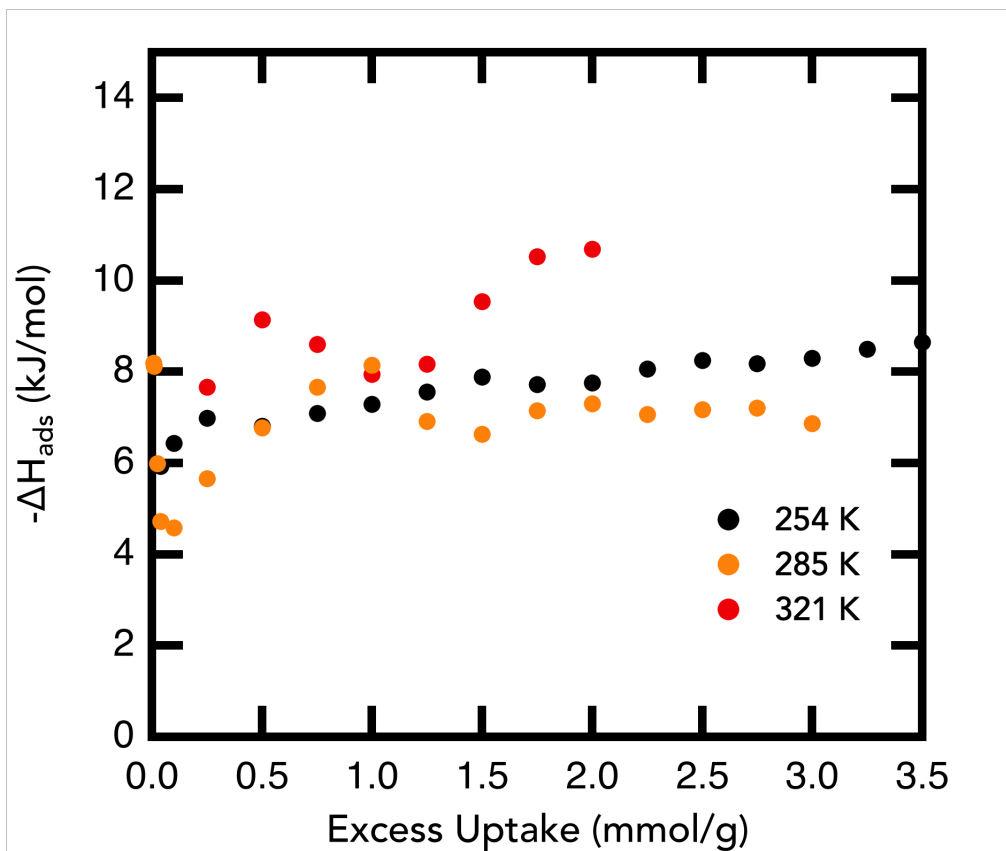
Figure 3.20: Isoexcess heats of adsorption on MSC-30 High Cu, calculated using Eq. 3.22 from Sieverts isotherm measurements at 236 K, 273 K, 298 K, and 343 K. Values calculated using adjacent temperature isotherms, with the listed temperature being the average of the two temperatures used in the calculation.

References

[1] Richard Chahine and Tapan K. Bose. Characterization and optimization of adsorbents for hydrogen storage. *Hydrogen Energy Progress*, 2:1259–1264, 1996.

[2] Suresh K. Bhatia and Alan L. Myers. Optimum conditions for adsorptive storage. *Langmuir*, 22(4):1688–1700, 2006. ISSN 07437463. doi: 10.1021/la0523816. URL `https://pubs.acs.org/doi/abs/10.1021/la0523816`.

[3] Nicholas P. Stadie, John J. Vajo, Robert W. Cumberland, Andrew A. Wilson, Channing C. Ahn, and Brent Fultz. Zeolite-templated carbon materials for high-pressure hydrogen storage. *Langmuir*, 28(26):10057–10063, 7 2012. ISSN 07437463. doi: 10.1021/la302050m. URL `http://pubs.acs.org/doi/10.1021/la302050m`.

[4] Seung Jae Yang, Ji Hyuk Im, Hirotomo Nishihara, Haesol Jung, Kunsil Lee, Takashi Kyotani, and Chong Rae Park. General relationship between hydrogen adsorption capacities at 77 and 298 K and pore characteristics of the porous adsorbents. *Journal of Physical Chemistry C*, 116(19):10529–10540, 5 2012. ISSN 19327447. doi: 10.1021/jp302304w. URL `https://pubs.acs.org/doi/abs/10.1021/jp302304w`.

[5] Wei Zhou, Hui Wu, and Taner Yildirim. Enhanced H2 adsorption in isostructural metal-organic frameworks with open metal sites: Strong dependence of the binding strength on metal ions. *Journal of the American Chemical Society*, 130(46):15268–15269, 11 2008. ISSN 00027863. doi: 10.1021/ja807023q. URL `https://pubs.acs.org/doi/abs/10.1021/ja807023q`.

[6] Yun Liu, Houria Kabbour, Craig M. Brown, Dan A. Neumann, and Channing C. Ahn. Increasing the density of adsorbed hydrogen with coordinatively unsaturated metal centers in metal-organic frameworks. *Langmuir*, 24(9):4772–4777, 5 2008. ISSN 07437463. doi: 10.1021/la703864a.

[7] R. Robson. Design and its limitations in the construction of bi- and polynuclear coordination complexes and coordination polymers (aka MOFs): A personal view. *Journal of the Chemical Society. Dalton Transactions*, 0(38):5113–5131, 7 2008. ISSN 14779226. doi: 10.1039/b805617j.

[8] Brandon R. Barnett, Hayden A. Evans, Gregory M. Su, Henry Z.H. Jiang, Romit Chakraborty, Didier Banyeretse, Tyler J. Hartman, Madison B. Martinez, Benjamin A. Trump, Jacob D. Tarver, Matthew N. Dods, Lena M. Funke, Jonas Börgel, Jeffrey A. Reimer, Walter S. Drisdell, Katherine E. Hurst, Thomas Gennett, Stephen A. FitzGerald, Craig M. Brown, Martin Head-Gordon, and Jeffrey R. Long. Observation of an Intermediate to H2 Binding in a Metal-Organic Framework. *Journal of the American Chemical Society*, 143

(36):14884–14894, 2021. ISSN 15205126. doi: 10.1021/jacs.1c07223. URL
`https://doi.org/10.1021/jacs.1c07223`.

[9] Alexey Klechikov, Jinhua Sun, Guangzhi Hu, Mingbo Zheng, Thomas Wåg-berg, and Alexandr V. Talyzin. Graphene decorated with metal nanoparticles: Hydrogen sorption and related artefacts. *Microporous and Mesoporous Materials*, 250:27–34, 9 2017. ISSN 13871811. doi: 10.1016/j.micromeso.2017. 05.014.

[10] Dipendu Saha and Shuguang Deng. Hydrogen adsorption on ordered meso-porous carbons doped with Pd, Pt, Ni, and Ru. *Langmuir*, 25(21):12550–12560, 2009. ISSN 07437463. doi: 10.1021/la901749r. URL `https://pubs.acs.org/doi/10.1021/la901749r`.

[11] Zhuxian Yang, Quanli Jia, Binling Chen, Xinglong Gou, Yanqiu Zhu, and Yongde Xia. Hydrogen adsorption properties of in-situ synthesized Pt-decorated porous carbons templated from zeolite EMC-2. *International Journal of Hydrogen Energy*, 45(46):25086–25095, 9 2020. ISSN 03603199. doi: 10.1016/j.ijhydene.2020.06.290.

[12] Hye Young Koo, Ha Jin Lee, Yong Young Noh, Eui Sup Lee, Yong Hyun Kim, and Won San Choi. Gold nanoparticle-doped graphene nanosheets: Sub-nanosized gold clusters nucleate and grow at the nitrogen-induced defects on graphene surfaces. *Journal of Materials Chemistry*, 22(15):7130–7135, 4 2012. ISSN 09599428. doi: 10.1039/c2jm16195h. URL `https://pubs.rsc.org/en/content/articlehtml/2012/jm/c2jm16195h`.

[13] Nicholas P. Stadie, Justin J. Purewal, Channing C. Ahn, and Brent Fultz. Measurements of hydrogen spillover in platinum doped superactivated carbon. *Langmuir*, 26(19):15481–15485, 10 2010. ISSN 07437463. doi: 10.1021/la9046758. URL `https://pubs.acs.org/doi/full/10.1021/la9046758`.

[14] Ashish Yadav, Mohammad Faisal, Anandh Subramaniam, and Nishith Verma. Nickel nanoparticle-doped and steam-modified multiscale structure of carbon micro-nanofibers for hydrogen storage: Effects of metal, surface texture and operating conditions. *International Journal of Hydrogen Energy*, 42(9):6104–6117, 3 2017. ISSN 03603199. doi: 10.1016/j.ijhydene.2016.11.070.

[15] Ilenia Rossetti, Gianguido Ramis, Alessandro Gallo, and Alessandro Di Michele. Hydrogen storage over metal-doped activated carbon. *International Journal of Hydrogen Energy*, 40(24):7609–7616, 6 2015. ISSN 03603199. doi: 10.1016/j.ijhydene.2015.04.064.

[16] P. Pei, M. B. Whitwick, W. L. Sun, G. Quan, M. Cannon, and E. Kjeang. Enhanced hydrogen adsorption on graphene by manganese and manganese vanadium alloy decoration. *Nanoscale*, 9(12):4143–4153, 3 2017. ISSN

20403372. doi: 10.1039/c6nr09545c. URL `https://pubs.rsc.org/en/content/articlehtml/2017/nr/c6nr09545c`.

[17] Justin J. Purewal, Houria Kabbour, John J. Vajo, Channing C. Ahn, and Brent Fultz. Pore size distribution and supercritical hydrogen adsorption in activated carbon fibers. *Nanotechnology*, 20(20):6, 2009. ISSN 09574484. doi: 10.1088/0957-4484/20/20/204012.

[18] Eric W. Lemmon, Marcia L. Huber, and Mark O. McLinden. NIST Standard Reference Database 23: Reference Fluid Thermodynamic and Transport Properties-REFPROP, Version 8.0. Technical report, 2007.

[19] Barbara Panella, Michael Hirscher, and Bernd Ludescher. Low-temperature thermal-desorption mass spectroscopy applied to investigate the hydrogen adsorption on porous materials. *Microporous and Mesoporous Materials*, 103(1-3):230–234, 6 2007. ISSN 13871811. doi: 10.1016/j.micromeso.2007.02.001.

[20] Tetsuya Shishido and Hideshi Hattori. Spillover of hydrogen over zirconium oxide promoted by sulfate ion and platinum. *Applied Catalysis A: General*, 146 (1):157–164, 10 1996. ISSN 0926860X. doi: 10.1016/0926-860X(96)00161-5.

[21] V. J. Mimeault and Robert S Hansen. Flash desorption and isotopic mixing of hydrogen and deuterium adsorbed on tungsten, iridium, and rhodium. *The Journal of Chemical Physics*, 45(6):2240–2250, 1966. ISSN 00219606. doi: 10.1063/1.1727917. URL `https://doi.org/10.1063/1.1727917`.

[22] Tersoo Genger, Olaf Hinrichsen, and Martin M. Muhler. The temperature-programmed desorption of hydrogen from copper surfaces. *Catalysis Letters*, 59:137–141, 1999. ISSN 1011372X. doi: 10.1023/A:1019076722708. URL `https://link.springer.com/content/pdf/10.1023/A:1019076722708.pdf`.

[23] Andrew Zangwill. *Physics at Surfaces*. Cambridge University Press, 3 1988. ISBN 9780521321471. doi: 10.1017/cbo9780511622564. URL `https://www.cambridge.org/core/product/identifier/9780511622564/type/book`.

[24] Peter B. Lloyd, John W. Kress, and Bruce J. Tatarchuk. Surface and bulk interactions of hydrogen with copper. *Applied Surface Science*, 119(3-4):275–287, 1997. ISSN 01694332. doi: 10.1016/S0169-4332(97)00179-7.

[25] A. V. Anil Kumar, Hervé Jobic, and Suresh K. Bhatia. Quantum effects on adsorption and diffusion of hydrogen and deuterium in microporous materials. *The Journal of Physical Chemistry B*, 110(33):16666–16671, 2006. ISSN 1520-6106. doi: 10.1021/jp063034n. URL `http://pubs.acs.org/doi/abs/10.1021/jp063034n`.

[26] Xuebo Zhao, Silvia Villar-Rodil, Ashleigh J. Fletcher, and K. Mark Thomas. Kinetic isotope effect for H2 and D2 quantum molecular sieving in adsorption/desorption on porous carbon materials. *The Journal of Physical Chemistry B*, 110(20):9947–9955, 2006. ISSN 1520-6106. doi: 10.1021/jp060748p. URL `http://pubs.acs.org/doi/abs/10.1021/jp060748p`.

[27] Iwao Yasumori, Naohiro Momma, and Makoto Kiyomiya. Mechanism of hydrogen adsorption and hydrogen- deuterium equilibration on copper surface. *Japanese Journal of Applied Physics*, 13(S2):485–488, 1974. ISSN 13474065. doi: 10.7567/JJAPS.2S2.485.

[28] Wade A. Braunecker, Sarah Shulda, Madison B. Martinez, Katherine E. Hurst, Joshua T. Koubek, Sarah Zaccarine, Rachel E. Mow, Svitlana Pylypenko, Alan Sellinger, Thomas Gennett, and Justin C. Johnson. Thermal activation of a copper-loaded covalent organic framework for near-ambient temperature hydrogen storage and delivery. *ACS Materials Letters*, 2(3):227–232, 2020. ISSN 26394979. doi: 10.1021/acsmaterialslett.9b00413. URL `https://pubs.acs.org/doi/10.1021/acsmaterialslett.9b00413`.

[29] David A. Cadenhead and Norman J. Wagner. Low-temperature hydrogen adsorption on copper-nickel alloys. *Journal of Physical Chemistry*, 72(8): 2775–2781, 5 1968. ISSN 00223654. doi: 10.1021/j100854a015. URL `https://pubs.acs.org/doi/10.1021/j100854a015`.

[30] Jitendra Bahadur, Cristian I. Contescu, Anibal J. Ramirez-Cuesta, Eugene Mamontov, Nidia C. Gallego, Yongqiang Cheng, Luke L. Daemen, and Yuri B. Melnichenko. Properties of immobile hydrogen confined in microporous carbon. *Carbon*, 117:383–392, 6 2017. ISSN 00086223. doi: 10.1016/j.carbon.2017.03.007.

[31] L. Mattera, F. Rosatelli, C. Salvo, F. Tommasini, U. Valbusa, and G. Vidali. Selective adsorption of 1H2 and 2H2 on the (0001) graphite surface. *Surface Science*, 93(2-3):515–525, 3 1980. ISSN 00396028. doi: 10.1016/0039-6028(80)90279-4.

[32] Geunseop Lee and E. W. Plummer. High-resolution electron energy loss spectroscopy study on chemisorption of hydrogen on Cu(111). *Surface Science*, 498(3):229–236, 2 2002. ISSN 00396028. doi: 10.1016/S0039-6028(01)01765-4. URL `https://www.sciencedirect.com/science/article/pii/S0039602801017654`.

[33] Josiah Willard Gibbs. On the equilibrium of heterogeneous substances. *American Journal of Science and Arts*, s3-16:441–458, 1878.

[34] S. J. Gregg and Kenneth S. W. Sing. *Adsorption, Surface Area and Porosity*. Academic Press, London, 2nd edition, 1982. doi: https://doi.org/10.1002/bbpc.19820861019. URL `https://onlinelibrary.wiley.com/doi/abs/10.1002/bbpc.19820861019`.

Chapter 4

COMPACT METHANE STORAGE AND UNUSUAL STRUCTURAL PROPERTIES OF ORDERED MICROPOROUS CARBON MONOLITHS

"Efficiency is doing better what is already being done."

— Peter Drucker

This chapter has been adapted from:

4.1   Abstract

Here we report the preparation of a series of densified carbonaceous monoliths that exhibit a record deliverable volumetric methane storage of up to $200\,\text{V/V}$ at $298\,\text{K}$ between 5-100 bar. Zeolite-templating produces a three-dimensionally connected, atomistically-thin carbon structure with ordered microporosity centered at $1.2\,\text{nm}$. The anomalously low bulk modulus inherent to these particles permits wide tunability of their pore structure upon compaction; hot-pressing in the presence of size-matched reduced graphene oxide (rGO) results in high mechanical strength of the resulting monoliths. Isosteric analysis shows increasing binding strengths to-

ward methane with increased pelletization pressure, concomitant with a narrowing pore structure, allowing optimization of optimal pore size for methane delivery. The optimized carbon monolith for volumetric methane storage surpasses all existing monolithic adsorbents, including metal-organic frameworks (MOFs), under conditions of high interest for mobile applications, emphasizing the importance of microstructure and mechanical properties over chemical composition for adsorptive energy storage and delivery.

4.2 Introduction

Increasing demands for energy and urgent calls to reduce carbon dioxide emissions carbon dioxide emissions motivate the search for sustainable replacements to conventional hydrocarbon fuels. Natural gas is in a unique position as a near-term replacement for gasoline and diesel for mobile applications, given the existing infrastructure and the ease of conversion of existing vehicles compared to hydrogen. The principal component of natural gas, methane, can be synthesized from carbon dioxide by biological or artificial photochemistry, making it a viable near-term sustainable energy vector.[1, 2] However, the low volumetric energy densities of gas-phase compared to liquid hydrocarbons impairs the widespread use of natural gas in the transportation sector. Conventional compressed natural gas (CNG) vehicles have significantly less driving range than their gasoline counterparts and require high-pressure storage cylinders (e.g., 250 bar) that present possible safety risks and require space-inefficient geometries (e.g., sphere-shaped vessels). Liquefied natural gas (LNG) exhibits improved volumetric storage density, yet has high production and

storage costs due to the energy intensive requirement of low-temperature handling at 111 K.[3] Ultimately, since gravimetric energy density decreases with increasing chain length among the simple alkane hydrocarbon fuels, the efforts to reduce carbon dioxide emissions require novel strategies to densify methane.

The phenomenon of adsorption can be harnessed to achieve fluid densification intermediate between compression and liquefaction. However, the necessary adsorbent material carries added weight and itself takes up volume ("dead volume" in the storage vessel). Nevertheless, an effectively designed adsorbent material can increase the overall storage density of gases in conventional pressure vessels. For methane, this enhancement can be significant at ambient temperature, making adsorbed natural gas (ANG) a viable solution for energy storage on-board reduced-emission mobile vehicles.[4] Adsorbents with molecular-sized pores including zeolites, activated carbons, and metal-organic frameworks (MOFs) generally show an increase of gravimetric storage capacity as a function of specific surface area, motivating efforts to design and synthesize materials with high surface areas.[5, 6] However, it is also imperative to consider the volumetric surface area, pore size, and packing density of candidate adsorbents to realize optimal volumetric energy density. While extensive work has been conducted to identify suitable adsorbents for hydrogen (where MOF-5 is prominent for hydrogen delivery),[7] methane storage has not received a similar level of attention. Studies of methane storage in engineered, molecularly-porous crystals have almost always relied on assuming single-crystal density to convert measured (gravimetric) uptake into volumetric uptake.[8] These

efforts have elevated several MOFs to prominance as candidates for optimal volumetric methane storage with adsorption: HKUST-1, NU-125, Ni-MOF-74 and UiO-66.[9, 7, 10, 11] Recently, MOF MFU-4l-Li has also been reported to exhibit very high volumetric delivery, reaching 251 and 220 V/V at 270 K and 296 K, respectively, if ideal crystal packing is assumed.[12] However, far fewer studies report the true volumetric storage of a bulk monolith or single crystal, requiring the extra step of preparing a high-quality, free-standing monolithic sample.

Typically, the actual volumetric storage capacity of monoliths is ∼ 50 % that of an ideal single crystal, even in optimal packing conditions.[13] Interestingly, Fairen-Jimenez and coworkers recently reported the preparation of an HKUST-1 monolith with extremely high bulk density (remarkably exceeding that of a single crystal) and a resulting methane delivery of 172 V/V between 5-65 bar at 298 K.[9] While the storage and delivery of pure methane in this MOF is admirable, it is important to note that HKUST-1 is notoriously sensitive to decomposition in the presence of water, a common impurity in natural gas.[14–17] It has been previously noted that for cost and durability, carbonaceous adsorbents may be a leading candidate for natural gas adsorbents ahead of MOFs,[18] but no study has reported a robust carbonaceous monolith that can approach the high methane deliveries of HKUST-1 or other metal-containing monoliths. Our hypothesis is that the metal centers and the requisite coordination bonding inherent to MOFs are not necessary to achieve the high structural regularity needed to achieve higher methane storage density, and may even inhibit this objective.

In this work, we explore a metal-free carbon scaffold material with ordered pores, known as zeolite-templated carbon (ZTC).[19] Its atomistically-modelable structure[20, 21] allows for a direct comparison to MOFs. We set out to maximize the density of ordered pores optimized for methane adsorption, within robust monolithic pellets, and based exclusively on covalently-bonded polyaromatic hydrocarbon networks. Theoretical and empirical studies show that for carbonaceous adsorbents, the optimal carbon-to-carbon spacing is 11-13 Å (effective pore width of 8-10 Å).[22–24] Most porous carbon adsorbents do not exhibit an organized structure and cannot be designed with a homogeneous pore size. Recently, however, there has been a surge in the discovery of ordered porous carbon structures. One such material, ZTC, exhibits a narrow pore size distribution centered at 1.2 nm derived from the pore-to-pore distance of 1.4 nm inherent to the zeolite template (see Figure 4.1). ZTC can consist of only atomistically thin walls; it has been shown to have unusually soft mechanical properties under external forces, providing an ideal material for dense compaction and a unique system for exploring the thermodynamics of adsorption with structural changes.[21]The maximum total volumetric uptake is limited by the physical packing of the adsorbent bed; the "ideal" volumetric adsorbent uptake is determined by measuring the powder adsorbent gravimetric uptake and treating the adsorbent volume under optimal packing conditions (i.e., as a single crystal for MOFs, or periodic unit cells for ZTCs).[19, 25]
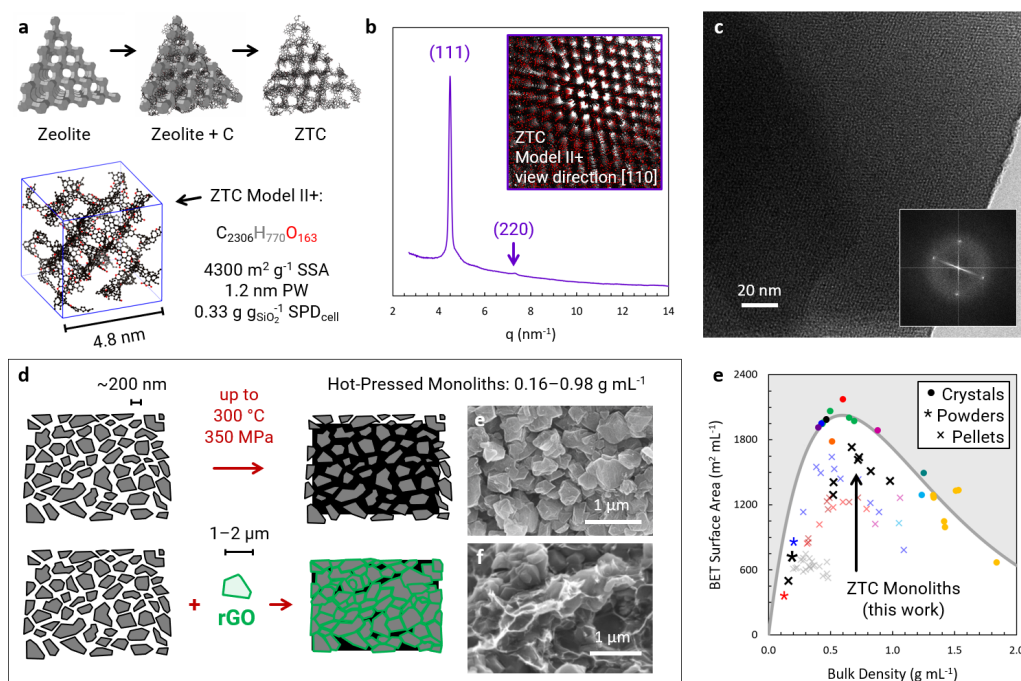
Figure 4.1: Overview of Zeolite-templated carbons. **a**, Zeolite templating synthesis strategy and periodic, atomistic model (Model II+[21]) of ZTC. **b**, XRD pattern and **c**, TEM micrograph (FFT inset) of ZTC. **d**, Pelletization strategy and SEM micrographs of ZTC monoliths with and without rGO as a binder.[26] **e**, Surface area as a function of increasing packing density across numerous solids, showing an approach to an apparent limit (grey line).[27]

Table 4.1: Pellet Pelletization Conditions and Microstructural properties

Name	Temp °C	Press MPa	SA_{BET} (m²/g)	ρ_{bulk} (g/mL)	ρ_{skel} (g/mL)	V_{pore} (mL/g)	SA_{vol} (m²/mL)
ZTC	-	-	3810	0.14	1.73	1.66	533
ZTC P1	160	50	2680	0.53	1.65	1.43	1420
ZTC P2	160	145	2580	0.67	1.77	1.35	1730
ZTC P3	160	345	1830	0.83	1.62	1.00	1520
ZTC P4	300	50	2490	0.52	1.78	1.31	1290
ZTC P6	300	145	2250	0.75	1.68	1.16	1690
ZTC P7	300	345	1450	0.98	1.69	0.76	1420

Densification, Synthesis, and Materials Properties.

Archetypical faujasite-type ZTC[25] was synthesized by the standard method, resulting in a low-density powder of high pore-to-pore regularity and aligned pores of 1.2 nm width (Figures 1a-1c). Six densified variants of ZTC were prepared for comparison to the pristine ZTC powder; their synthesis conditions and properties are summarized in Table 4.1. Densification was performed by hot-pressing in an aqueous dispersion of graphene oxide (GO). During heat treatment, the GO was converted to *in situ* reduced graphene oxide (rGO) as the binder (Figure 1d), intimately packing the ZTC particles without blocking pores as described elsewhere.[26] The GO precursor was selected to size-match effectively the produced binder to the ZTC particles. The uniquely soft mechanical properties of ZTC,[21] combined with the rGO binder, yielded a series of monolithic pellets with extraordinary robustness toward physical and chemical degradation (see Supporting Information). This size-matching strategy by commercially available GO as an intimate binder is likely generalizable to materials beyond ZTC. The monolithic nature of densified ZTC permitted measurements of the actual envelope volume of each pellet (i.e., the true volume displaced by a given adsorbent pellet, the true "bulk density" relevant in storage/delivery applications, as shown in Table 4.1). The volumetric surface areas of the pellets passed through a maximum upon increasing densification, indicating that an appropriate range of temperature and pressure were selected to achieve materials with maximum methane storage and delivery within this paradigm.

Optimal Volumetric Methane Uptake and Delivery

The as-measured gravimetric uptake of pristine ZTC powder and ZTC P6, an optimized methane delivery material, are shown in Figure 4.2a and 4.2b, respectively, demonstrating significantly higher gravimetric uptake at 100 bar than HKUST-1.[28] A double-site Langmuir model fit is shown in solid lines (see methods). Carbon adsorbents generally have higher gravimetric methane uptake than MOFs, but their lower densities negate the gravimetric advantages for volumetric uptake. To meet the specific demands of the transportation sector, an emerging metric for adsorbent materials is the *volumetric* storage density, or the amount of gas stored per storage system volume. A common metric is V/V, which refers to the total amount stored as a volume at standard temperature and pressure (STP). The details of the adsorbed storage and delivery used in this work are defined in detail in the Supporting Information and Chapter 2.

The volumetric methane uptake of powder ZTC, assuming both ideal ZTC structure density (open dotted) and actual powder density (solid), is shown in Figure 4.2c. The large discrepancy in volumetric methane uptake highlights the importance of densifying ZTC powder to realize its ultimate volumetric methane storage and delivery. The 298 K total volumetric data is shown for all densified ZTCs in Figure 4.2d (with other temperatures shown in the Supporting Information). Interestingly, the volumetric uptake of ZTC P6 at 100 bar 298 K (as shown in Figures. 4.2e,f) surpasses that of the ideal ZTC structure and that of any other carbon adsorbent to the authors' knowledge.
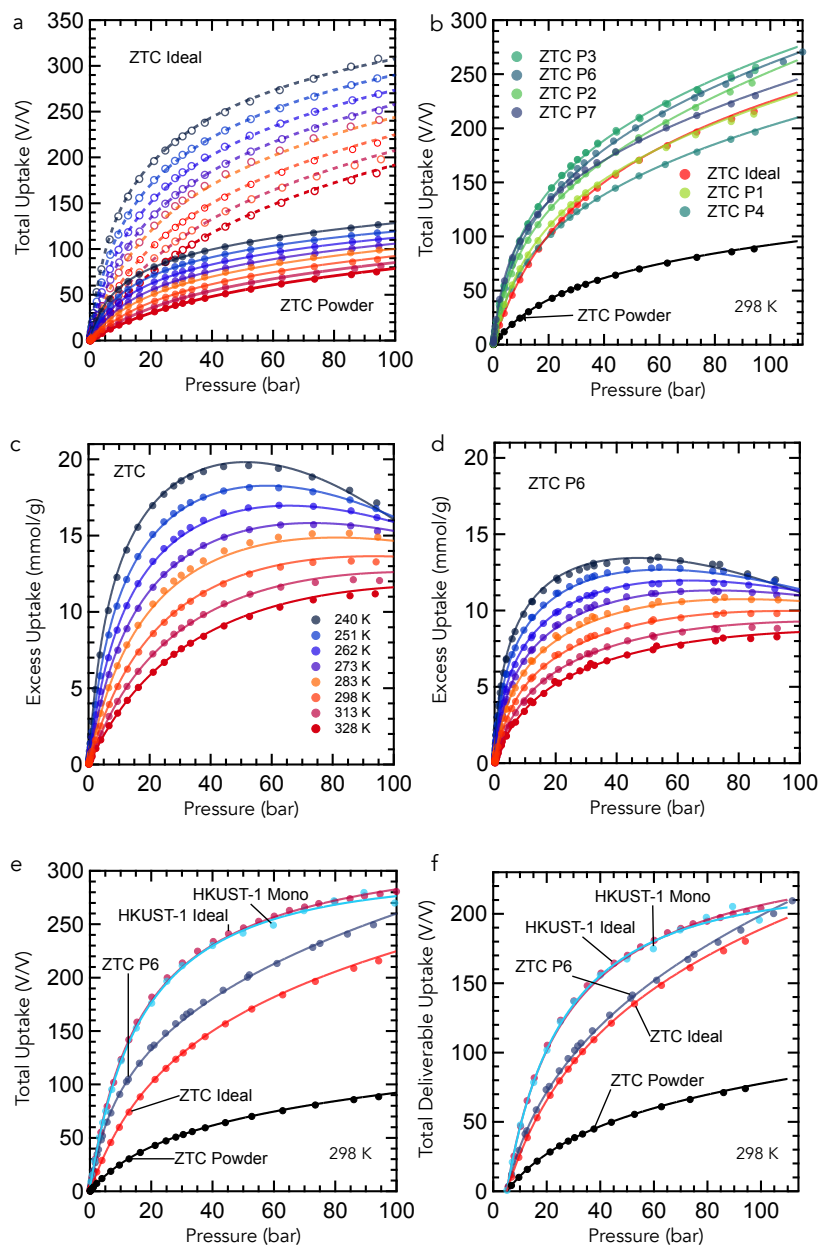
Figure 4.2: Gravimetric and volumetric uptake of ZTC materials. Excess methane adsorption (solid circles) on **a**, ZTC powder and **b**, ZTC P6 fitted with a double-site Langmuir model (solid lines). Fitting parameters provided in Table S2. **c**, Total volumetric methane adsorption on ZTC powder with powder packing density (solid circles, dotted lines) and ideal structure packing (open circles, dashed lines). **d**, Total volumetric methane uptake on ZTC monoliths. **e**, Total volumetric uptake and **f**, deliverable volumetric uptake at 298 K of notable materials (HKUST-1 ideal crystal,[28] HKUST-1 monolith,[9] and ZTC). The deliverable methane was calculated by subtracting the total volumetric uptake for each isotherm at 5 bar.

The *deliverable* volumetric uptake of methane at a pressure, P, is defined by subtracting the total volumetric uptake at 5 bar (the minimum pressure of delivery)[29] from the total uptake at P. Hence, any amount stored at 5 bar is considered "undeliverable" and should be minimized. While MOFs such as HKUST-1 have been reported that have high total volumetric methane uptakes, these materials have significantly reduced deliverable quantities due to the strong binding of methane at low pressures. The total and deliverable volumetric methane uptake of ZTC P6, in addition to other notable adsorbents, are shown in Figures 4.2e and 4.2f, respectively. ZTC P6 meets previous ambient temperature delivery records set by monolithic MOFs at 100 bar; importantly, no metal coordination centres are needed and the materials remain robust to humidity and oxidation compared to MOFs.[9] Furthermore, at 273 K ZTC P6 shows enhanced deliverable methane densities over previously reported materials at pressures > 65 bar. Measurements at > 100 bar reveal the advantage of ZTC P6 over HKUST-1 monoliths as delivery continues to increase. At 100 bar, densified ZTC would provide ultra-high deliverable energy densities of ~7 MJ L^{-1} (see Figure 4.3f).

Pelletization Effects on Microstructure

It is intriguing that ZTC P6 exhibits a higher volumetric storage than even the ideal ZTC structure. For an ideal rigid framework material, total volumetric methane uptake would be directly proportional to the packing density as the framework is more efficiently organized to eliminate interparticle voids, approaching (but not exceeding) the value of the ideal structure uptake. Exceeding the ideal structure
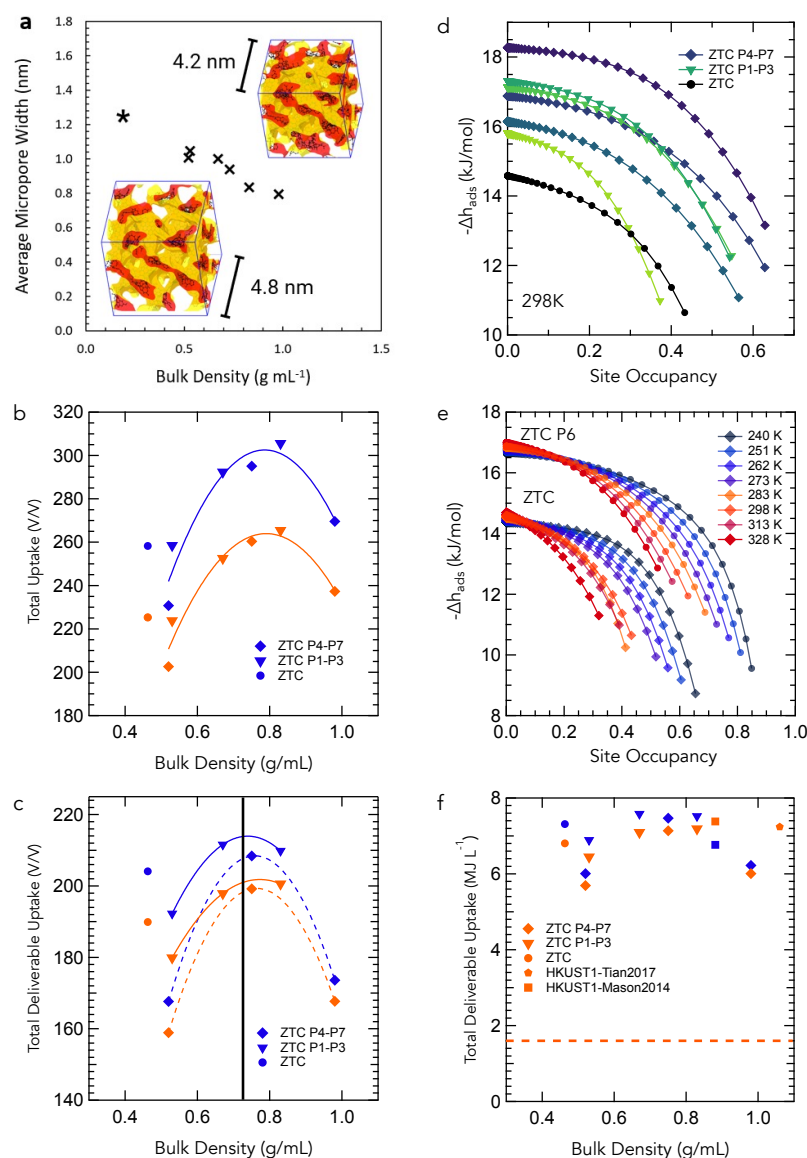
Figure 4.3: Average micropore width in ZTC pellets as a function of bulk density **a**, with inset of structural compaction. Total volumetric uptake **b**, and total deliverable volumetric uptake **c**, of ZTC materials as a function of bulk density at 298 K (orange) and 273 K (blue). Isosteric enthalpies of adsorption of all ZTC monoliths at 298 K **d**, and ZTC P6 (diamonds) **e**, compared to ZTC powder (circles) as a function of the fraction of sites occupied. Pelletization pressure and pellet number increases with trace darkness; green traces with triangles denote pellets synthesized at 433 K and blue traces with diamonds at 573 K. Total deliverable volumetric uptake of notable materials **f**, compared with volumetric energy density of state-of-the-art lithium batteries (horizontal red line).[30] Measurement conditions for total deliverable uptake at 100 bar, 273 K and 298 K, where diamonds denote ZTC powder with ideal ZTC density, triangles denote ZTC pellets, squares denote HKUST-1 powder data with crystal density,[28] and hash symbols denote HKUST-1 monoliths.[9]

limit indicates that microstructural differences may exist between the original ZTC powder and the densified variant, ZTC P6. Further possibilities, such as expansion/contraction of the lattice under methane loading are also explored in the next section.

Several features of the series of densified ZTC monoliths indicate distinct, tunable changes to the atomistic structure of the ZTC particles as a function of pelletization conditions during hot-pressing. Pore-size analysis of the series (Figure 4.3a) shows the continuous narrowing of pore width upon increasing severity of hot-pressing conditions. Total and deliverable volumetric uptake of the monoliths as a function of bulk density is shown in Figure 4.3b and 4.3c, respectively. Synthesized ZTC monoliths in this work (triangles) show maximum deliverable methane storage (at 100 bar) with 0.75 g/mL bulk density. This bulk density corresponds to the "ideal" volumetric ambient temperature methane monolayer packing scheme for a theoretical 2D-carbon slit pore (solid line at 0.73 g/mL, as described in Bhatia and Myers), where single layers of graphene (SSA 2630 m^2/g) are separated by 10.45 Å to accommodate exactly two layers of adsorbed methane.[31, 32] Bulk densities for carbon materials below this value have excess void volume not needed for adsorbed methane storage, and above this value correspond to pores that can only accommodate one methane layer. ZTC P6 has the bulk density closest to this "optimal" value.

The non-destructive modification of pore structure with pressure is a unique property of a material with a flexible structure, despite having covalent bonds. The

compliance of the ZTC structure is due to its underlying framework of atomically-thin curved graphene-like surfaces. Most high surface area carbons have rigid frameworks which inhibit the modification of pores while the inherent bonding in MOFs result in structure collapse with applied pressure. ZTCs have been shown to have remarkable elasticity and softness, allowing for temporary modification of a fully recoverable pore structure under applied pressure.[19] The pelletization pyrolysis inhibits the relaxation of the ZTC structure with removal of applied force, allowing for persistent pore size tunability with pelletization.

We have shown that increasing adsorption enthalpies can be achieved through pressurization, allowing for fine tuning of microporous structures for optimizing deliverable volumetric gas density for certain pressure and temperature conditions. The change in microstructure by pressurization is secured with the rGO binder, which prevents the relaxation of the ZTC framework to its original structure. Smaller pores have higher adsorption enthalpies due to increased overlapping of adsorption potentials from both pore walls. We observe a 20% increase in the enthalpies at all temperatures for ZTC P6 over the uncompressed ZTC powder (Figure 4.3d). This behaviour is observed for all of the ZTC monoliths in that the Henry's Law value at 298 K increases with increasing pelletization pressure (see Figure 4.3e). The enthalpy increase due to the change in pore size is consistent with reported pore size-dependent methane isosteric heat computations.[32]

4.3   Conclusion

A simple route to monolith preparation under mild temperature and pressure conditions in the presence of rGO as a binder has been shown, which has broad implications for the tunability of adsorbent materials for gas storage applications. Zeolite-templated carbon (ZTC) monoliths have shown record total and total deliverable volumetric uptakes between 5-100 bar of 260 V/V and 200 V/V, respectively, for ZTC P6. Highly effective methane storage can be achieved without the presence of metal-based coordination nodes, as the isosteric methane heats of adsorption in carbonaceous adsorbents are suitable for ambient temperature gas storage applications. Synthesized ZTC materials have exceptional porosity, uniquely soft mechanical properties (especially a low elastic modulus of <1 GPa, an order of magnitude lower than MOFs), and a controlled pore size that can be tuned for optimal methane delivery. A maximum in deliverable volumetric uptake was observed for a pellet bulk density of around 0.7 $g\,mL^{-1}$, which corresponds to the density of a slit pore that can accomodate two layers of adsorbed methane.

4.4   Methods

Synthesis of ZTC Samples

An impregnation/chemical vapor deposition (CVD) approach was used to synthesize the zeolite-templated carbon (ZTC) powder. All tube furnace steps were conducted at 200 sccm gas flow with a ramp rate of 5 °C min^{-1} unless otherwise noted. NaY zeolite (4g Tosoh HSZ 320NAA) was dried under vacuum in a B-585 Buchi at 300 °C for 1 day. Furfuryl alcohol (40 mL Sigma, 99%) was impregnated

into the zeolite structure by stirring for 1 day, dried with vacuum suction, and poly-merized at 80°C in a 45mm OD quartz tube furnace (2 alumina boats, 10x30x107 mm) for 1 day under argon flow. The zeolite/polymer sample was pyrolyzed by heating to 700°C, under 7% propylene in argon (99.999% Ar purity) mixture to further the carbon deposition in the zeolite structure by CVD for 5 hours. The gas was then switched to argon flow and heated to 900°C and held for 3 hours, then cooled overnight. The zeolite structure was removed using 3 35 mL hydrofluroic acid (48-51%, Thermo Scientific) washes, centrifuged, followed by three DI washes. The resulting zeolite-templated carbon was dried at 40 °C in ambient conditions.

The pelletization procedure is described in Gabe et al., and is outlined here for completeness.[26] ZTC powder was combined with an aqueous solution of graphene oxide (GO, NiSiNa materials Co. Ltd., 10 mg mL^{-1}) to obtain 5 wt% GO in ZTC mixture. Distilled water was added and the solution was stirred, then further mixed in a planetary mixer at a speed of 2000 rpm for 10 minutes. The water was removed by evaporation at 60 °C and ground into a powder. 100 mL of the resulting powder was inserted into a hot-press mold, evacuated, and ramped to the temperature and pressure listed in Table 4.1 and held for 1 hour, then returned to ambient conditions.

Microstructural Characterization of ZTC Materials

In situ X-ray diffraction (XRD) measurements were performed at the Stanford Synchrotron Radiation Lightsource (SSRL) at beamline 2-1. The incident wave-length was 0.73 Å, as determined from a NIST 660c LaB6 calibration measurement. Samples were loaded into 1.5 mm outer diameter single crystal sapphire capillar-

ies with 0.25 mm wall thickness and sealed in a sample cell (described in detail elsewhere[33]) with graphite ferrules. A type K thermocouple, used to monitor sample temperature, was inserted into the capillary and made direct contact with the packed powder. Sample temperature was controlled using an open-flow cryogenic gas cooler (Cryostream, Oxford Cryosystems). The sample cell was connected to a custom gas handling manifold which was used to pressurize the sample under research purity methane (99.999%) to setpoints up to 80 bar. Angular dispersive XRD data were acquired stepwise using a Pilatus 100 K hybrid photon counting detector in portrait orientation. The 2D diffraction images were integrated into 1D XRD patterns using a custom Python script.

A Micrometrics 3Flex unit was used to conduct 77 K nitrogen adsorption measurements for determination of specific surface area (SSA), pore volume, and pore size distribution. SSA was obtained using the BET method. Pore size distributions were obtained using a non-local density functional as implemented in the Micromeritics software.

Skeletal volume was determined using helium pycnometry. Bulk volume of the monoliths was determined using calipers on pristine cylindrical samples and massing each pellet, and using jolting volumetry for the ZTC powder.

Methane Adsorption Measurements and Model

Excess methane adsorption was measured on ZTC powder and on a series of densified ZTC materials according to the usual definition attributed to Gibbs,[34] between 238-328 K and 0-100 bar, the range of temperature and pressure of highest

interest for mobile ANG applications. A custom automated volumetric Sieverts apparatus was used with thermoelectrics for temperature control, and a minimum 300 second equilibration time (480 second for temperatures <-30 °C) was implemented for the adsorption and desorption steps. Samples were heated to 55 °C for several hours between runs to drive off any impurities. Overall, ∼ 200 pressure and temperature adsorption equilibria per sample were measured and simultaneously fit to a global Langmuir-type adsorption model:

$$n_e(f, P, T) = n_m(1 - \rho_g(P, T)v_m)\left((1 - \alpha)\frac{K_1 f}{1 + K_1 f} + \alpha\frac{K_2 f}{1 + K_2 f}\right) \quad (4.1)$$

where n_e, ρ_g, and v_a are the excess uptake, gas phase density, and adsorbed phase volume, respectively. All practical analysis of methane volumetrics and the delivered quantity above 5 bar were assessed using the directly measured excess adsorption quantity, n_e. Absolute adsorption was also determined in order to assess the thermodynamics of the adsorbed phase (see Chapter 2 for a statistical mechanical justification):

$$K_i(T) = \frac{A_i}{\sqrt{T}}e^{-\frac{E_i}{RT}} \quad (4.2)$$

$$\frac{A_i}{\sqrt{T}} = A_{B,i}\frac{\lambda_g}{\hbar\omega} \quad (4.3)$$

where A_i is the temperature-independent prefactor, $A_{B,i}$ is the two dimensional binding site volume, λ_g is the thermal de Broglie wavelength, $\hbar$ is Planck's constant, and ω is the vibrational adsorption frequency.

By using fugacity instead of pressure as an independent variable during fitting, corrections for the behavior of real methane could be incorporated into the adsorption model. As in previous work,[35] a single-site Langmuir model was not sufficient

for describing methane adsorption across the entire range of T and P explored in this study; hence, a double-site Langmuir equation was employed. The measured gravimetric methane adsorption equilibria on ZTC powder and corresponding Langmuir fit are shown in Figure 4.2a.

4.5 Acknowledgements

4.6 Supporting Information

Fitting of Experimental Isotherms
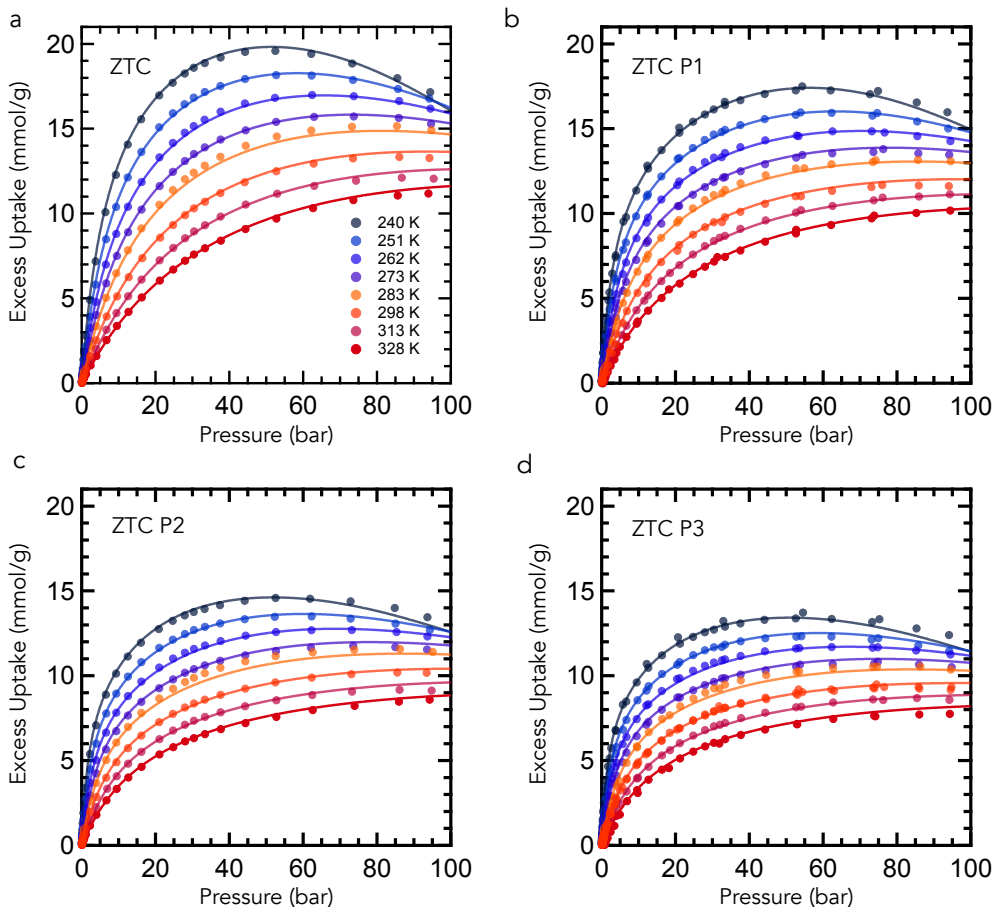
Figure 4.4: Excess methane adsorption (solid circles) on **a**, ZTC powder, pellets **b**, ZTC P1 **c**, ZTC P2, and **d**, ZTC P3 with double-site Langmuir fits (solid lines). Parameters provided in Table 4.2.

Experimentally measured Gibbs excess uptake can be converted to absolute uptake measurements using Eq. 2.26:

$$n_e = n_a - \rho_g v_a = (n_m - \rho_g v_m)\theta \tag{4.4}$$

where n_m, n_e, n_a, ρ_g, v_m and v_a are the max absolute gas uptake, excess uptake, absolute uptake, gas density, maximum adsorbed volume and adsorbed volume, respectively.
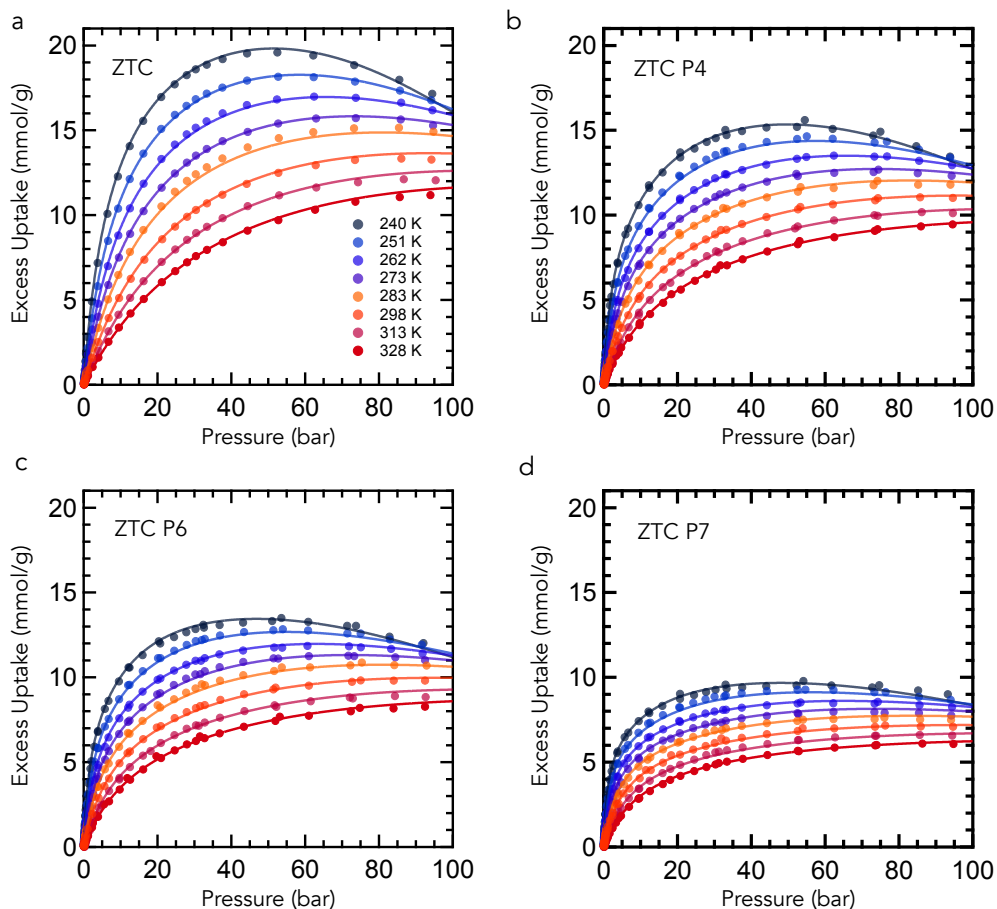
Figure 4.5: Excess methane adsorption (solid circles) on **a**, ZTC powder, pellets **b**, ZTC P4 **c**, ZTC P6, and **d**, ZTC P7 with double-site Langmuir fits (solid lines). Parameters provided in Table 4.2.

Each isotherm set corresponding to a particular adsorbent was universally fitted to a double-site Langmuir equation with seven fitting parameters (see equations 2.12, 2.24, and 4.4) :

$$n_e(P,T) = (n_m - \rho_g(P,T) * v_m)\left((1-\alpha)\frac{K_1(T)f}{1+K_1(T)f} + \alpha\frac{K_2(T)f}{1+K_2(T)f}\right). \quad (4.5)$$

The fitting equations and procedure were implemented in the Python REALIST package, which is available for use online.[36] The differential evolution package in scipy was used with the "randtobest1exp" strategy, a tolerance of 0.006, and a maximum of 10,000 iterations. The multiprocessing Python package was utilized to

Sample	n_{m}	v_m	α	A_1	$-\varepsilon_1$	A_2	$-\varepsilon_2$
	mmol/g	mL/g		$K^{0.5}MPa^{-1}$	kJ/mol	$K^{0.5}MPa^{-1}$	kJ/mol
ZTC	41.6	2.13	0.558	3.12e-2	13.20	9.96e-4	15.03
ZTC P1	41.5	1.95	0.694	3.14e-2	14.60	1.32e-3	14.14
ZTC P2	23.5	0.957	0.643	3.08e-2	15.93	2.09e-3	15.53
ZTC P3	22.0	0.929	0.628	2.96e-2	16.12	1.86e-3	15.55
ZTC P4	25.1	1.13	0.668	4.26e-2	15.02	4.43e-3	14.15
ZTC P6	19.8	0.828	0.654	4.20e-2	15.71	4.05e-3	15.15
ZTC P7	13.8	0.502	0.591	3.28e-2	17.09	1.76e-3	16.63

Table 4.2: Double-site Langmuir coefficients for ZTC powder and pellets using Eq. 4.5.

run 128 random seeds across 12 threads. Fugacity is only used for thermodynamic calculations. While both fugacity and pressure are needed for the real-gas Langmuir equation in Eq. 4.5, the resulting uptakes are plotted only against the experimentally measured pressures.
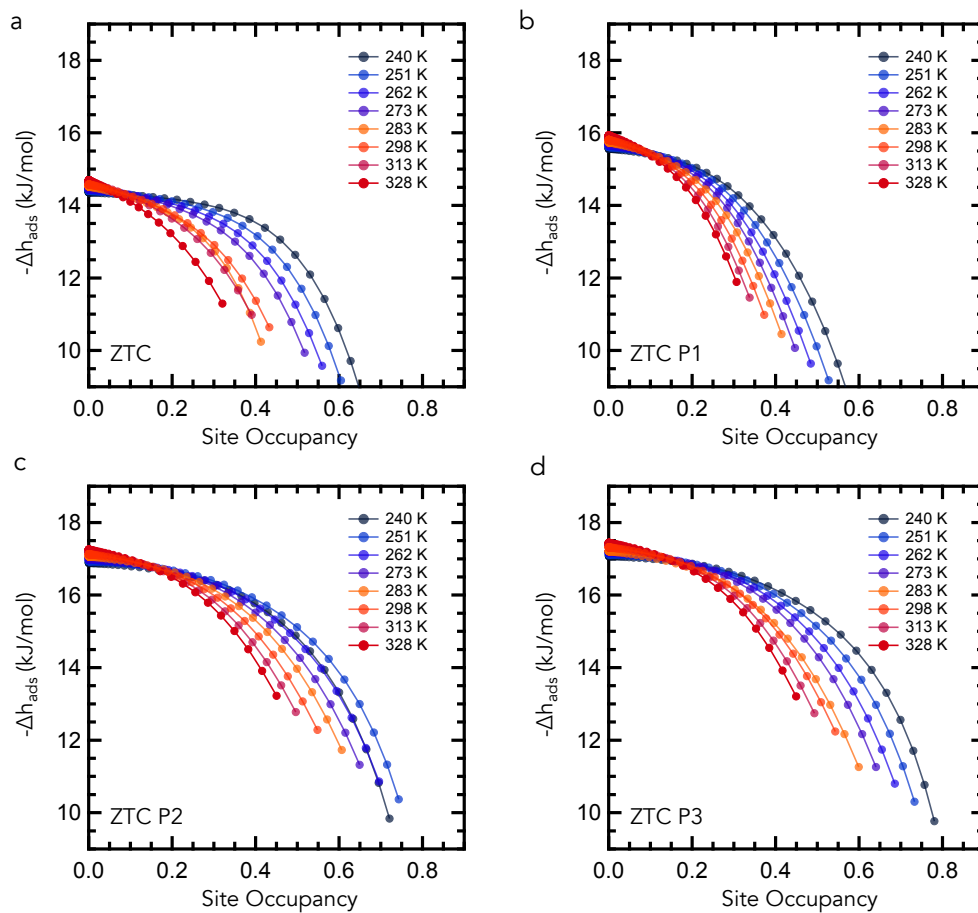
Figure 4.6: Enthalpies of adsorption as a function of site occupancy on **a**, ZTC powder, pellets **b**, ZTC P1 **c**, ZTC P2, and **d**, ZTC P3 calculated from Eq. 2.47 and Eq. 4.5 for $-\Delta h_{ads}$ and θ, respectively. Parameters provided in Table 4.2.
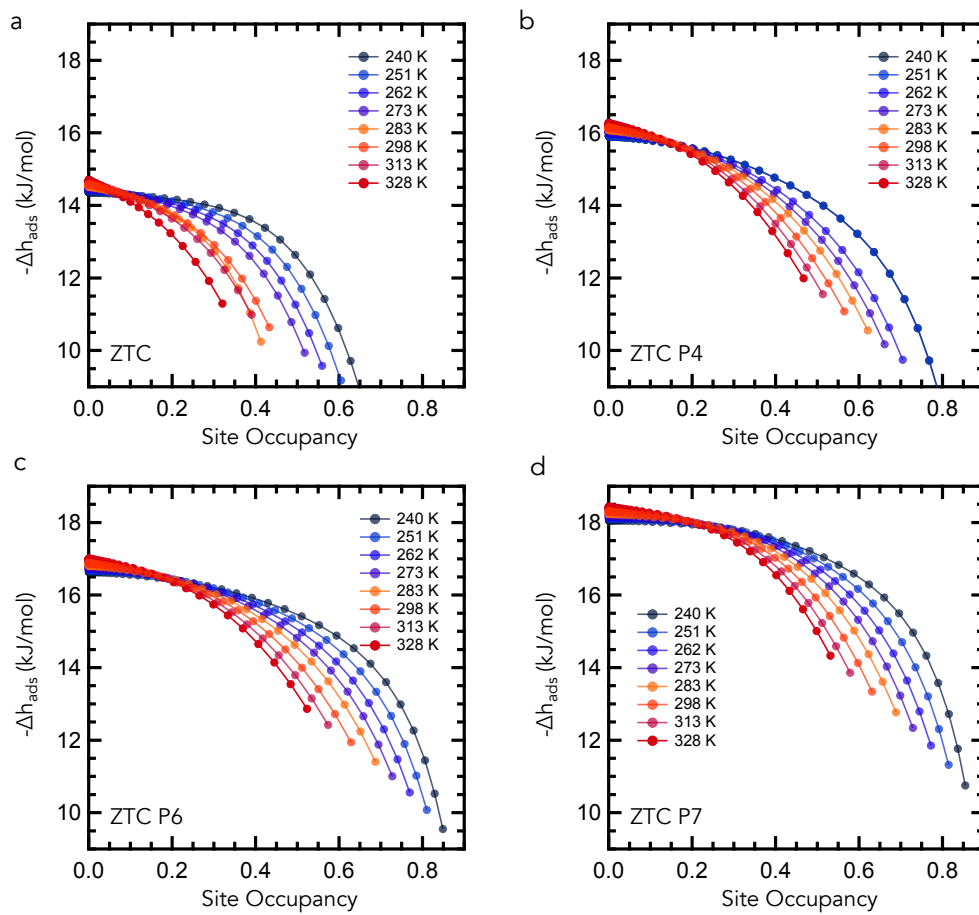
Figure 4.7: Enthalpies of adsorption as a function of site occupancy on **a**, ZTC powder, pellets **b**, ZTC P4 **c**, ZTC P6, and **d**, ZTC P7 calculated from Eq. 2.47 and Eq. 4.5 for $-\Delta h_{ads}$ and θ, respectively. Parameters provided in Table 4.2.
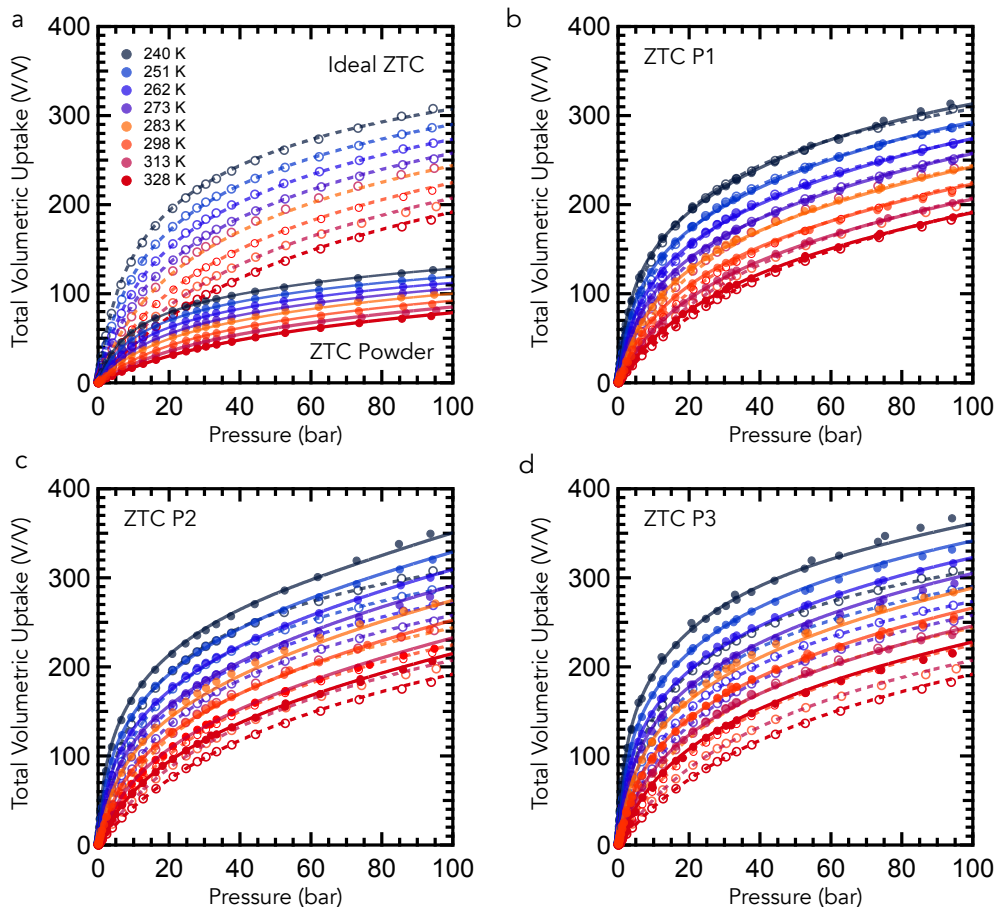
Figure 4.8: Total volumetric methane adsorption on an ideal ZTC structure packing (open circles dashed lines) and on **a**, ZTC powder with powder packing density, **b**, ZTC P1 **c**, ZTC P2, and **d**, ZTC P3 (solid circles, dotted lines) calculated from Eq. 4.8 and Eq. 2.33. Parameters provided in Table 4.1.

4.7 Volumetric Uptake

For a single crystal of microporous material, the total volume can be defined as

$$V_{pore} + V_{skeletal} = V_{bulk} \tag{4.6}$$

where V_{pore}, $V_{skeletal}$, and V_{bulk} are the micropore volume, adsorbent skeletal volume, and bulk sample volume, respectively. To convert measured gravimetric excess uptake to volumetric excess uptake the following equation is used

$$n_{e,v}(P,T) = n_e(P,T)\rho_{bulk}v_{g,STP} \tag{4.7}$$

where ρ_{bulk} is the bulk density of the adsorbent, and $v_{g,STP}$ is the molar volume of the adsorbate at STP. Volumetric uptake is unitless and is defined as V_{STP}/V, which is the amount of equivalent gas at STP adsorbed normalized by the adsorbent volume. The total volumetric uptake is the sum of excess volumetric uptake and the bulk gas phase in the adsorbent

$$n_{t,v} = n_{e,v} + (\rho_g v_{gas} X_{pore}).$$ (4.8)

It is necessary to know the void fraction of the bulk material, X_{pore}, to calculate the total volumetric uptake. Physically, this is the ratio of empty void volume to the physical volume of the sample. This is commonly defined in literature as

$$X_{pore,common} = \frac{V_{N_2}}{V_{bulk}} = \rho_{bulk} * V_{pore}.$$ (4.9)

This is accurate for an ideal pellet of a single crystal adsorbent with no macropores or surface roughness. We will be using this metric to compare with other results from literature, as this is the most prevalent one used. We also propose a more accurate metric for accounting for the void fraction as

$$X_{pore,best} = \frac{V_{bulk} - V_{skel}}{V_{bulk}} = 1 - \frac{\rho_{bulk}}{\rho_{skel}}.$$ (4.10)

Monolith Stability Experiments

ZTC P7 was subjected to both physical stability as well as water stability. The pellet was dropped from about 7 cm multiple times showing no deformation. After the pellet was dropped, DI water was added to the pellet in the petri dish. As soon as the water interacted with the pellet, the pellet started to bubble and fracture. Small shard like pieces started to break off from main pellet. After about 4 minutes in
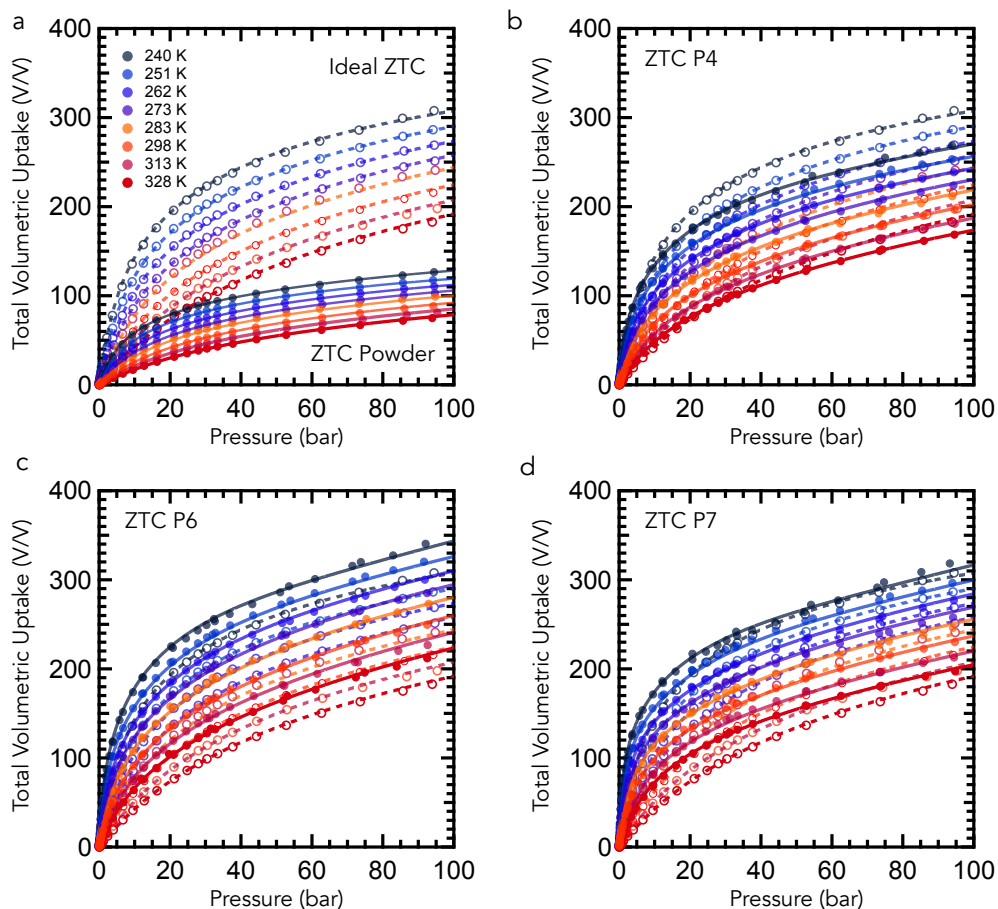
Figure 4.9: Total volumetric methane adsorption on an ideal ZTC structure packing (open circles dashed lines) and on **a**, ZTC powder with powder packing density, pellets **b**, ZTC P4 **c**, ZTC P6, and **d**, ZTC P7 (solid circles, dotted lines) calculated from Eq. 4.8 and Eq. 4.9. Parameters provided in Table 4.1

water the pellet had completely fractured into small shard like pieces. These shards were dried and then analyzed using N2 adsorption. The original ZTC P7 had a BET surface area of 1380 m^2 g^{-1} and the post water ZTC P7 shards had a BET surface area of 1293 m^2 g^{-1}. The N_2 isotherm and pore size distribution can be seen in Figure 4.10.
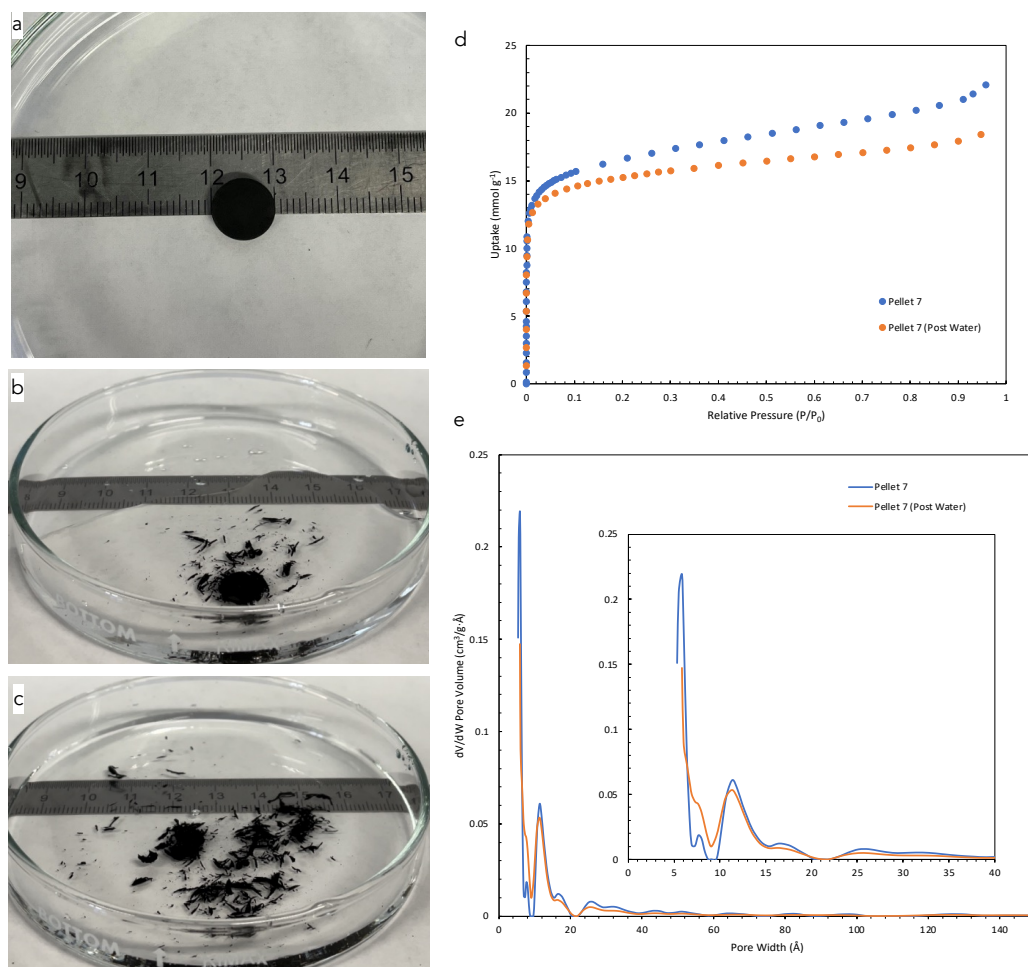
Figure 4.10: Water stability experiments on ZTC P7. Pristine ZTC P7 **a**, after immediate exposure to water **b**, and after 4 minutes of water exposure **c**. 77 K N_2 isotherm measurements on ZTC P7 pre and post water exposure **d** and resulting pore size distribution calculations **e**.

References

[1] Thomas Amon, Barbara Amon, Vitaliy Kryvoruchko, Andrea Machmüller, Katharina Hopfner-Sixt, Vitomir Bodiroza, Regina Hrbek, Jürgen Friedel, Erich Pötsch, Helmut Wagentristl, Matthias Schreiner, and Werner Zollitsch. Methane production through anaerobic digestion of various energy crops grown in sustainable crop rotations. *Bioresource Technology*, 98(17): 3204–3212, 12 2007. ISSN 09608524. doi: 10.1016/j.biortech.2006.07. 007. URL `https://www.sciencedirect.com/science/article/pii/S0960852406003117`.

[2] Heng Rao, Luciana C. Schmidt, Julien Bonin, and Marc Robert. Visible-light-driven methane formation from CO2 with a molecular iron catalyst. *Nature*, 548(7665):74–77, 8 2017. ISSN 14764687. doi: 10.1038/nature23016. URL `http://www.nature.com/articles/nature23016`.

[3] Alternative Fuels Data Center: Natural Gas Fuel Basics. *US Department of Energy*, 2013. URL `https://afdc.energy.gov/fuels/natural_gas_basics.html`.

[4] Matthew Beckner and Anne Dailly. Adsorbed methane storage for vehicular applications. *Applied Energy*, 149:69–74, 7 2015. ISSN 03062619. doi: 10.1016/j.apenergy.2015.03.123. URL `https://linkinghub.elsevier.com/retrieve/pii/S0306261915004250`.

[5] Mirian Elizabeth Casco, Manuel Martínez-Escandell, Enrique Gadea-Ramos, Katsumi Kaneko, Joaquín Silvestre-Albero, and Francisco Rodríguez-Reinoso. High-pressure methane storage in porous materials: Are carbon materials in the pole position? *Chemistry of Materials*, 27(3):959–964, 2 2015. ISSN 15205002. doi: 10.1021/cm5042524. URL `https://pubs.acs.org/doi/abs/10.1021/cm5042524`.

[6] Nicholas P. Stadie, Maxwell Murialdo, Channing C. Ahn, and Brent Fultz. Anomalous isosteric enthalpy of adsorption of methane on zeolite-templated carbon. *Journal of the American Chemical Society*, 135(3):990–993, 1 2013. ISSN 00027863. doi: 10.1021/ja311415m. URL `https://pubs.acs.org/doi/abs/10.1021/ja311415m`.

[7] Alauddin Ahmed, Saona Seth, Justin Purewal, Antek G. Wong-Foy, Mike Veenstra, Adam J. Matzger, and Donald J. Siegel. Exceptional hydrogen storage achieved by screening nearly half a million metal-organic frameworks. *Nature Communications*, 10(1), 2019. ISSN 20411723. doi: 10.1038/s41467-019-09365-w. URL `http://dx.doi.org/10.1038/s41467-019-09365-w`.

[8] Philip A. Parilla, Karl Gross, Katherine Hurst, and Thomas Gennett. Recommended volumetric capacity definitions and protocols for accurate, standardized and unambiguous metrics for hydrogen storage materials. *Applied Physics*

A: Materials Science and Processing, 122(3):1–18, 3 2016. ISSN 14320630. doi: 10.1007/s00339-016-9654-1. URL `https://link.springer.com/article/10.1007/s00339-016-9654-1`.

[9] Tian Tian, Zhixin Zeng, Diana Vulpe, Mirian E. Casco, Giorgio Divitini, Paul A. Midgley, Joaquin Silvestre-Albero, Jin Chong Tan, Peyman Z. Moghadam, and David Fairen-Jimenez. A sol-gel monolithic metal-organic framework with enhanced methane uptake. *Nature Materials*, 17(2):174–179, 2 2018. ISSN 14764660. doi: 10.1038/NMAT5050. URL `https://www.nature.com/articles/nmat5050`.

[10] Yang Peng, Vaiva Krungleviciute, Ibrahim Eryazici, Joseph T. Hupp, Omar K. Farha, and Taner Yildirim. Methane storage in metal-organic frameworks: Current records, surprise findings, and challenges. *Journal of the American Chemical Society*, 135(32):11887–11894, 8 2013. ISSN 00027863. doi: 10.1021/ja4045289. URL `https://pubs.acs.org/doi/abs/10.1021/ja4045289`.

[11] B. M. Connolly, M. Aragones-Anglada, J. Gandara-Loe, N. A. Danaf, D. C. Lamb, J. P. Mehta, D. Vulpe, S. Wuttke, J. Silvestre-Albero, P. Z. Moghadam, A. E.H. Wheatley, and D. Fairen-Jimenez. Tuning porosity in macroscopic monolithic metal-organic frameworks for exceptional natural gas storage. *Nature Communications*, 10(1):1–11, 2019. ISSN 20411723. doi: 10.1038/s41467-019-10185-1. URL `http://dx.doi.org/10.1038/s41467-019-10185-1`.

[12] Zhijie Chen, Mohammad Rasel Mian, Seung Joon Lee, Haoyuan Chen, Xuan Zhang, Kent O. Kirlikovali, Sarah Shulda, Patrick Melix, Andrew S. Rosen, Philip A. Parilla, Thomas Gennett, Randall Q. Snurr, Timur Islamoglu, Taner Yildirim, and Omar K. Farha. Fine-tuning a robust metal-organic framework toward enhanced clean energy gas storage. *Journal of the American Chemical Society*, 143(45):18838–18843, 11 2021. ISSN 15205126. doi: 10.1021/jacs.1c08749. URL `https://pubs.acs.org/doi/abs/10.1021/jacs.1c08749`.

[13] J. J. Purewal, D. Liu, J. Yang, A. Sudik, D. J. Siegel, S. Maurer, and U. Müller. Increased volumetric hydrogen uptake of MOF-5 by powder densification. *International Journal of Hydrogen Energy*, 37(3):2723–2727, 2 2012. ISSN 03603199. doi: 10.1016/j.ijhydene.2011.03.002.

[14] Katie A. Cychosz and Adam J. Matzger. Water stability of microporous coordination polymers and the adsorption of pharmaceuticals from water. *Langmuir*, 26(22):17198–17202, 11 2010. ISSN 07437463. doi: 10.1021/la103234u. URL `https://pubs.acs.org/doi/full/10.1021/la103234u`.

[15] Alternative Fuels Specifications | California Air Resources Board. URL `https://ww2.arb.ca.gov/resources/documents/alternative-fuels-specifications`.

[16] Farhana Gul-E-Noor, Bettina Jee, Andreas Pöppl, Martin Hartmann, Dieter Himsl, and Marko Bertmer. Effects of varying water adsorption on a Cu3(BTC)2 metal-organic framework (MOF) as studied by 1H and 13C solid-state NMR spectroscopy. In *Physical Chemistry Chemical Physics*, volume 13, pages 7783–7788. The Royal Society of Chemistry, 4 2011. doi: 10.1039/c0cp02848g. URL https://pubs.rsc.org/en/content/articlelanding/2011/cp/c0cp02848g.

[17] J. Raziel Álvarez, Elí Sánchez-González, Eric Pérez, Emilia Schneider-Revueltas, Ana Martínez, Adriana Tejeda-Cruz, Alejandro Islas-Jácome, Eduardo González-Zamora, and Ilich A. Ibarra. Structure stability of HKUST-1 towards water and ethanol and their effect on its CO2 capture properties. *Dalton Transactions*, 46(28):9192–9200, 7 2017. ISSN 14779234. doi: 10.1039/c7dt01845b.

[18] Mirian Elizabeth Casco, Manuel Martínez-Escandell, Enrique Gadea-Ramos, Katsumi Kaneko, Joaquín Silvestre-Albero, and Francisco Rodríguez-Reinoso. High-pressure methane storage in porous materials: Are carbon materials in the pole position? *Chemistry of Materials*, 27(3):959–964, 2 2015. ISSN 15205002. doi: 10.1021/cm5042524. URL https://pubs.acs.org/doi/abs/10.1021/cm5042524.

[19] H Nishihara and T Kyotani. Zeolite-templated carbons-three-dimensional microporous graphene frameworks. *Chemical Communications*, 54(45):5648–5673, 5 2018. ISSN 1364548X. doi: 10.1039/c8cc01932k.

[20] Hirotomo Nishihara, Hiroyuki Fujimoto, Hiroyuki Itoi, Keita Nomura, Hideki Tanaka, Minoru T. Miyahara, Patrick A. Bonnaud, Ryuji Miura, Ai Suzuki, Naoto Miyamoto, Nozomu Hatakeyama, Akira Miyamoto, Kazutaka Ikeda, Toshiya Otomo, and Takashi Kyotani. Graphene-based ordered framework with a diverse range of carbon polygons formed in zeolite nanochannels. *Carbon*, 129:854–862, 4 2018. ISSN 00086223. doi: 10.1016/j.carbon.2017.12.055.

[21] Keita Nomura, Hirotomo Nishihara, Masanori Yamamoto, Atsushi Gabe, Masashi Ito, Masanobu Uchimura, Yuta Nishina, Hideki Tanaka, Minoru T. Miyahara, and Takashi Kyotani. Force-driven reversible liquid–gas phase transition mediated by elastic nanosponges. *Nature Communications*, 10(1):1–10, 6 2019. ISSN 20411723. doi: 10.1038/s41467-019-10511-7. URL https://www.nature.com/articles/s41467-019-10511-7.

[22] Kimberly R. Matranga, Alan L. Myers, and Eduardo D. Glandt. Storage of natural gas by adsorption on activated carbon. *Chemical Engineering Science*, 47(7):1569–1579, 5 1992. ISSN 00092509. doi: 10.1016/0009-2509(92)85005-V. URL https://www.sciencedirect.com/science/article/pii/000925099285005V.

[23] David Nicholson. Simulation studies of methane transport in model graphite micropores. *Carbon*, 36(10):1511–1523, 10 1998. ISSN 00086223. doi: 10.

1016/S0008-6223(98)00143-2. URL `https://www.sciencedirect.com/science/article/pii/S0008622398001432#FIG4`.

[24] Roger F. Cracknell, Peter Gordon, and Keith E. Gubbins. Influence of pore geometry on the design of microporous materials for methane storage. *Journal of Physical Chemistry*, 97(2):494–499, 1 1993. ISSN 00223654. doi: 10.1021/j100104a036. URL `https://pubs.acs.org/doi/abs/10.1021/j100104a036`.

[25] Erin E. Taylor, Kaitlin Garman, and Nicholas P. Stadie. Atomistic Structures of Zeolite-Templated Carbon, 4 2020. ISSN 15205002. URL `https://pubs.acs.org/doi/full/10.1021/acs.chemmater.0c00535`.

[26] Atsushi Gabe, Mohammed Ouzzine, Erin E. Taylor, Nicholas P. Stadie, Naoki Uchiyama, Tomomi Kanai, Yuta Nishina, Hideki Tanaka, Zheng Ze Pan, Takashi Kyotani, and Hirotomo Nishihara. High-density monolithic pellets of double-sided graphene fragments based on zeolite-templated carbon. *Journal of Materials Chemistry A*, 9(12):7503–7507, 3 2021. ISSN 20507496. doi: 10.1039/d0ta11625d. URL `https://pubs.rsc.org/en/content/articlehtml/2021/ta/d0ta11625d`.

[27] Sai Smruti Samantaray, Seth T. Putnam, and Nicholas P. Stadie. Volumetrics of hydrogen storage by physical adsorption, 6 2021. ISSN 23046740. URL `https://www.mdpi.com/2304-6740/9/6/45/htm`.

[28] Jarad A. Mason, Mike Veenstra, and Jeffrey R. Long. Evaluating metal-organic frameworks for natural gas storage. *Chemical Science*, 5(1):32–51, 11 2014. ISSN 20416520. doi: 10.1039/c3sc52633j. URL `https://pubs.rsc.org/en/content/articlelanding/2014/sc/c3sc52633j`.

[29] Deparment of Energy. DOE Technical Targets for Onboard Hydrogen Storage for Light-Duty Vehicles, 2018. URL `https://www.energy.gov/eere/fuelcells/doe-technical-targets-onboard-hydrogen-storage-light-duty-vehicles`.

[30] Nitin Muralidharan, Ethan C. Self, Marm Dixit, Zhijia Du, Rachid Essehli, Ruhul Amin, Jagjit Nanda, and Ilias Belharouak. Next-Generation Cobalt-Free Cathodes – A Prospective Solution to the Battery Industry's Cobalt Problem. *Advanced Energy Materials*, 12(9):2103050, 3 2022. ISSN 16146840. doi: 10.1002/aenm.202103050. URL `https://onlinelibrary.wiley.com/doi/full/10.1002/aenm.202103050`.

[31] Suresh K. Bhatia and Alan L. Myers. Optimum conditions for adsorptive storage. *Langmuir*, 22(4):1688–1700, 2006. ISSN 07437463. doi: 10.1021/la0523816. URL `https://pubs.acs.org/doi/abs/10.1021/la0523816`.

[32] Stepan Hlushak. Heat of adsorption, adsorption stress, and optimal storage of methane in slit and cylindrical carbon pores predicted by classical density functional theory. *Physical Chemistry Chemical Physics*, 20(2):872–888, 1 2018. ISSN 14639076. doi: 10.1039/c7cp06591d. URL `https://pubs.rsc.org/en/content/articlehtml/2018/cp/c7cp06591d`.

[33] Adam S. Hoffman, Joseph A. Singh, Stacey F. Bent, and Simon R. Bare. In situ observation of phase changes of a silica-supported cobalt catalyst for the Fischer-Tropsch process by the development of a synchrotron-compatible in situ/operando powder X-ray diffraction cell. *Journal of Synchrotron Radiation*, 25(6):1673–1682, 11 2018. ISSN 16005775. doi: 10.1107/S1600577518013942. URL `https://scripts.iucr.org/cgi-bin/paper?fv5092https://journals.iucr.org/s/issues/2018/06/00/fv5092/`.

[34] Josiah Willard Gibbs. On the equilibrium of heterogeneous substances. *American Journal of Science and Arts*, s3-16:441–458, 1878.

[35] Nicholas Stadie. *Synthesis and thermodynamic studies of physisorptive energy storage materials*. PhD thesis, 2013. URL `http://thesis.library.caltech.edu/7198/`.

[36] Cullen M Quine. REALIST, 6 2023. URL `https://github.com/cullenmq/REALIST`.

Chapter 5

IMPROVED MULTICOMPONENT MODELLING OF GAS ADSORPTION USING A THERMODYNAMICALLY CONSISTENT SOFTWARE PACKAGE: REALIST

"The road not taken looks real good now."

— T. Swift *"'Tis the Damn Season"*

This chapter has been adapted from:

Cullen M. Quine, Joel Chacko, David A. Boyd, Nicholas P. Stadie, and Brent T. Fultz. Improved multicomponent modelling of gas adsorption using a thermodynamically-consistent software package: REALIST. In preparation. 2023. C.M.Q conceptualized the project, conducted gas isotherm measurements, synthesized the carbon materials, built and analyzed the software required for thermodynamic characterization, and completed the majority of the writing in the manuscript.

5.1 Abstract

A new thermodynamic Python package (REALIST) was developed to fit pure gas experimental excess isotherms and to simulate mixed-gas adsorption. Two carbons were synthesized with a varying degree of activation, and compared to a commercial carbon (MSP-20). The pore morphology of the three activated carbons was characterized, showing a varying amount of ultramicropores between the three. At lower pressures, all samples showed similar uptake of CO_2. This is due to the strong interactions of CO_2 withinultramicropores. Ideal Adsorption Solution Theory (IAST) predictions showed that the carbon with the highest selectivity for CO_2 over

N_2 was due to lower N_2 uptake with reduced specific surface area. Measurements of mixed adsorption with a mixture of 10% CO_2 in N_2 were performed, showing good agreement between the simulated and measured values.

5.2   Introduction

Calls for the removal and sequestration of carbon dioxide have resulted in an increased interest in the simulation and measurement of mixed-gas adsorption equilibria on solid surfaces. Carbon sequestration solutions utilizing adsorption phenomena require enhanced selectivity of certain gas species in multi-component gas streams. Power plants have remained one of the main sources of CO_2 emissions as 1.5 gigatons were released in 2021 from coal and natural gas power plants.[1] Post-combustion flue gas exhausts are ~10% CO_2 in N_2, with an additional content of water vapor. Pre-combustion carbon capture involves removing CO_2 from syngas, a mixture made from reforming coal or methane into hydrogen and carbon dioxide before hydrogen combustion. Landfill gas is around 50% CO_2 in CH_4, and requires carbon dioxide removal to up-convert the gas mixture to renewable natural gas (RNG). Direct air capture (DAC) technologies have focused on removing CO_2 from atmospheric conditions (420 ppm of CO_2) using sorbent materials with high selectivity. Unfortunately, mixed-gas adsorption experiments are more challenging to conduct and predict than their pure gas counterparts.

Both physisorbents and chemisorbents adsorb gas through surface-gas interactions, known as adsorbent-adsorbate interactions. Chemisorbents form chemical surface bonds with specific gases, permitting high selectivity, but there is a high energy cost for material regeneration due to the strength of these bonds. Physisorbents operate through weaker van der Waals forces. These forces are proportional to the polarizability of the gas, making the fixed dipole of carbon dioxide energetically suitable for reversible physisorption at ambient temperature, especially at high CO_2 concentrations. The primary physical adsorbents being investigated for carbon dioxide capture from point sources include zeolites, MOFs, and activated carbons. Zeolite materials exhibit strong carbon binding energies due to their polar structure, resulting in higher CO_2 selectivity and regeneration costs. However, the polar structure (and in the case of aluminosilicate zeolites, charged frameworks) also enhances water adsorption, resulting in lower CO_2 capacity in the presence of water than carbon adsorbents.[2] MOFs have also been shown to have high uptake and selectivity of CO_2 over nitrogen, but generally suffer from high cost and either stability issues [3] or reduced CO_2 capacity [4] with water vapor, which is essential for post-combustion flue gas capture. Current research directions are addressing these setbacks to make MOFs viable candidates for carbon dioxide capture.[5, 6]

Activated carbons, while having lower selectivity than both MOFs and zeolites, exhibit a high gravimetric uptake of CO_2 and can be readily derived from sustainable biomass precursors. A promising method to improve activated carbon selectivity is by modification of the binding strength of gases in activated carbons by surface

functionalization [7–10] or by controlling the pore morphology.[11–13] Nutshells have been shown to be viable biomass sources for producing high surface area activated carbons suitable for gas adsorption studies. Pistachio shells were chosen herein for a study of the tunability of pore structure.[14–19]

Multicomponent gas adsorption is notoriously challenging to measure and is also more time consuming than its pure gas counterpart. Many researchers therefore only measure pure gas isotherms and then predict multi-component adsorption behaviour based on theoretical models. Ideal Adsorption Solution Theory (IAST) is one of the most common models for simulation of mixed-gas adsorption nearly 60 years after its inception.[20]

IAST adopts three fundamental assumptions:

- The adsorbed species form an ideal mixture (enthalpy of mixing is zero).

- Each lattice site is equally accessible by each adsorbed species (no sites exist that can be occupied only by one adsorbate species).

- The adsorption site energy and surface area are independent of coverage (i.e., there are no structural changes in adsorbent with coverage).

The violation of any of these assumptions can lead to deviations between experimental measurements and simulated results.[21] The spreading pressure π is the two-dimensional adsorption equivalent of the gas pressure and is determined for each adsorbate species i from an analogous version of the ideal gas law (see Chapter

2 for its derivation):

$$\pi A = kT \int_0^{p_i^0} \frac{n_i(T)}{P_i} dP_i. \tag{5.1}$$

The pure component partial pressure p_i^0 is determined from the following equation:

$$p_i = \chi_i p_i^0(\pi, T) \tag{5.2}$$

where χ_i is the molar adsorbed fraction of species i and p_i is gas phase partial pressure. This equation is an adsorption equivalent of Raoult's law for liquid mixtures, which states that the partial pressure in the gas phase of each component i of an ideal mixture is equal to the *vapor pressure* of the pure species i multiplied its fractional molar amount in the mixture. Multicomponent adsorption simulations based on IAST have shown results consistent with some mixed-gas experimental measurements where the above assumptions have held valid.[22–25]

A useful software package, pyIAST, can be used to provide mixed-gas predictions close to experimental measurements for many chemical and physical adsorption systems at low pressures.[26] However, this package is based on absolute uptake while experimental measurements of pure-component isotherms are always excess uptake measurements. Additionally, the current isotherm models built into pyIAST are temperature-independent single isotherm fits, requiring pure-component isotherms measured at the temperature of interest for simulation. Nonetheless, the usability and robustness of pyIAST has led to its widespread use as one of the primary software packages for mixed-gas adsorption, with hundreds of citations to date. Furthermore, the open-source nature, combined with good documentation, of

Figure 5.1: Synthesis approach to pistachio shell-derived activated carbon production.

the package enabled the incorporation of mixed-gas adsorption calculations into the thermodynamic package outlined in this work.

This study establishes an improved temperature-dependent statistical-mechanical based model incorporated in the REALIST Python package.[27] The software allows for both pure gas thermodynamic adsorption information and mixed-gas uptake predictions at varying temperature and pressures. Experimental pure-component excess adsorption equilibria were measured on three carbon materials, with complementary structures, and a carbon dioxide-nitrogen mixture was chosen to demonstrate the capabilities of REALIST. Materials with smaller pore sizes exhibited higher binding energies for CO_2, and higher selctivities over N_2, establishing that control pore structure is a viable tool to enhance selective CO_2 capture in mixed-gas streams.

5.3   Material Synthesis and Characterization

Pistachio shell-derived carbons were produced following a previously established KOH-activation procedure,[14] as illustrated in Figure 5.1. Raw pistachio

shells from the Wonderful Company were ground mechanically into 1-2 mm granules. The granules were dried overnight at 120°C in an oven and then pyrolysis was conducted in an alumina combustion boat in a tube furnace under 100 sccm N_2 flow. The furnace was heated at $10°\text{C}\,\text{min}^{-1}$ to 500°C and held for 2 h. The resulting char (~20% of original mass) was mixed with KOH flakes (90% reagent grade) in a 2:1 or 3:1 ratio by weight in water and dried overnight at 120°C. The KOH/char mixture was then activated in a stainless steel tube under 100 sccm N_2 flow. The temperature ramp was $10\,°\text{C}\,\text{min}^{-1}$ to 300 °C for 1 h (drying step) and $10°\text{C}\,\text{min}^{-1}$ to 700 or 800 °C for 2 h (activation step). The activated char was then rinsed with 0.1 M HCl followed by deionized water until the pH returned to 7, rinsed with isopropyl alcohol, and then dried at 100°C in an oven overnight. The resulting activated carbon is referred to as PCxKyC where x is the KOH:char ratio (2 or 3), and y is the final activation temperature in °C (700 or 800).

Pore volume and surface area measurements were obtained by measurements of N_2 and Ar adsorption up to 1 bar using a Micromeritics Tristar II apparatus, at 77 K or 87 K, respectively. Surface area was determined using the BET method. Pore size distribution was obtained using a non-local density functional theory with heterogeneous surfaces (NLDFT-HS) argon kernel using a dedicated software package (Micromeritics Microactive).[28]

Table 5.1: Processing Conditions and Microstructural Properties of carbon adsorbents investigated in this study

Name	KOH:C ratio	Act Temp $^\circ$C	Act Time min	SA_{BET} m^2/g	ρ_{bulk} g/mL	ρ_{skel} g/mL	V_{pore} mL/g
PC3K800C	3:1	800	120	2440	0.53	1.65	1.34
MSP-20	N/A	N/A	N/A	2080	0.14	1.73	1.02
PC2K700C	2:1	700	120	1240	0.67	1.77	0.644
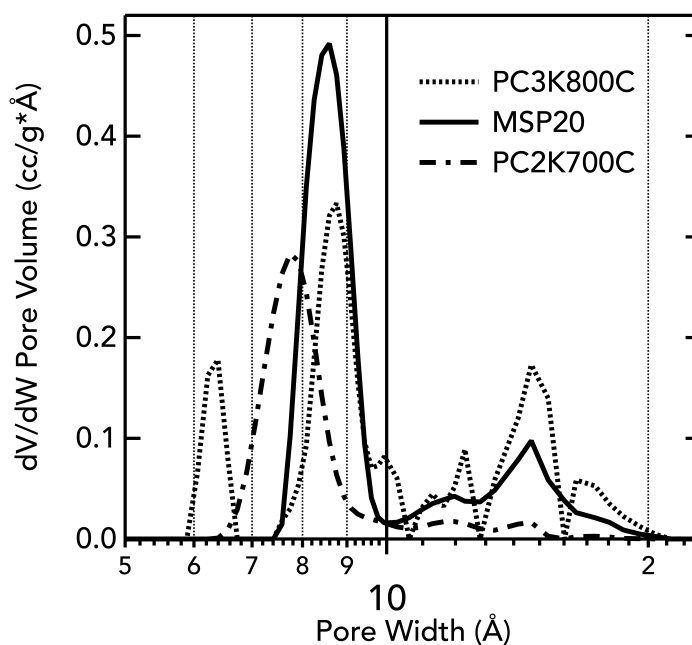
Figure 5.2: Pore size distributions on PC3K800C (dotted), MSP-20 (solid), and PC2K700C (dashed) obtained from 87 K Ar isotherms.

5.4 Results

Physical Properties

The processing conditions and material properties for each of the carbon materials are shown in Table 5.1. The pore-size distributions of all three samples are shown in Figure 5.2. PC2K700C has a majority of pores in the sub-nanometer regime with a main contribution centered around 7.8 Å. PC3K800C has a similar

pore size distribution as MSP-20, except with a broader distribution of pores. None

of the materials show significant porosity above 20 Å (mesopores).

Pure Component Isotherms

Pure component isotherms of hydrogen, methane, carbon dioxide, and nitrogen

were measured on PC2K700C, MSP-20, and PC3K800C using a custom Sieverts

apparatus. Isotherms were fit to a temperature-dependent double-site Langmuir

equation (see Chapter 2 for details):

$$n_e(f, P, T) = n_m(1 - \rho_g(P, T)v_m)\left((1 - \alpha)\frac{K_1 f}{1 + K_1 f} + \alpha\frac{K_2 f}{1 + K_2 f}\right) \qquad (5.3)$$

where n_e, n_{max} ρ_g, and v_a are the excess uptake, maximum absolute uptake, gas

phase density, and adsorbed phase volume, respectively. The K_i are temperature

dependent (based on the statistical mechanical partition function) and defined as:

$$K_i(T) = \frac{A_i}{\sqrt{T}}e^{-\frac{E_i}{RT}}. \qquad (5.4)$$

To fit n_{max} and v_a properly for experimental excess uptake measurements,

multiple isotherms with high coverage data are required (either by high pressures

or low temperatures, ideally near the fluid's liquid-gas saturation line or above the

critical point).

Nitrogen uptake measurements are shown in Figure 5.3 up to 100 bar, and

temperature from 233 to 393 K. PC2K700C has the lowest nitrogen uptake, followed

by MSP-20 and PC3K800C. The shape of the isotherms is similar for all samples, and

the samples have similar uptake at low pressures and high temperatures. Methane

uptake is shown in Figure 5.4 up to 100 bar, and temperatures from 240 to 328 K.
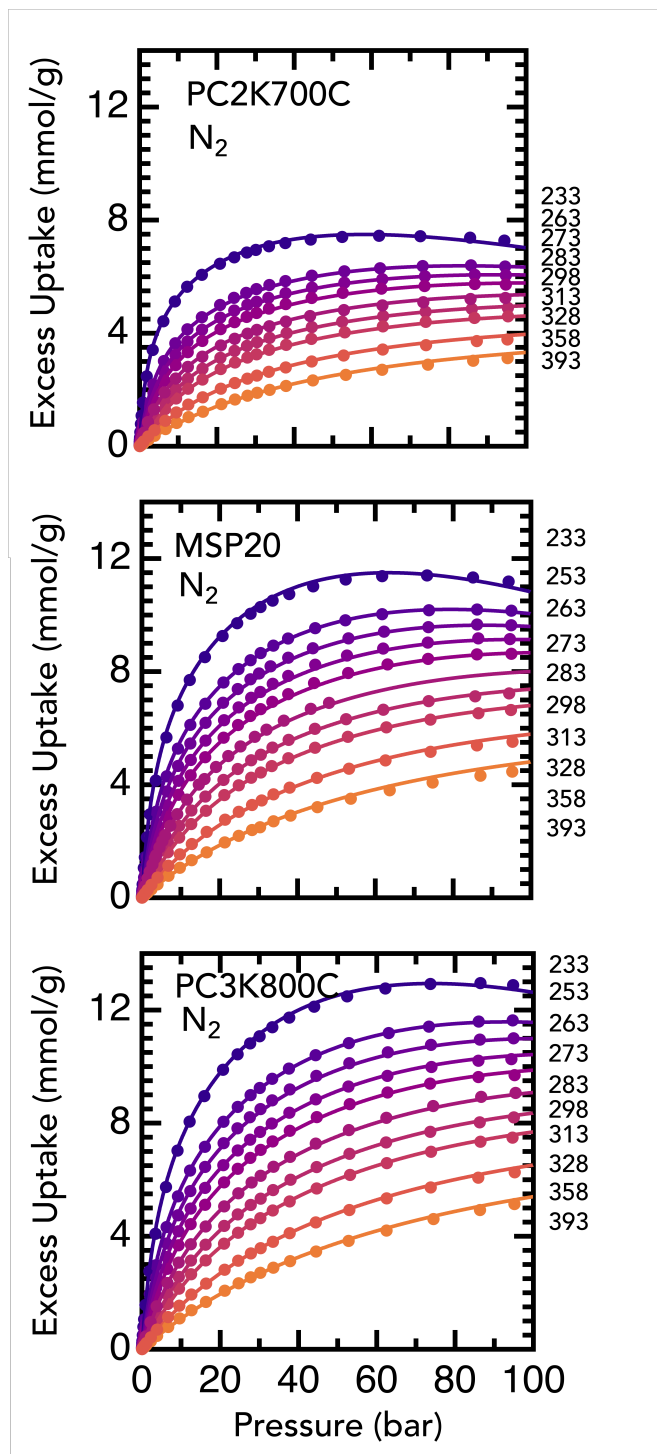
Figure 5.3: Excess uptake of nitrogen on PC2K700C (top), MSP-20 (middle), and PC3K800C (bottom) with experimentally measured data shown as points and double-site Langmuir shown as solid lines. Temperatures (in kelvin) are labelled at right.
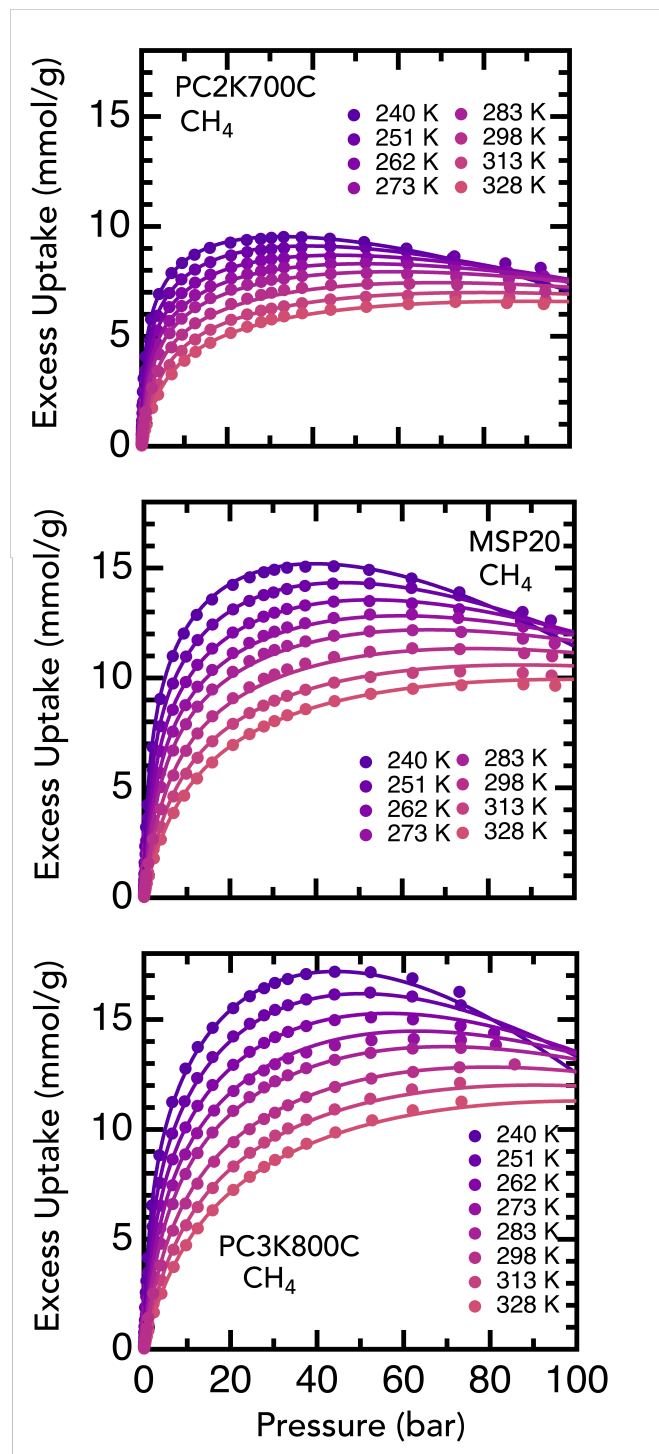
Figure 5.4: Excess uptake of methane on PC2K700C (top), MSP-20 (middle), and PC3K800C (bottom) with experimentally measured data shown as points and double-site Langmuir shown as solid lines. Temperatures (in kelvin) are labelled in the legends.

Excess uptake maxima occur at lower pressures than in the nitrogen isotherms, and all samples show high initial uptake at <10 bar. PC2K700C reaches maximum excess uptake at lower pressures than both MSP-20 and PC3K800C, and PC3K800C has the highest uptake.

Carbon dioxide uptake is shown in Figure 5.5 up to 50 bar (to prevent condensation) and from 263 to 398 K. Temperatures were chosen to satisfy both the high coverage limit as well as to explore temperatures of interest to post-combustion carbon capture conditions. At pressures below 3 bar, all samples demonstrated similar uptake of carbon dioxide. PC2K700C exhibited maximum excess uptake at lower pressures than MSP-20 and PC3K800C, with uptake increasing with MSP-20 and PC3K800C at higher pressures. Carbon dioxide isotherms for all samples did not show as pronounced of excess maxima as the other gases on the same materials owing to features of sub-critical adsorption phenomena.

IAST Predictions

IAST was used to predict multi-component gas adsorption behavior from the pure-component adsorption equilibria.[29] Extensions to the pyIAST Python package [26] were made to increase accuracy and robustness of the predictions.

The fundamental development of IAST (based on that shown by Simon et al.) [26] can be found in Chapter 2. Briefly, the use of the above assumptions enables the development of equations analogous to the partial pressure of a mixed-gas in equilibrium with a solution, where the "solution" is a two dimensional adsorbed
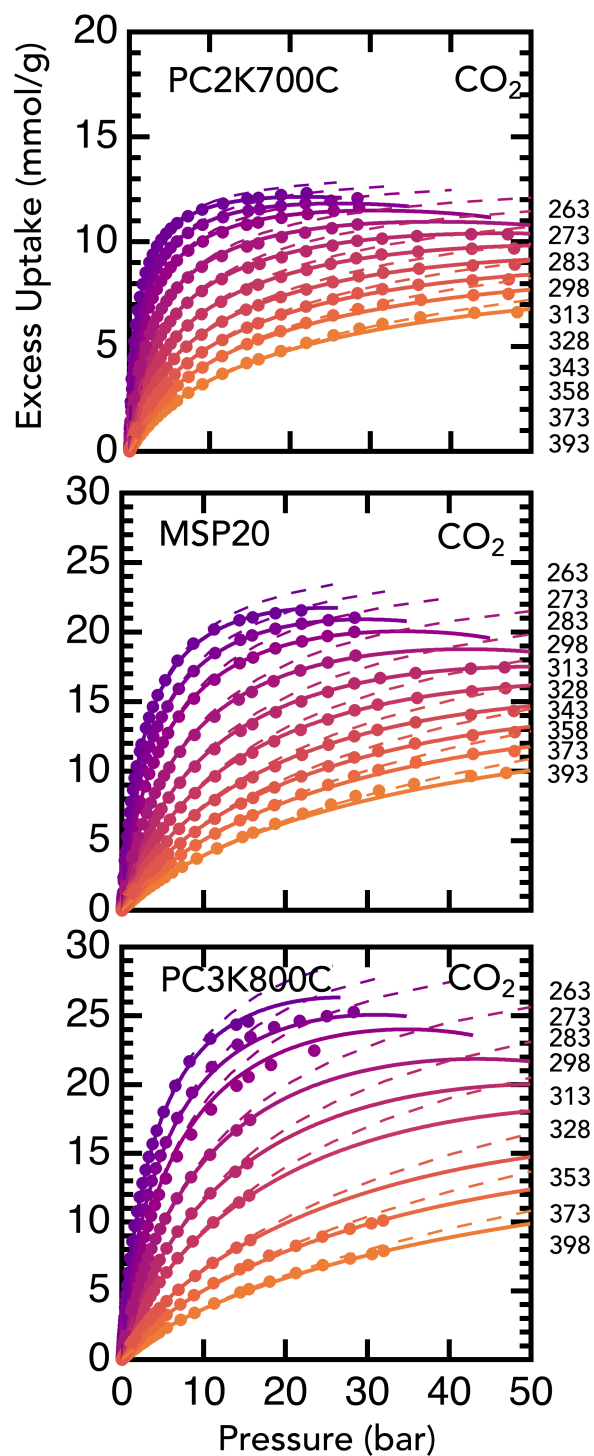
Figure 5.5: Carbon dioxide uptake on PC2K700C (top), MSP-20 (middle), and PC3K800C (bottom) with experimentally measured data shown as points and double-site Langmuir shown as solid lines (excess) and dashed lines (absolute). Temperatures (in kelvin) are labelled at right.

fluid on the surface of an adsorbent. Three equations are derived:

$$\pi_a(f_a^0) = \pi_b(f_b^0)... = \pi_n(f_n^0) \tag{5.5}$$

$$y_i \phi_i P = \chi_i \gamma_i f_i^0 \tag{5.6}$$

$$\sum_i^N \chi_i = 1. \tag{5.7}$$

The first equation states the adsorbed gases spreading pressure (which is a function of the pure component pressure p_i^0) are equal. Each adsorbed gas atom must experience the same surface chemical potential. The second equation is equivalent to Raoult's law, where the partial fugacity $f_i = \phi_i P_i = \phi_i y_i P$ in the gas mixture is equal to the pure-component equilibrium vapor fugacity multiplied by the adsorbed gas mole fraction χ_i and activity coefficient γ_i. Gas phase nonidealities (fugacity coefficient ϕ_i) were implemented coolProp.[30] Adsorbed phase nonidealities (activity coefficients) must be determined for a specific adsorbate/adsorbent combination, either experimentally or with high-accuracy computational models.[29] Most IAST experimental implementations, including this work, use the assumption that the adsorbates are non-interacting on the adsorbent ($\gamma_i = 1$). The known variables in these equations are the partial pressures in the gas phase $P_i = y_i P$ and temperature T. Once χ_i for each adsorbate i is determined, the total adsorbed gas uptake can be determined for an N component mixture using Eq. 5.8 (Eq. 2.73):

$$\frac{1}{n_T} = \sum_{i=1}^N \frac{\chi_i}{n_i}. \tag{5.8}$$

Each pure-component set of isotherms was fit globally (all temperatures and pressures at once). This has the added benefit of increasing the fit robustness to

measurement uncertainty, and enabling the prediction of any temperature, pressure, and composition for the system, even if the pure component isotherms are not measured under those conditions.

The spreading pressure for a double-site Langmuir isotherm is:

$$\pi(P) = n_{max} \left[(1 - \alpha) \ln(1 + K_1 P) + \alpha \ln(1 + K_2 P) \right]. \tag{5.9}$$

The improvements of our package over the original pyIAST package include:

- Universal fitting of excess (or absolute) isotherms to a statistical mechanical Langmuir model over temperature, pressure,

- Real gas corrections with fugacity,

- Predictions of gas uptake from mixtures at temperatures, pressures not directly measured experimentally or simulated computationally.

Figure 5.6 (left) shows the pressure, temperature, absolute uptake surfaces for CO_2 (green), N_2 (red), and N_2+CO_2 (colormap) for the 3 samples at a composition of 10% CO_2 in N_2. This mix was chosen to approximate the conditions of a dehydrated post-combustion flue gas mixture. PC3K800C and MSP-20 show a similar trend in absolute uptake, having 5 mmol g^{-1} CO_2 at 273 K and 0.8 mmol g^{-1} at 328 K. N_2 uptake is relatively constant compared to CO_2 uptake with uptake for both samples and reaches a maximum around 2.8 mmol g^{-1} at 273 K. PC2K700C has similar CO_2 uptake as the other two materials, however N_2 uptake is about half of MSP-20 and PC3K800C N_2 uptake over the same temperature and pressure range.
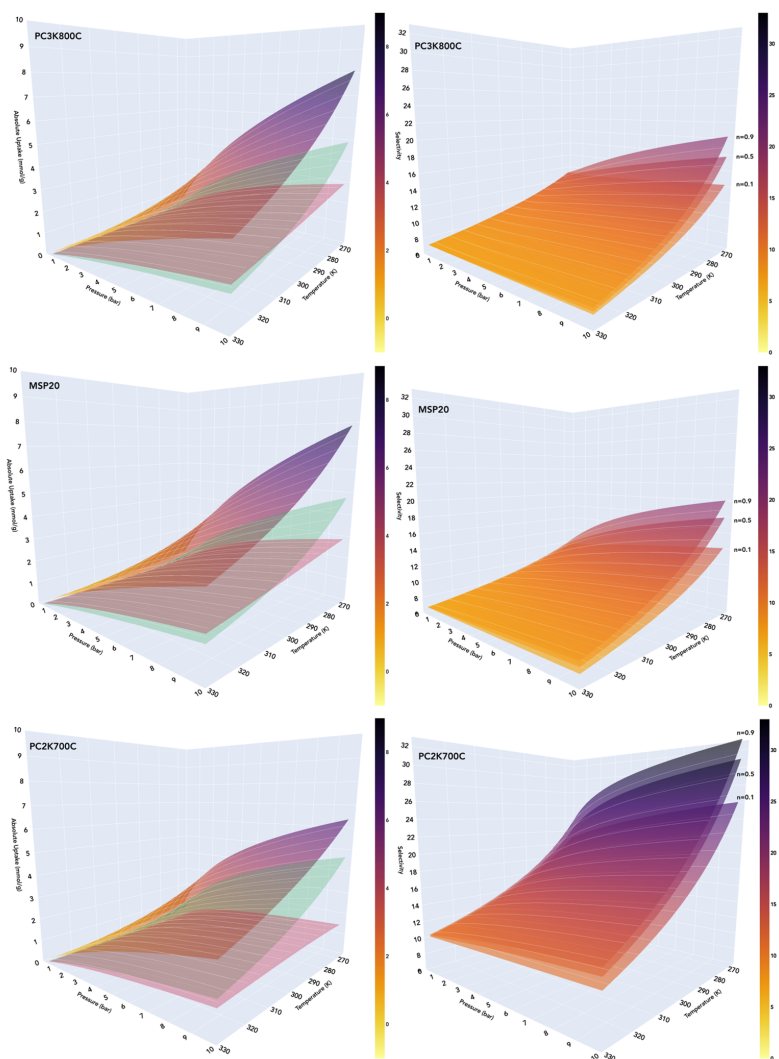
Figure 5.6: Simulated IAST (left) absolute gas uptake of CO_2 (green) N_2 (red) and CO2+N2 (inferno) of a 10% CO_2 in N_2 gas stream and (right) CO_2 selectivity of 10%, 50%, and 90% of CO_2 in N_2 on PC3K800C (top), MSP-20 (middle), and PC2K700C (bottom).

Gas selectivity is shown in Figure 5.6 (right) for the three samples at 10%, 50%, and 90% CO_2 in N_2 (bottom, middle, and top surface, respectively. At low pressure (low coverage), the three surfaces converge, approaching 13, 12, and 21 CO_2/N_2 selectivity at 273 K and 7, 7, and 10 at 328 K for PC3K800C, MSP-20, and PC2K700C, respectively. The selectivity dependence on gas concentration increases at higher pressures, with PC2K700C reaching maximum selectivity values of 33,

31, and 26 at 273 K, 10 bar for 10%, 50%, and 90% CO_2 in N_2, respectively.

Mixed Gas Experiments
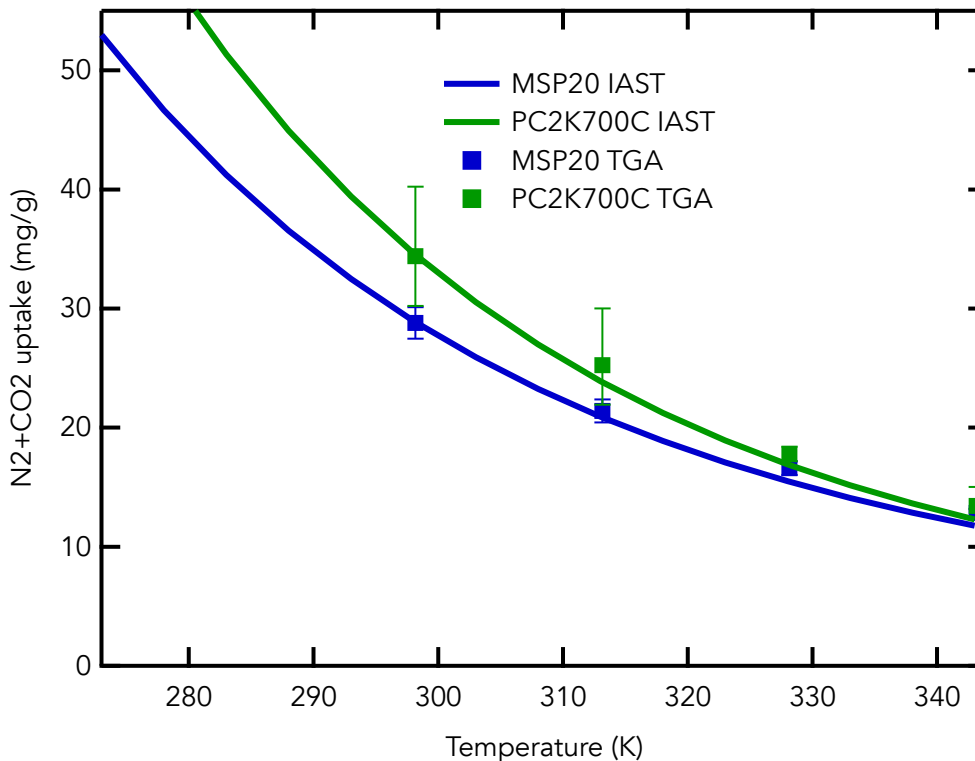
Figure 5.7: Comparison of pyIAST predictions (solid lines) at 10% CO_2 in N_2 with experimental measurements using thermogravimetric analysis (squares) at 100 sccm for MSP-20 (blue) and PC2K700C (green). Data corrected for flow rate using pure gas N_2 and CO_2 measurements and error bars determined from deviations between calibration measurements (see Supporting Information).

Finally, actual mixed-gas measurements were conducted using the open gravimetric technique [31] at ambient pressure conditions using a thermogravimetric analyzer (TGA) for total component excess gas measurement, and a residual gas analyzer in an open volumetric (OV) configuration at several temperatures. A gas mixture containing 10% CO_2 in N_2 was used. The open technique ensures that the bulk mixed-gas remains at a fixed composition in all experiments. The results of

Table 5.2: Gas polarizabilities [32] and enthalpies of adsorption at 298 K and zero coverage from the double-site Langmuir fit for each adsorbent.

	α_p $10^{-24}\,cm^3$	PC2K700C $-\Delta h_{ads,0}$ kJ/mol	MSP-20 $-\Delta h_{ads,0}$ kJ/mol	PC3K800C $-\Delta h_{ads,0}$ kJ/mol
H_2	0.804	8.12	8.74	8.67
N_2	1.74	15.72	14.21	13.46
CH_4	2.59	19.11	17.09	16.82
CO_2	2.91	24.18	20.74	20.79

the mixed-gas measurements are shown in Fig. 5.7. IAST predictions are based on absolute uptake, while TGA measurements are excess uptake. Since the measurements were conducted at 1 bar with low CO_2 concentrations, the absolute uptake of both nitrogen and carbon dioxide in the adsorbent is similar to the excess uptake measurements. This is valid as long as the gas phase contribution is much less than the amount of adsorbed gas. This equivalence breaks down at higher pressures and lower temperatures (see SI for plots of excess and absolute uptake).

5.5   Discussion

The pure isotherm behavior shows the direct effect of pore structure and surface area on uptake. While the maximum uptake is dependent on surface area, the shape of the isotherm depends both on the adsorbate polarizability and pore morphology. PC3K800C and MSP-20 generally had higher gas uptakes for all the measured gases at high pressures due to increased surface area (number of adsorption sites) over PC2K700C. Hydrogen has the lowest polarizability of the measured gases, followed by nitrogen, methane and carbon dioxide (see Table 5.2). Nitrogen uptake

depends primarily on accessible surface area near ambient temperature, with larger surface area materials showing higher nitrogen uptake than the lower surface area materials. Methane, being more polarizable but not having a fixed dipole moment, shows increased uptake with surface area at higher pressures/lower temperatures, but nonetheless shows a sharp increase in uptake at low pressures in all materials.

The high degree of polarizability for carbon dioxide results in adsorption behavior being sensitive to pore morphology. Carbon dioxide, having a quadropole moment and slightly higher polarizability than methane, has strong interactions with carbon surfaces. For carbon dioxide uptake at pressures below 3 bar, the structural properties (pore morphology, surface functionalization, etc.) are more important than accessible surface area, and all of the materials show similar uptakes despite having large differences in surface areas. The strong interactions of carbon dioxide with the carbon surfaces also results in increased surface coverage at lower pressures than with other gases, resulting in a sharp increase in gas uptake.

A thermodynamic metric for the strength of gas binding to adsorbents, the adsorption enthalpy, is dependent on both the pore structure and gas polarizability. The enthalpy of adsorption at zero coverage, known as the Henry's law enthalpy, is calculated by extrapolating the double-site Langmuir isotherm to $\theta = 0$ (see Supporting Information for details on fits). Both the magnitude and the sensitivity of the strength of adsorption to the pore size increases with the polarizability of the gas α_p, as shown in Table 5.2, except for hydrogen which shows negligible differences between the carbon materials at 298 K. The material with the largest relative per-

centage of ultramicropores (PC2K700C) shows the highest zero coverage isosteric heat of adsorption for each adsorbate while PC3K800C shows the lowest adsorption heats. Furthermore, the difference between the highest and lowest enthalpies increases with increasing gas polarizability, further illustrating the sensitivity of adsorption binding strength to pore morphology and adsorbate type.

IAST calculations require absolute uptake, however all measurements are excess uptakes. Since the gas phase density is much lower than the adsorbed phase density at low pressures and high temperatures, excess uptake measurements closely match absolute uptake under these conditions. Many studies assume these conditions in their IAST predictions, which limit reliable calculations to low pressures. The adsorbed volume parameter v_a is essential to transform excess measurements into absolute uptake data used in pyIAST predictions.

All of the adsorption fits in this study show high coverage at the low-temperature and high-pressure measurement conditions, which is required for an accurate fitting of the adsorbed volume. A further validation is that the adsorbed phase density is near the adsorbate's liquid density. As noted above, the nitrogen and methane excess uptake reach maxima before decreasing at high pressures due to the increase in the gas phase density. The carbon dioxide excess isotherms reach a plateau and closely match the absolute isotherms, unlike the other pure gases measured (see SI for absolute vs excess plots). Due to strong interactions of CO_2 with carbon surfaces, excess CO_2 excess measurements closely match absolute uptakes over a larger range of coverage than other gases. This increases the validity of using

excess measurements directly with pyIAST over a larger pressure range for carbon adsorbents than with other gases.

The dependence of CO_2 selectivity on pore structure is further established from the IAST predictions. PC2K700C shows much higher selectivity of carbon dioxide over nitrogen due to the decreased nitrogen uptake in this material relative to the other samples with carbon dioxide uptake similar for all samples in the 10% mixture. This is seen in Figure 5.6 (left) with the carbon dioxide surface intersecting the nitrogen surface at lower temperatures for MSP-20 and PC3K800C than with PC2K700C. Nitrogen uptake scales with surface area and carbon dioxide uptake is more dependent on pore microstructure. To maximize carbon dioxide selectivity, it is more advantageous to have a low surface area material with ultramicropores.

The pyIAST predictions of combined nitrogen and carbon dioxide uptake amounts are consistent with the mass change measured by the TGA under the same conditions (as shown in Figure 5.7). This demonstrates both the reliability and the robustness in the prediction for near-ambient carbon capture from a simulated flue-gas composition over a large range of temperature. While the statistical model presented in this work was specifically designed for physisorbents, the partition function (the prefactor temperature dependence of the Langmuir constant) can be modified for chemical adsorption modelling.

5.6 Conclusion

A new Python-based package REALIST was developed based on temperature-dependent thermodynamic isotherm models to fit pure-gas and simulate mixed-gas adsorption from experimental excess isotherm fits. Two pistachio shell-derived activated carbons PC2K700C and PC3K800C were synthesized with a varying degree of activation, and compared to a commercial carbon MSP-20. Strong interactions of CO_2 with carbon highlights the importance of pore morphology (relative amount of ultramicropores) for CO_2 capture at low pressures. IAST selectivity predictions show that at low CO_2 partial pressures, the small pore morphology of PC2K700C has higher selectivity for CO_2 in N_2 than the other materials, despite the material having a lower specific surface area overall. Carbon dioxide uptake in the carbon materials scales with surface area at higher pressures (20 bar), demonstrating a potential use for high surface area adsorbents as temporary storage mediums for carbon dioxide. A mixture of 10% CO_2 in N_2 was selected to compare with the IAST predictions, showing good agreement between the simulated and measured values. Future experimental measurements need to be conducted with other mixtures/adsorbates to determine the degree of success of these new models.

5.7 Acknowledgements

5.8   Supporting Information

Experimental Isotherms with Thermodynamic Fits

The full derivation for the thermodynamic model and the Ideal Adsorption Solution Theory is shown in Chapter 2. The double-site Langmuir equation used for fitting experimental uptake measurements is given by Eq. 2.28:

$$n_e(P,T) = (n_m - \rho_g(P,T)v_m)\left((1-\alpha)\frac{K_1(T)f}{1+K_1(T)f} + \alpha\frac{K_2(T)f}{1+K_2(T)f}\right) \quad (5.10)$$

where n_e is the excess uptake, n_m is the maximum absolute uptake at full coverage, ρ_g is the gas phase density, v_m is the adsorbed gas volume at full coverage, α is a weighting factor for adsorption site 1 over site 2, f is the fugacity of the gas to correct for non-ideal behavior in the gas phase, and K_i is the Langmuir constant, which varies with temperature.

For all (physisorbed) gases analyzed in this chapter, a two dimensional adsorbed phase with a classical translational vibrational component was used such that the partition function has the same functional form for every gas (Eq. 2.4):

$$q_i(T) = q_{i,\text{trans}}q_{i,\text{vib}} = \frac{A_{\text{B},i}}{\lambda_{\text{ads}}^2}\frac{k_\text{B}T}{\hbar\omega} \quad (5.11)$$

$$\lambda_{\text{ads}} = \left(\frac{2\pi\hbar^2}{mk_\text{B}T}\right)^{1/2} \quad (5.12)$$

which gives the following temperature dependence for the prefactor (Eq. 2.13):

$$K_i = \frac{A_i}{\sqrt{T}}e^{-\beta\varepsilon_i}. \quad (5.13)$$

The main assumptions for the double-site Langmuir isotherm used for fitting is that the adsorbed gas is non-interacting on the surface, has monolayer coverage,

and has the same adsorbed phase density and behavior over the entire range of temperature and pressure fitted.

The total volumetric uptake is determined using Eq. 2.32:

$$n_{t,v} = n_{e,v} + (\rho_g v_{g,\text{STP}} X_{\text{pore}})$$ (5.14)

$$n_{e,v}(P,T) = n_e(P,T) \rho_{\text{bulk}} v_{g,\text{STP}}$$ (5.15)

where $n_{t,v}$ is the total volumetric uptake, $n_{e,v}$ is the excess volumetric uptake, and X_{pore}, $v_{g,\text{STP}}$, ρ_g, and ρ_{bulk} are the void fraction of bulk material, molar gas volume at $0\,°\text{C}$, 1 bar, gas phase density, and bulk sample density, respectively.

To determine the total volumetric uptake, X_{pore} must be determined. The common method described in literature is given as:

$$X_{\text{pore,common}} = \frac{v_{N_2}}{v_{\text{bulk}}} = \rho_{\text{bulk}} v_{\text{pore}}.$$ (5.16)

where the bulk density ρ_{bulk} for the samples in this chapter was determined using a combination of tap density/syringe and the pore volume v_{pore} was determined from $77\,\text{K}$ N_2 measurements.

The isosteric heat of adsorption q_{st}, which is defined as the positive quantity of the enthalpy of adsorption, $-\Delta h_{\text{ads}}$, is determined from Eq. 2.47:

$$q_{\text{st}} \equiv -\Delta h = -T \left(\frac{\partial P}{\partial T}\right)_{n_a} \left(\frac{v_{\text{m}}}{n_{\text{m}}} - \frac{1}{\rho_{\text{g}}}\right).$$ (5.17)

The $\left(\frac{\partial P}{\partial T}\right)_{n_a}$ is dependent on the adsorption model used (specifically site occupancy θ), and can be determined with the following relationships

$$-\left(\frac{\partial P}{\partial T}\right)_n = \frac{\left(\frac{\partial \theta}{\partial T}\right)_{P,n}}{\left(\frac{\partial \theta}{\partial P}\right)_{T,n}}.$$ (5.18)

For the double-site physisorption Langmuir model used in this chapter:

$$\frac{\partial \theta}{\partial P} = (1 - \alpha) \left(\frac{K_1}{(1 + K_1 P)^2} \right) + \alpha \left(\frac{K_2}{(1 + K_2 P)^2} \right) \tag{5.19}$$

$$\frac{\partial \theta}{\partial T} = (1 - \alpha) \frac{\partial \theta}{\partial K_1} \frac{\partial K_1}{\partial T} + \alpha \frac{\partial \theta}{\partial K_2} \frac{\partial K_2}{\partial T} \tag{5.20}$$

$$\frac{\partial \theta}{\partial K_i} \frac{\partial K_i}{\partial T} = - \left(\frac{P}{(1 + K_i P)^2} \right) (xRT + \varepsilon_i) \frac{K_i}{RT^2}. \tag{5.21}$$

where the gas constant R is used in place of Boltzmann's constant k_B to get energy quantities in terms of kJ/mol and the energies ε_1 and ε_2 are negative for adsorption. x is the power of the prefactor temperature dependence (as determined from the adsorbate partition function). In this case with the above adsorption partition function, $x = 0.5$.

Sample	n_m	v_m	α	A_1	$-\varepsilon_1$	A_2	$-\varepsilon_2$	RSSR/pt
	mmol/g	mL/g		$\sqrt{K}/MPa$	kJ/mol	$\sqrt{K}/MPa$	kJ/mol	mmol/g
PC3K800C	36.1	2.21	0.943	0.0621	8.75	0.0138	6.59	0.002
MSP-20	20.7	0.631	0.788	0.109	7.08	0.00438	8.87	0.005
PC2K700C	17.5	0.191	0.592	0.0678	6.89	0.00159	6.70	0.01

Table 5.3: Double-site Langmuir coefficients for hydrogen on PC3K800C, MSP-20, and PC2K700C using Eq. 4.5.

Figure 5.8: Hydrogen measurements on carbon materials. Experimental excess (circles) with excess (solid) and absolute (dotted) fits (left), total volumetric uptake (middle), and enthalpy of adsorption (right) on PC3K800C (top), MSP-20 (middle), and PC2K700C (bottom).

Sample	n_m	v_m	α	A_1	$-\varepsilon_1$	A_2	$-\varepsilon_2$	RSSR/pt
	mmol/g	mL/g		$\sqrt{K}/MPa$	kJ/mol	$\sqrt{K}/MPa$	kJ/mol	mmol/g
PC3K800C	25.6	1.35	0.721	0.0582	12.55	0.0100	10.68	0.003
MSP-20	22.3	1.35	0.716	0.0533	13.26	0.00818	11.41	0.004
PC2K700C	12.1	0.639	0.632	0.0436	14.62	0.489	13.16	0.002

Table 5.4: Double-site Langmuir coefficients for nitrogen on PC3K800C, MSP-20, and PC2K700C using Eq. 4.5.

Figure 5.9: Nitrogen measurements on carbon materials. Experimental excess (circles) with excess (solid) and absolute (dotted) fits (left), total volumetric uptake (middle), and enthalpy of adsorption (right) on PC3K800C (top), MSP-20 (middle), and PC2K700C (bottom).

Sample	n_m	v_m	α	A_1	$-\varepsilon_1$	A_2	$-\varepsilon_2$	RSSR/pt
	mmol/g	mL/g		$\sqrt{K}/MPa$	kJ/mol	$\sqrt{K}/MPa$	kJ/mol	mmol/g
PC3K800C	30.2	1.76	0.679	0.0363	16.01	0.0103	12.24	0.008
MSP-20	22.1	1.11	0.571	0.0469	15.87	0.00312	15.66	0.008
PC2K700C	12.2	0.578	0.528	0.0407	17.9	0.00271	17.21	0.006

Table 5.5: Double-site Langmuir coefficients for methane on PC3K800C, MSP-20, and PC2K700C using Eq. 4.5.
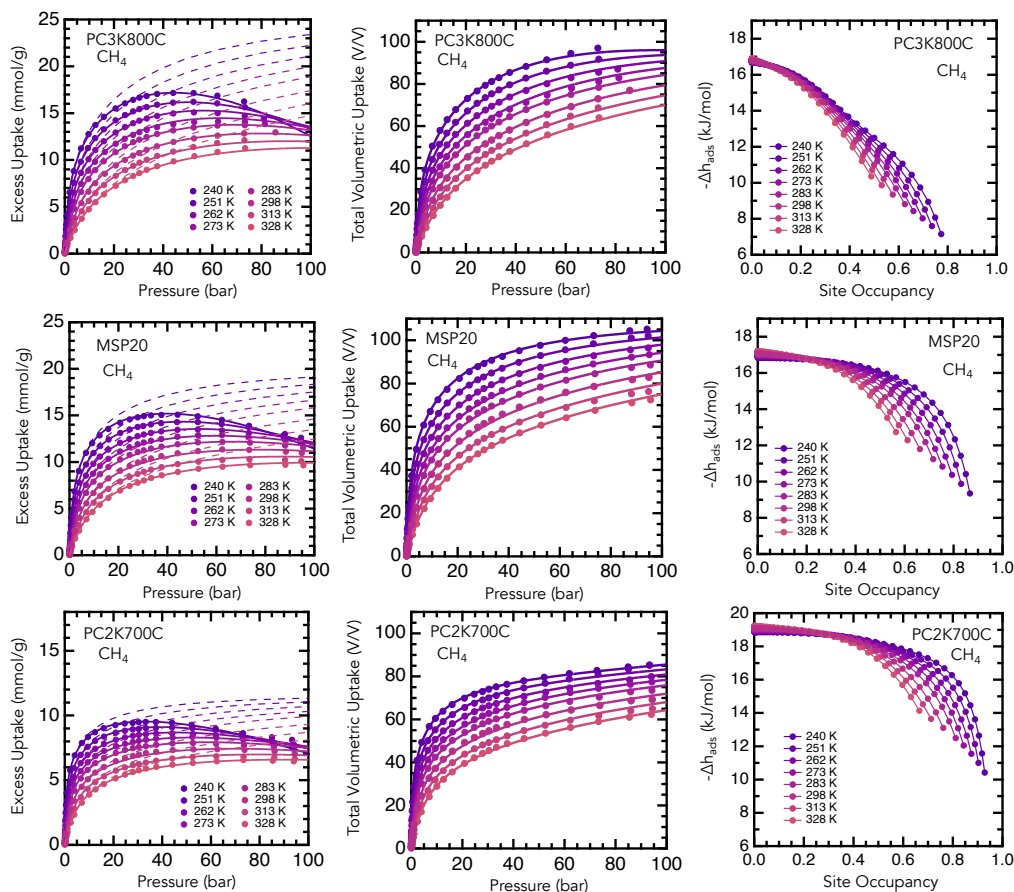
Figure 5.10: Methane measurements on carbon materials. Experimental excess (circles) with excess (solid) and absolute (dotted) fits (left), total volumetric uptake (middle), and enthalpy of adsorption (right) on PC3K800C (top), MSP-20 (middle), and PC2K700C (bottom).

Sample	n_m	v_m	α	A_1	$-\varepsilon_1$	A_2	$-\varepsilon_2$	RSSR/pt
	mmol/g	mL/g		$\sqrt{K}/MPa$	kJ/mol	$\sqrt{K}/MPa$	kJ/mol	mmol/g
PC3K800C	35.4	1.84	.918	0.053	19.79	0.004	19.24	0.008
MSP-20	27.3	1.25	0.873	0.0412	19.74	0.00637	19.22	0.005
PC2K700C	13.8	0.501	0.656	0.0177	23.14	0.00306	21.97	0.004

Table 5.6: Double-site Langmuir coefficients for carbon dioxide on PC3K800C, MSP-20, and PC2K700C using Eq. 4.5.

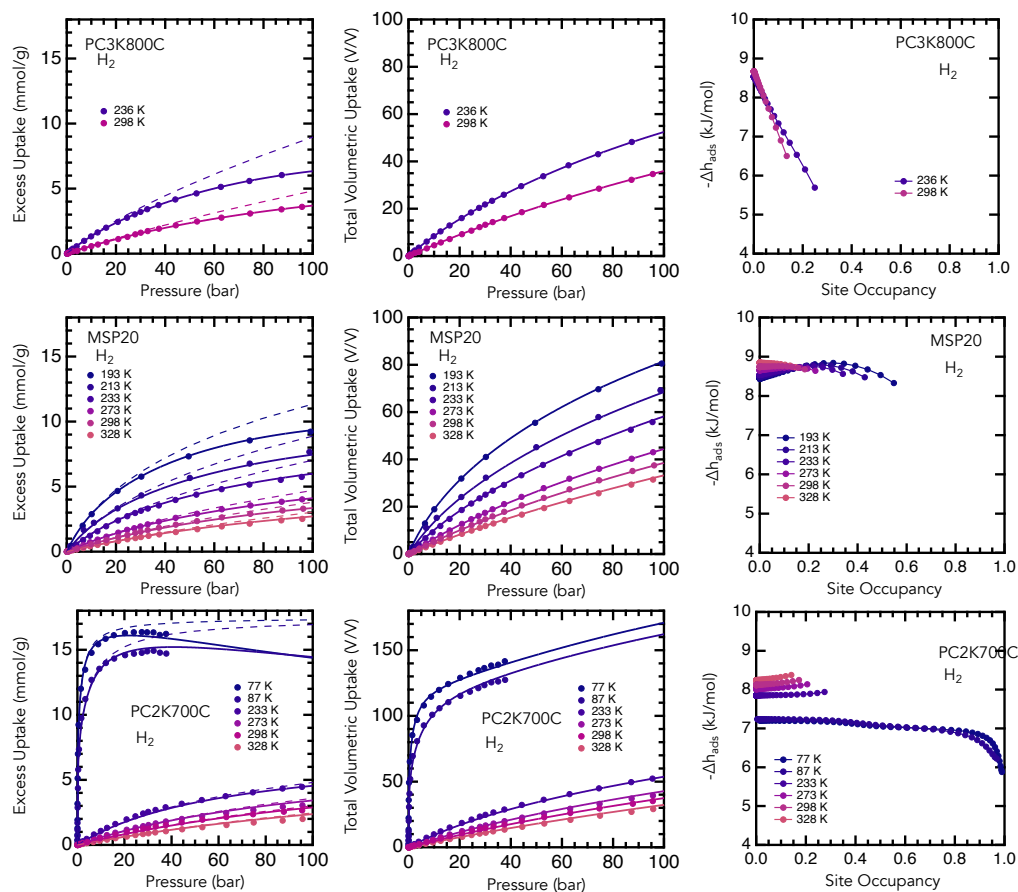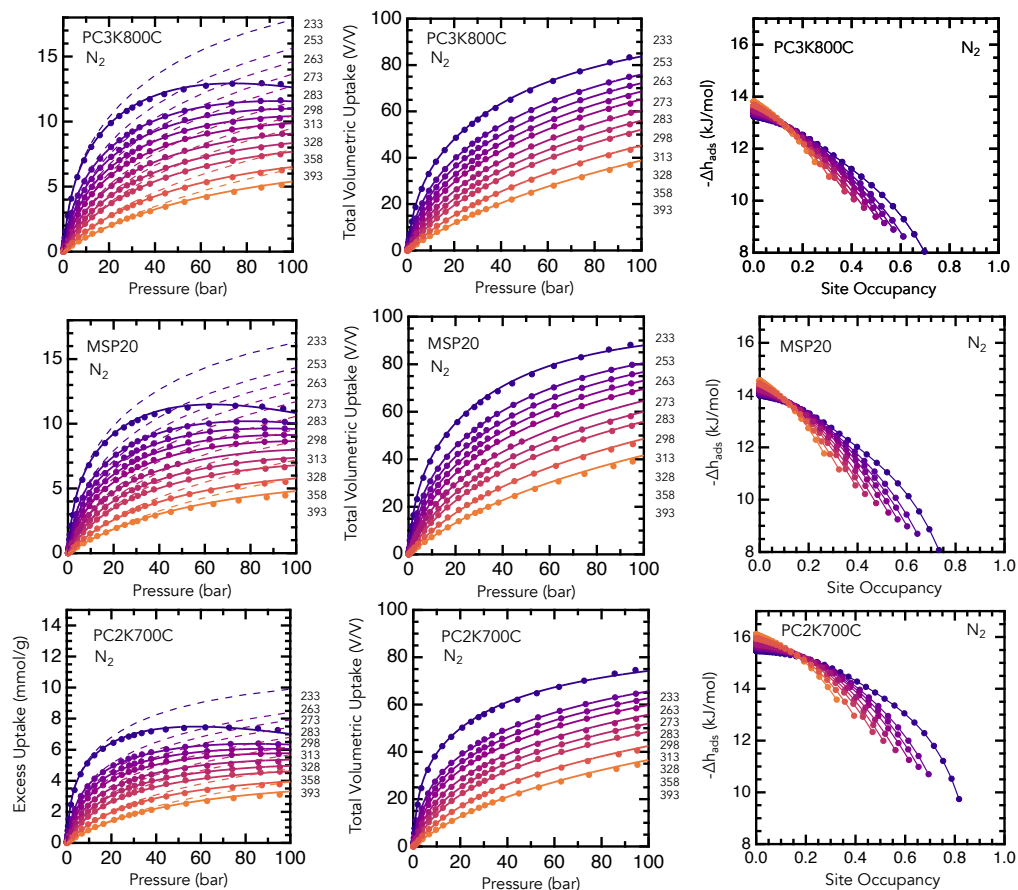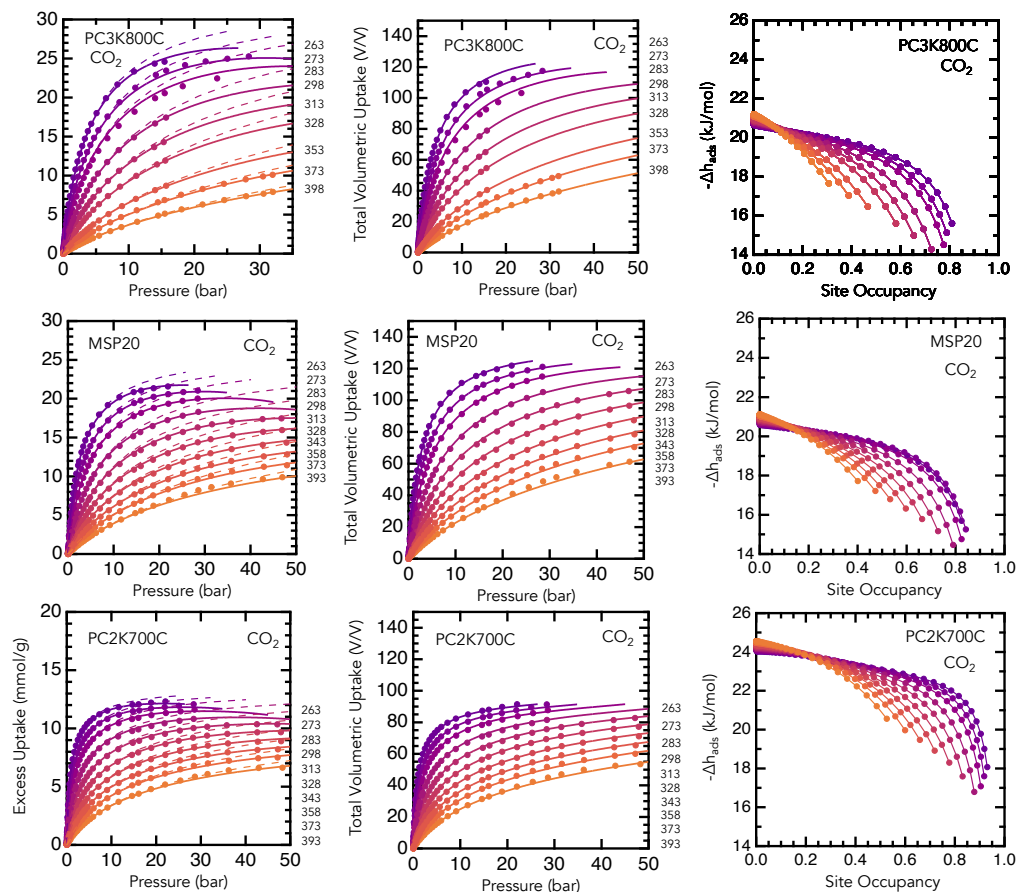Figure 5.11: Carbon dioxide measurements on carbon materials. Experimental excess (circles) with excess (solid) and absolute (dotted) fits (left), total volumetric uptake (middle), and enthalpy of adsorption (right) on PC3K800C (top), MSP-20 (middle), and PC2K700C (bottom).

Thermogravimetric Gas Analysis Experiments

A 9.85% CO_2 in N_2 mixture (EPA protocol 2% analysis, Airgas) was used with a thermogravimetric analyzer (TGA) to determine total mixed-gas uptake in each sample to compare with the IAST predictions. To correct for non-idealities in the experimental procedure (i.e., mass change due to buoyancy or gas flow), experiments of pure N_2 and CO_2 were conducted under the same conditions as the mixed-gas experiment. A correction factor for N_2 and CO_2 was determined for each temperature by dividing the measured Sieverts isotherms at the same thermodynamic conditions by the pure component TGA measurements. A simple weighting of the correction factors based on the gas mixture (9.85%) was applied to the measured mixture TGA uptake data.
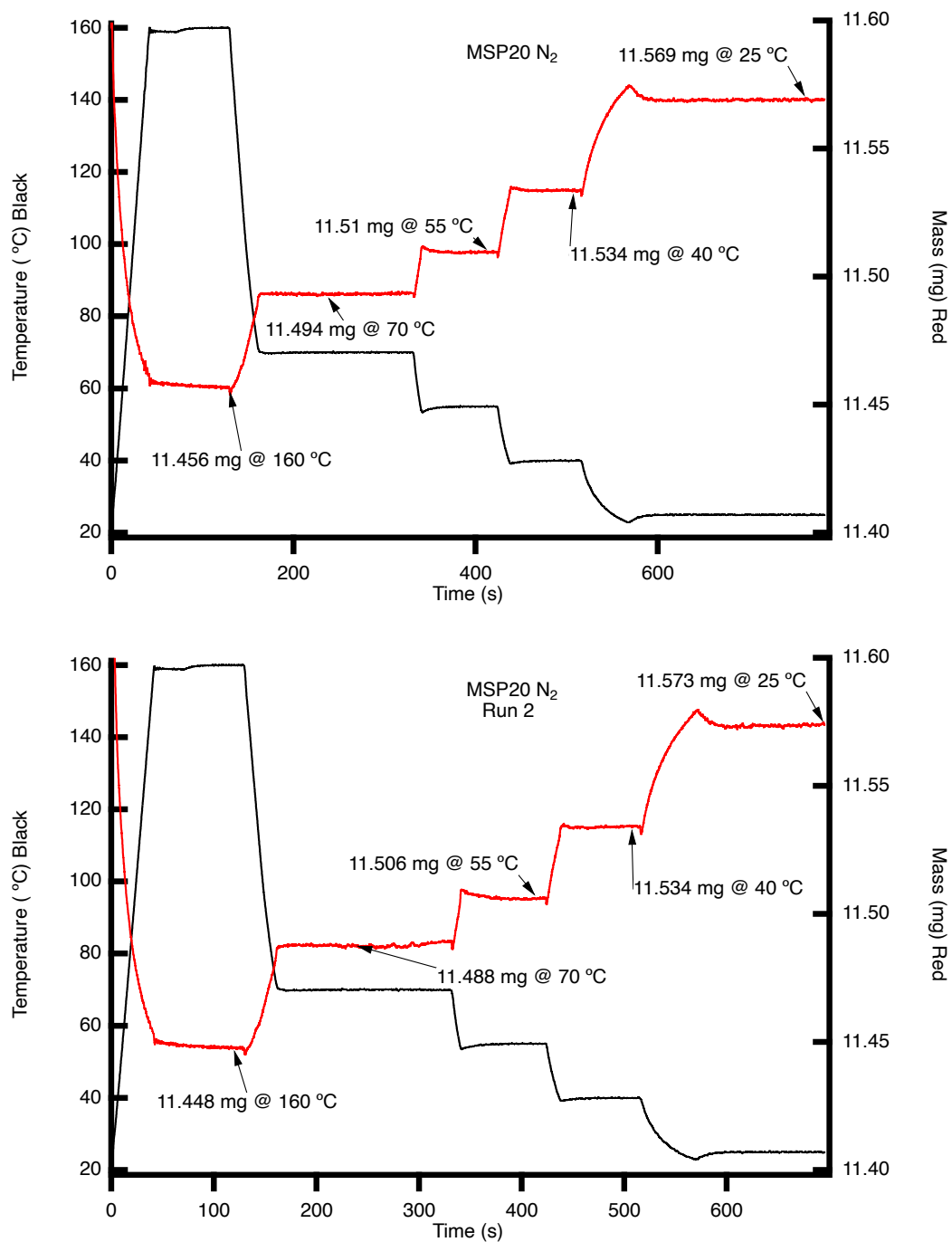
Figure 5.12: 50 sccm N_2 1 bar TGA calibration on MSP-20 for two runs. Sample heated at 20 °C/min under 50 sccm N_2 flow to 160 °C for 1 hour to determine sample mass.
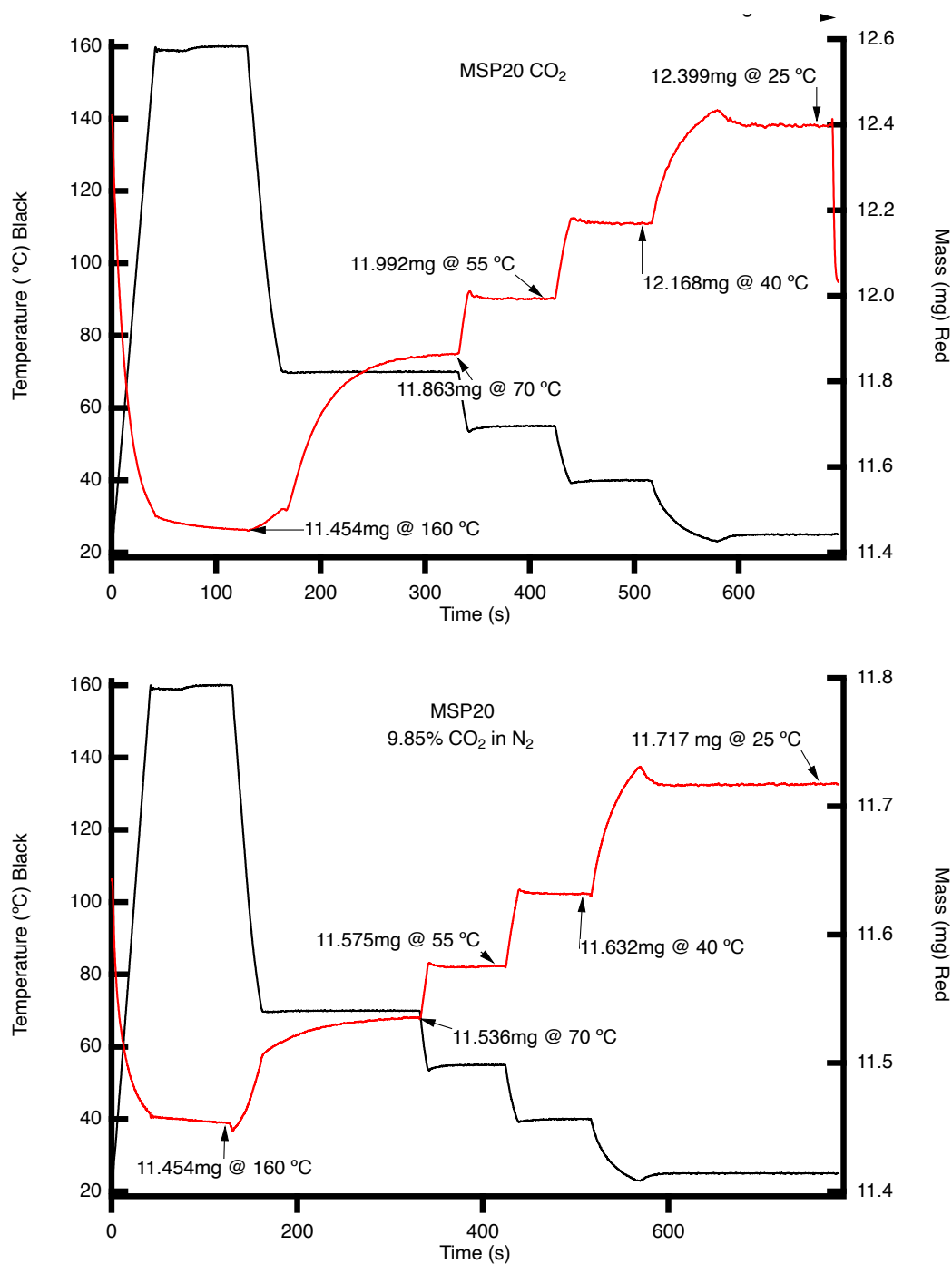
Figure 5.13: 50 sccm CO_2 1 bar TGA calibration (top) and 9.85% CO_2 balance N_2 mixture (Airgas, EPA protocol) measurement (bottom) on MSP-20. Sample heated at 20 °C/min under 50 sccm N_2 flow to 160 °C for 1 hour to determine sample mass, switched to 50 sccm measurement gas flow and cooled at 15 °C/min to each set temperature and held for 1 hour at each setpoint.
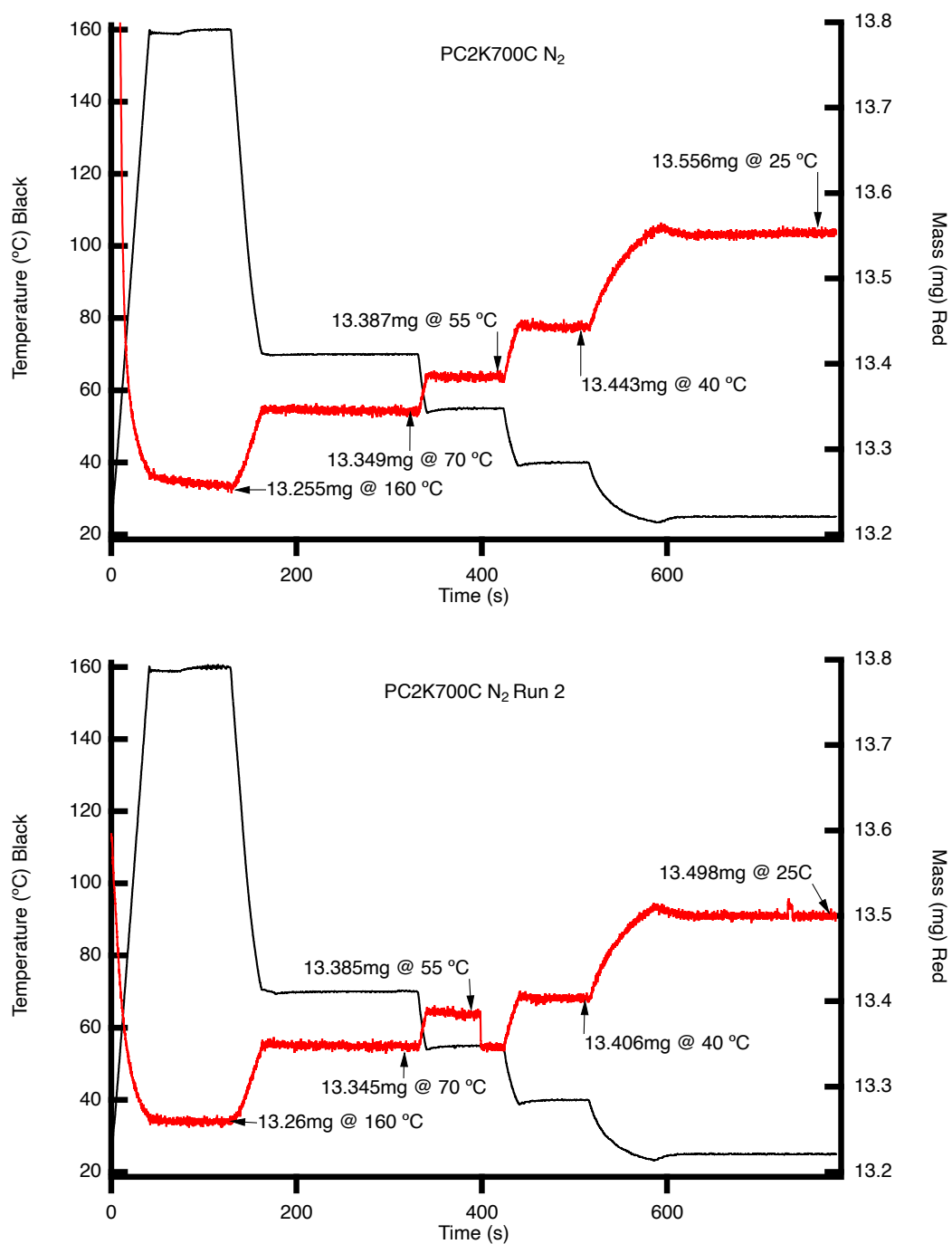
Figure 5.14: 50 sccm N_2 1 bar TGA calibration on PC2K700C for two runs. Sample heated at 20 °C/min under 50 sccm N_2 flow to 160 °C for 1 hour to determine sample mass.

Figure 5.15: 50 sccm CO_2 1 bar TGA calibration (top) and 9.85% CO_2 balance N_2 mixture (Airgas, EPA protocol) measurement (bottom) on PC2K700C. Sample heated at 20 °C/min under 50 sccm N_2 flow to 160 °C for 1 hour to determine sample mass, switched to 50 sccm measurement gas flow and cooled at 15 °C/min to each set temperature and held for 1 hour at each setpoint.

References

[1] EIA. Total Energy Monthly Data - U.S. Energy Information Administration (EIA), 2021. URL `https://www.eia.gov/totalenergy/data/monthly/`.
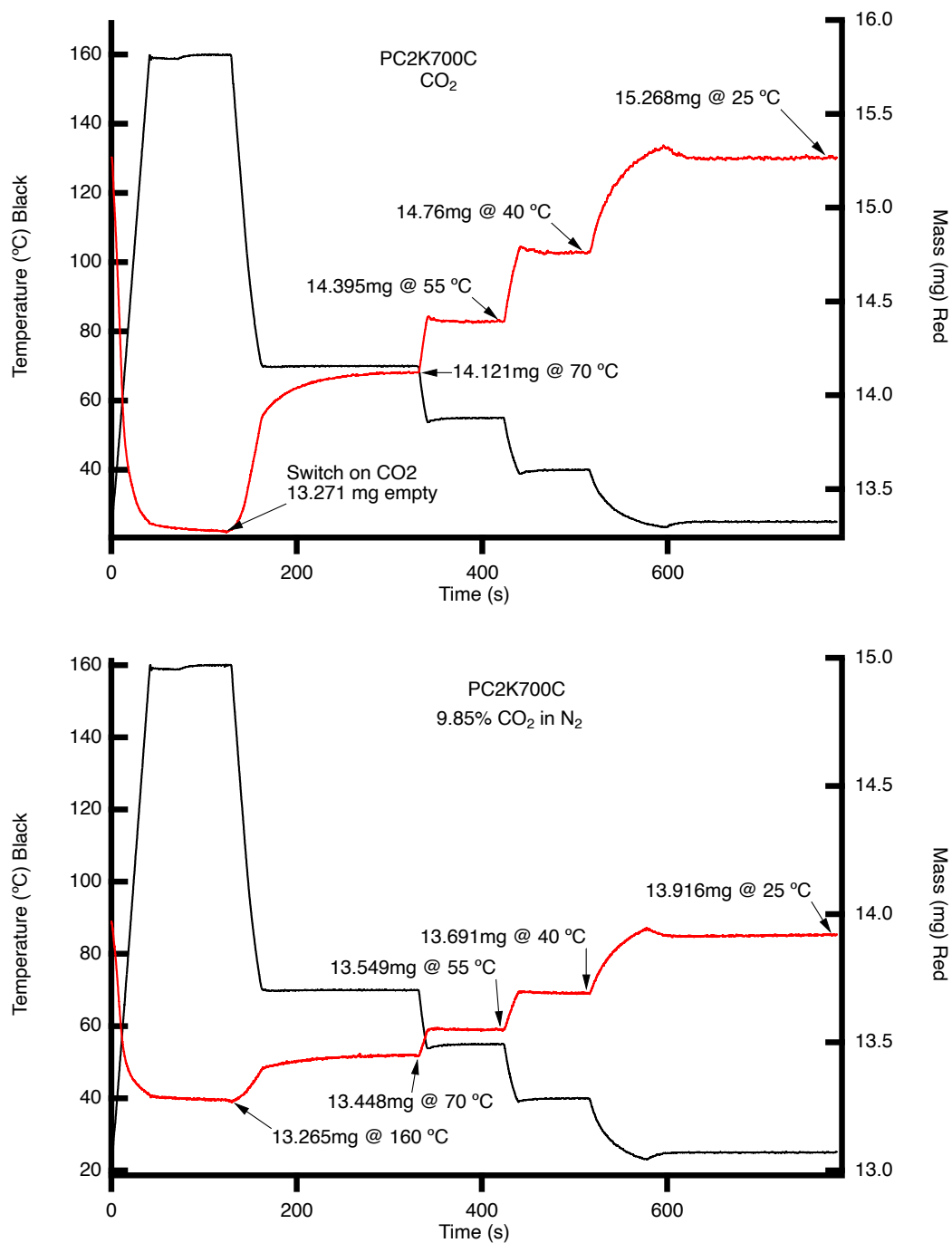
[2] R. Ben-Mansour, M. A. Habib, O. E. Bamidele, M. Basha, N. A.A. Qasem, A. Peedikakkal, T. Laoui, and M. Ali. Carbon capture by physical adsorption: Materials, experimental investigations and numerical modeling and simulations - A review. *Applied Energy*, 161:225–255, 1 2016. ISSN 03062619. doi: 10.1016/j.apenergy.2015.10.011.

[3] Sangil Han, Yougui Huang, Taku Watanabe, Sankar Nair, Krista S. Walton, David S. Sholl, and J. Carson Meredith. MOF stability and gas adsorption as a function of exposure to water, humid air, SO2, and NO2. *Microporous and Mesoporous Materials*, 173:86–91, 2013. ISSN 13871811. doi: 10.1016/j.micromeso.2013.02.002.

[4] Anne Andersen, Swapnil Divekar, Soumen Dasgupta, Jasmina Hafizovic Cavka, A. Aarti, Anshu Nanoti, Aud Spjelkavik, Amar N. Goswami, M. O. Garg, and Richard Blom. On the development of Vacuum Swing adsorption (VSA) technology for post-combustion CO2 capture. In *Energy Procedia*, volume 37, pages 33–39. Elsevier Ltd, 2013. doi: 10.1016/j.egypro.2013.05.082.

[5] Hayden A. Evans, Dinesh Mullangi, Zeyu Deng, Yuxiang Wang, Shing Bo Peh, Fengxia Wei, John Wang, Craig M. Brown, Dan Zhao, Pieremanuele Canepa, and Anthony K. Cheetham. Aluminum formate, Al(HCOO)3: An earth-abundant, scalable, and highly selective material for CO2 capture. *Science Advances*, 8(44):1473, 11 2022. ISSN 23752548. doi: 10.1126/sciadv.ade1473. URL `https://www.science.org/doi/10.1126/sciadv.ade1473`.

[6] Jian Bin Lin, Tai T.T. Nguyen, Ramanathan Vaidhyanathan, Jake Burner, Jared M. Taylor, Hana Durekova, Farid Akhtar, Roger K. Mah, Omid Ghaffari-Nik, Stefan Marx, Nicholas Fylstra, Simon S. Iremonger, Karl W. Dawson, Partha Sarkar, Pierre Hovington, Arvind Rajendran, Tom K. Woo, and George K.H. Shimizu. A scalable metal-organic framework as a durable physisorbent for carbon dioxide capture. *Science*, 374(6574):1464–1469, 12 2021. ISSN 10959203. doi: 10.1126/science.abi7281. URL `https://www.science.org/doi/10.1126/science.abi7281`.

[7] J. Przepiórski, M. Skrodzewicz, and A. W. Morawski. High temperature ammonia treatment of activated carbon for enhancement of CO 2 adsorption. *Applied Surface Science*, 225(1-4):235–242, 3 2004. ISSN 01694332. doi: 10.1016/j.apsusc.2003.10.006.

[8] Dipendu Saha, Scott E. Van Bramer, Gerassimos Orkoulas, Hoi Chun Ho, Jihua Chen, and Dale K. Henley. CO2 capture in lignin-derived and nitrogen-

doped hierarchical porous carbons. *Carbon*, 121:257–266, 9 2017. ISSN 0008-6223. doi: 10.1016/J.CARBON.2017.05.088.

[9] Mohammad Saleh Shafeeyan, Wan Mohd Ashri Wan Daud, Amirhossein Houshmand, and Arash Arami-Niya. Ammonia modification of activated carbon to enhance carbon dioxide adsorption: Effect of pre-oxidation. *Applied Surface Science*, 257(9):3936–3942, 2 2011. ISSN 0169-4332. doi: 10.1016/J.APSUSC.2010.11.127.

[10] Jie Chen, Jie Yang, Gengshen Hu, Xin Hu, Zhiming Li, Siwei Shen, Maciej Radosz, and Maohong Fan. Enhanced CO2 Capture Capacity of Nitrogen-Doped Biomass-Derived Porous Carbons. *ACS Sustainable Chemistry and Engineering*, 4(3):1439–1445, 3 2016. doi: 10.1021/ACSSUSCHEMENG. 5B01425.

[11] Long-Yue Meng and Soo-Jin Park. Investigation of narrow pore size distributions on carbon dioxide capture. *Bull. Korean Chem. Soc*, 33(11):3749, 2012. doi: 10.5012/bkcs.2012.33.11.3749. URL http://dx.doi.org/10.5012/bkcs.2012.33.11.3749.

[12] Xin Hu, Maciej Radosz, Katie A Cychosz, and Matthias Thommes. CO2-filling capacity and selectivity of carbon nanopores: Synthesis, texture, and pore-size distribution from Quenched-Solid Density Functional Theory (QSDFT). *Environ. Sci. Technol*, 45:7068–7074, 2011. doi: 10.1021/es200782s.

[13] Lindsey Ortiz. Computational studies of methane adsorption in nanoporous carbon. *Masters of Science Thesis, University of Missouri-Columbia*, 2012. URL https://mospace.umsystem.edu/xmlui/handle/10355/33157.

[14] Ting Yang and Aik Chong Lua. Characteristics of activated carbons prepared from pistachio-nut shells by potassium hydroxide activation. *Microporous and Mesoporous Materials*, 63(1-3):113–124, 9 2003. ISSN 13871811. doi: 10.1016/S1387-1811(03)00456-6.

[15] Chi Chang Hu, Chen Ching Wang, Feng Chin Wu, and Ru Ling Tseng. Characterization of pistachio shell-derived carbons activated by a combination of KOH and CO2 for electric double-layer capacitors. *Electrochimica Acta*, 52(7): 2498–2505, 2 2007. ISSN 00134686. doi: 10.1016/j.electacta.2006.08.061.

[16] Jun Seok Bae and Shi Su. Macadamia nut shell-derived carbon composites for post combustion CO2 capture. *International Journal of Greenhouse Gas Control*, 19:174–182, 11 2013. ISSN 17505836. doi: 10.1016/j.ijggc.2013. 08.013.

[17] Hacer Dolas, Omer Sahin, Cafer Saka, and Halil Demir. A new method on producing high surface area activated carbon: The effect of salt on the surface area and the pore size distribution of activated carbon prepared from pistachio shell. *Chemical Engineering Journal*, 166(1):191–197, 1 2011. ISSN 13858947. doi: 10.1016/j.cej.2010.10.061.

[18] Cagdas Okutucu, Gozde Duman, Suat Ucar, Ihsan Yasa, and Jale Yanik. Production of fungicidal oil and activated carbon from pistachio shell. *Journal of Analytical and Applied Pyrolysis*, 91(1):140–146, 5 2011. ISSN 01652370. doi: 10.1016/j.jaap.2011.02.002.

[19] K. Y. Foo and B. H. Hameed. Preparation and characterization of activated carbon from pistachio nut shells via microwave-induced chemical activation. *Biomass and Bioenergy*, 35(7):3257–3261, 7 2011. ISSN 09619534. doi: 10.1016/j.biombioe.2011.04.023.

[20] Krista S. Walton and David S. Sholl. Predicting multicomponent adsorption: 50 years of the ideal adsorbed solution theory. *AIChE Journal*, 61(9):2757–2762, 9 2015. ISSN 15475905. doi: 10.1002/aic.14878. URL `https://onlinelibrary.wiley.com/doi/full/10.1002/aic.14878`.

[21] Masoud Mofarahi and Fatemeh Gholipour. Gas adsorption separation of CO2/CH4 system using zeolite 5A. *Microporous and Mesoporous Materials*, 200:1–10, 12 2014. ISSN 13871811. doi: 10.1016/j.micromeso.2014.08.022.

[22] Jarad A. Mason, Thomas M. McDonald, Tae Hyun Bae, Jonathan E. Bachman, Kenji Sumida, Justin J. Dutton, Steven S. Kaye, and Jeffrey R. Long. Application of a high-throughput analyzer in evaluating solid adsorbents for post-combustion carbon capture via multicomponent adsorption of CO2, N2, and H2O. *Journal of the American Chemical Society*, 137(14):4787–4803, 2015. ISSN 15205126. doi: 10.1021/jacs.5b00838.

[23] Xuqing Cai, Farhad Gharagheizi, Lukas W. Bingel, Danny Shade, Krista S. Walton, and David S. Sholl. A collection of more than 900 gas mixture adsorption experiments in porous materials from literature meta-analysis. *Industrial and Engineering Chemistry Research*, 60(1):639–651, 1 2021. ISSN 15205045. doi: 10.1021/acs.iecr.0c05398. URL `https://pubs.acs.org/doi/full/10.1021/acs.iecr.0c05398`.

[24] Pierre Billemont, Nicolas Heymans, Périne Normand, and Guy De Weireld. IAST predictions vs co-adsorption measurements for CO2 capture and separation on MIL-100 (Fe). *Adsorption*, 23(2-3):225–237, 4 2017. ISSN 15728757. doi: 10.1007/s10450-016-9825-6. URL `https://link.springer.com/article/10.1007/s10450-016-9825-6`.

[25] J. Raziel Álvarez, Elí Sánchez-González, Eric Pérez, Emilia Schneider-Revueltas, Ana Martínez, Adriana Tejeda-Cruz, Alejandro Islas-Jácome, Eduardo González-Zamora, and Ilich A. Ibarra. Structure stability of HKUST-1 towards water and ethanol and their effect on its CO2 capture properties. *Dalton Transactions*, 46(28):9192–9200, 7 2017. ISSN 14779234. doi: 10.1039/c7dt01845b.

[26] Cory M. Simon, Berend Smit, and Maciej Haranczyk. PyIAST: Ideal adsorbed solution theory (IAST) Python package. *Computer Physics Communications*, 200:364–380, 3 2016. ISSN 00104655. doi: 10.1016/j.cpc.2015.11.016. URL `https://www.sciencedirect.com/science/article/pii/S0010465515004403`.

[27] Cullen M Quine. REALIST, 6 2023. URL `https://github.com/cullenmq/REALIST`.

[28] Jacek Jagiello and Jeffrey Kenvin. Consistency of carbon nanopore characteristics derived from adsorption of simple gases and 2D-NLDFT models. Advantages of using adsorption isotherms of oxygen (O2) at 77 K. *Journal of Colloid and Interface Science*, 542:151–158, 4 2019. ISSN 10957103. doi: 10.1016/j.jcis.2019.01.116.

[29] A. L. Myers and J. M. Prausnitz. Thermodynamics of mixed-gas adsorption. *AIChE Journal*, 11(1):121–127, 1 1965. ISSN 15475905. doi: 10.1002/aic.690110125. URL `https://onlinelibrary.wiley.com/doi/full/10.1002/aic.690110125`.

[30] Ian H. Bell, Jorrit Wronski, Sylvain Quoilin, and Vincent Lemort. Pure and pseudo-pure fluid thermophysical property evaluation and the open-source thermophysical property library coolprop. *Industrial and Engineering Chemistry Research*, 53(6):2498–2508, 2014. ISSN 08885885. doi: 10.1021/ie4033999. URL `https://pubs.acs.org/doi/10.1021/ie4033999`.

[31] Danny Shade, Brandon W.S. Bout, David S. Sholl, and Krista S. Walton. Opening the toolbox: 18 experimental techniques for measurement of mixed gas adsorption. *Industrial and Engineering Chemistry Research*, 2022, 2367. doi: 10.1021/acs.iecr.1c03756. URL `https://doi.org/10.1021/acs.iecr.1c03756`.

[32] Polarizabilities of atoms and molecules. In John R. Rumble, editor, *Handbook of Chemistry and Physics*. CRC Press/Taylor & Francis, Boca Raton, FL, 103rd edition, 2022. URL `https://hbcp.chemnetbase.com/faces/documents/10_04/10_04_0014.xhtml`.

Chapter 6

CONCLUSION

6.1 Summary of Results

The work described in this thesis focused on the tunability of gas binding strength in carbonaceous adsorbent materials. Two different methodologies were investigated: one modifying the surface chemistry of carbon adsorbents for ambient temperature storage and the other focusing on structural changes to the underlying pore structure (see Fig. 6.1). To characterize these systems, statistical mechanical models were developed and implemented in a Python package to extract relevant thermodynamic quantities.
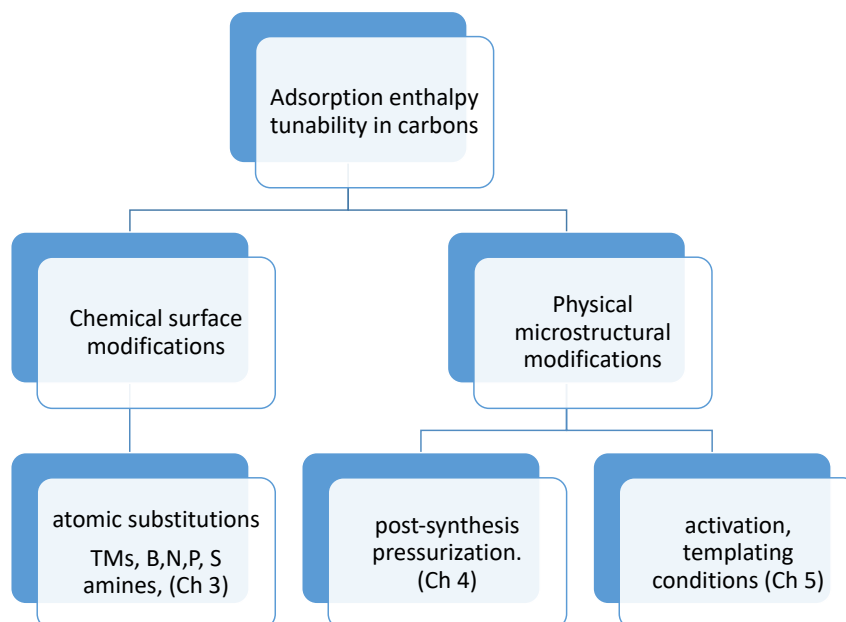

Figure 6.1: Outline of different potential techniques to tune adsorption enthalpies in carbon adsorbents. Chapter 3 focused on transition metal (TM) copper additions, Chapter 4 on post-synthesis pelletization pressures, and Chapter 5 on changes in activation conditions.

The first material system incorporated metal additions to a commercial carbon to improve the ambient temperature storage of hydrogen in carbon materials. Through temperature programmed desorption experiments, it was shown that a new desorption feature existed in the metal-modified material, showing hydrogen desorption near ambient temperature. Further investigation with isotope mixing experiments established that the addition of copper clusters to the super-activated carbon resulted in an activated chemisorption process due to dissociation of the hydrogen molecule. A double-site isotherm model was established to decouple the physisorption from the chemisorption uptake, and adsorption enthalpies were extracted. The modified material showed significant improvement over the unmodified material at low pressures, ambient temperature due to the copper additions (binding energies of 20 kJ/mol for the copper sites compared to 6 kJ/mol for the underlying carbon structure), however clustering of the copper reduced the overall surface area and the overall enhancement to the total enthalpy of adsorption.

Zeolite-templated carbons were synthesized and pelletized using a hot-pressing technique with reduced-graphene oxide as a binder. This improved the bulk density of the material over powder packing. Furthermore, the total volumetric uptake was higher than expected for an ideal specimen of the material. It was shown that the pore structure in the material was altered as a result of pelletization due to the unusual elastic nature of the material, resulting in smaller pores. This hypothesis was supported with pore size distributions of the monolithic samples, showing both increased bulk densities and smaller average pore diameter with increasing pelleti-

zation pressure Adsorption uptake with thermodynamic analysis showed that the enthalpies of adsorption increased with pressurization of the material, establishing the use of pressure as a mechanism to tune the binding strength of gases in post-synthesis of the material. This is an unusual material property attributed to the unique structure of zeolite-templated carbon over conventional activated carbons. Methane adsorption enthalpies increased from 14.5 kJ/mol in the pristine powder sample to over 18 kJ/mol in ZTC P7.

Pistachio shell-derived activated carbons were synthesized using chemical activation with potassium hydroxide. Two materials were made with a different distribution of pores, and compared to a commercial carbon. Instead of post-synthesis tuning of the pore structure, a direct approach of tuning the development of porosity during activation was investigated. Higher activation temperatures and ratio of activation agent resulted in higher specific surface areas, with an increased density of larger pores. The selectivity of carbon dioxide over nitrogen was shown to be higher for the lower surface area carbon, due to higher enthalpies of adsorption for carbon dioxide. Carbon dioxide adsorption enthalpies ranged from 20 kJ/mol to over 24 kJ/mol depending on the degree of activation. While all of the carbon materials exhibited similar carbon dioxide uptake at low pressures, the lower surface area carbon also showed significantly lower nitrogen uptake than the other studied materials, resulting in its increased carbon dioxide selectivity. Thermodynamic analysis showed that the sensitivity of enthalpies of adsorption increased with the polarizability of the gas, which is consistent with theoretical results.

6.2   Future Work

Single Atom Metal Centers on Carbons

While the copper-modified commercial activated carbon showed improved uptake at ambient temperature conditions, specific surface area was reduced due to pore-blocking and development of nano-clusters of copper. Recent work has shown that nitrogen functionalization of activated carbons is effective at pinning down metal sites on supported carbon frameworks. Using these approaches to develop metal functionalized activated carbon using nitrogen for metallic atom pinning could prevent the setbacks mentioned above. It would be of scientific interest to investigate the heat of adsorption changes due to metal-nitride bonds instead of metal clusters, and to determine if the adsorption process is dissociative in nature.

Experimental Investigations into Langmuir Equation Temperature Dependencies

As outlined in this thesis, the "K" Langmuir constant has both an exponential temperature dependence and a power law prefactor temperature dependence, the latter depending on the adsorbed state partition function. The power law term does not significantly change the goodness of fits, but does have an effect on the isosteric heat of adsorption temperature dependence. Furthermore, the adsorbed gas density is assumed to be constant over all temperatures and pressures, which may not be valid in different adsorption regimes, especially if the adsorbed gas dimensionality changes. There are two approaches to experimentally determine the temperature dependence of this prefactor:

- Experimental investigations into the nature of the adsorbed state for a specific adsorbate and adsorbent system over the temperature and pressure range of interest.

- Accurate and precise direct measurements of the heats of adsorption as a function of temperature and pressure.

Unfortunately, both of these experimental approaches require substantial commitments in both time and resources. The adsorbed state investigation requires either EELS measurements or neutron scattering data. To characterize an adsorbent system, both quasielastic neutron scatering (QENS) to determine the dimensionality of the adsorbed state and inelastic neutron scattering to determine the vibrational energy of different adsorption modes would be necessary. The precise heat of adsorption measurements would be suitable with a Calvet Calorimeter. Current commercial versions of these systems however do not possess high enough accuracy to discern between the different partition function models. A custom apparatus that functions at constant uptake (isosteric measurements) using pressure feedback control on a gravimetric Sieverts apparatus with a temperature ramp could provide a direct method of measuring the latent heat with temperature using the Clausius equation, and would operate similarly to a conventional calorimeter. Constant uptake measurements are notoriously challenging, and would require ultra-fast real-time buoyancy corrections.

Improvement of Mixed Gas Isotherm Predictions and Experimental Measurements

The Ideal Adsorption Solution Theory Python package developed through the work in this thesis improves on a highly used Python package (pyIAST), incorporating both fugacity and universal Langmuir isotherm models to fit experimental excess pure-component adsorption data. However, there are many improvements that have not yet been incorporated into the model. Multiple isotherm models that fit multiple isotherms over a large range of temperatures (such as the Unilan, Sips, toth isotherm models) need to be added to the REALIST adsorption package. While the IAST model can predict experimental mixed-gas excess measurements at low pressure, the package does not account for absolute vs. excess mixed-gas measurements. The predictions are given as absolute uptake data, however this prediction will deviate from the experimental excess measurements at higher pressures. For pure gases, excess measurements can be converted to absolute through adsorbed phase density fitting. With mixed-gas adsorbents, and potentially different adsorbed gas densities, the problem of accounting for the adsorbed gas volume becomes more challenging.

To evaluate the effectiveness of the mixed-gas predictions, including the high pressure uptake conditions mentioned above, accurate measurements of mixed-gas adsorption will need to be conducted over a large range of adsorbent systems. These measurements take significantly more time than their pure-gas counterparts, as the sample needs to be evacuated between each pressure and temperature measurement. Without gas flow and constant volume measurements, the gas phase composition

will change after each adsorption step. Recently, a review paper has investigated the current experimental techniques for mixed-gas adsorption.[1] One of the more promising techniques, known as the integral mass balance (IMB) system involves the combination of a gravimetric balance to measure the total mixed-gas adsorption with a simple breakthrough (SB) apparatus to measure the fractional uptake of each adsorbate. Our work used a thermogravimetric analyzer (TGA) as the gravimetric balance, however pressures were limited to near-ambient. Combination of a high-pressure gravimetric Sieverts apparatus with a simple breakthrough analyzer would increase the pressure range of measurements, and further automation of this apparatus would allow for increased experimental throughput.

Broader Outlook

In addition to improving the fundamental science needed to model gas adsorption, advancements in materials synthesis commercialization will need to be pursued. The demand for highly tuned adsorbents to filter exhaust streams and to transport gases will most likely increase in the 21st century. Many polluting gas streams will need to be filtered in a more effective manner (both in selectivity and in reduced cost) than what has been traditionally accepted. Furthermore, gas pipelines that transport gas streams of interest for carbon neutrality such as carbon dioxide to sequestration sites, or hydrogen and ammonia for energy storage, will receive atypical bipartisan push-back due to cost, renewable infrastructure reluctance, and environmental concerns. Adsorbent materials offer solutions to both gas filtration and transport, reducing pressurization costs for transport and energy costs

for filtration. A diverse set of adsorbent materials will need to be tailored for each application, that optimizes the structure (and the corresponding adsorption enthalpy) needed for different gas compositions, temperatures, and pressures. Metal-organic frameworks (MOFs) offer the tunability required for such applications, and novel emerging structures such as breathing frameworks have been recently discovered, which improve deliverable gas uptakes. Many novel structures that have been synthesized in recent years have focused on breaking arbitrary existing records, while the primary driver for technology adoption also includes system and operating costs. Techno-economic studies of low-cost commercialization of MOFs, or to identify existing potentially low-cost MOFs that have reasonable performance metrics, should be pursued with clear applications identified for gas filtration. At the same time, carbon adsorbents have historically been low-cost, and through this work have been shown to have sufficient microstructural tunability for effective methane and carbon dioxide adsorbed storage. New techniques that offer increased microstructural tunability at scales of technological interest should be commercially pursued for carbon adsorbents to address the gas transport demands of the upcoming decades.

References

[1] Danny Shade, Brandon W.S. Bout, David S. Sholl, and Krista S. Walton. Opening the toolbox: 18 experimental techniques for measurement of mixed gas adsorption. *Industrial and Engineering Chemistry Research*, 2022, 2367. doi: 10.1021/acs.iecr.1c03756. URL https://doi.org/10.1021/acs.iecr.1c03756.

A p p e n d i x   A

DETERMINATION OF PORE SIZE DISTRIBUTIONS

One of the most important structural properties for adsorption in porous materials is the pore size distribution, and the resulting pore volume and surface area. This thesis has investigated the use of both chemical surface functionalization and pore morphology changes to tune adsorption phenomena, however determination of the pore structure and size in a microporous adsorbent is in itself an active field of research. While pore structure determination is not the primary focus of this dissertation, a brief overview and insight into the current state of the field will be presented here.

A commonly utilized technique for microstructural determination of porous materials utilizes probe gas molecules, generally near the saturation pressure p_0 of the adsorbate, which include Ar, N_2, CO_2, O_2, and H_2. Each of these molecules have different kinetic diameters and polarizability constants, making them suitable for different ranges in pore size. Pore sizes in adsorbent materials are characterized into four main groups: ultramicropores ($<10\,\text{Å}$), micropores ($10\text{-}20\,\text{Å}$), mesopores ($20\text{-}500\,\text{Å}$) and macropores $>500\,\text{Å}$. The IUPEC standard for pore structure characterization porous materials is Ar at 87 K (liquid argon bath) due to the size of Ar as a probe molecule, and the relative insensitivity of argon to surface functional groups compared to other adsorbates. Argon measurements are suitable for a large range in pore sizes, from ultramicropores to mesopores. The feasibility of conducting experiments at liquid argon temperatures (due to the availability of liquid argon or
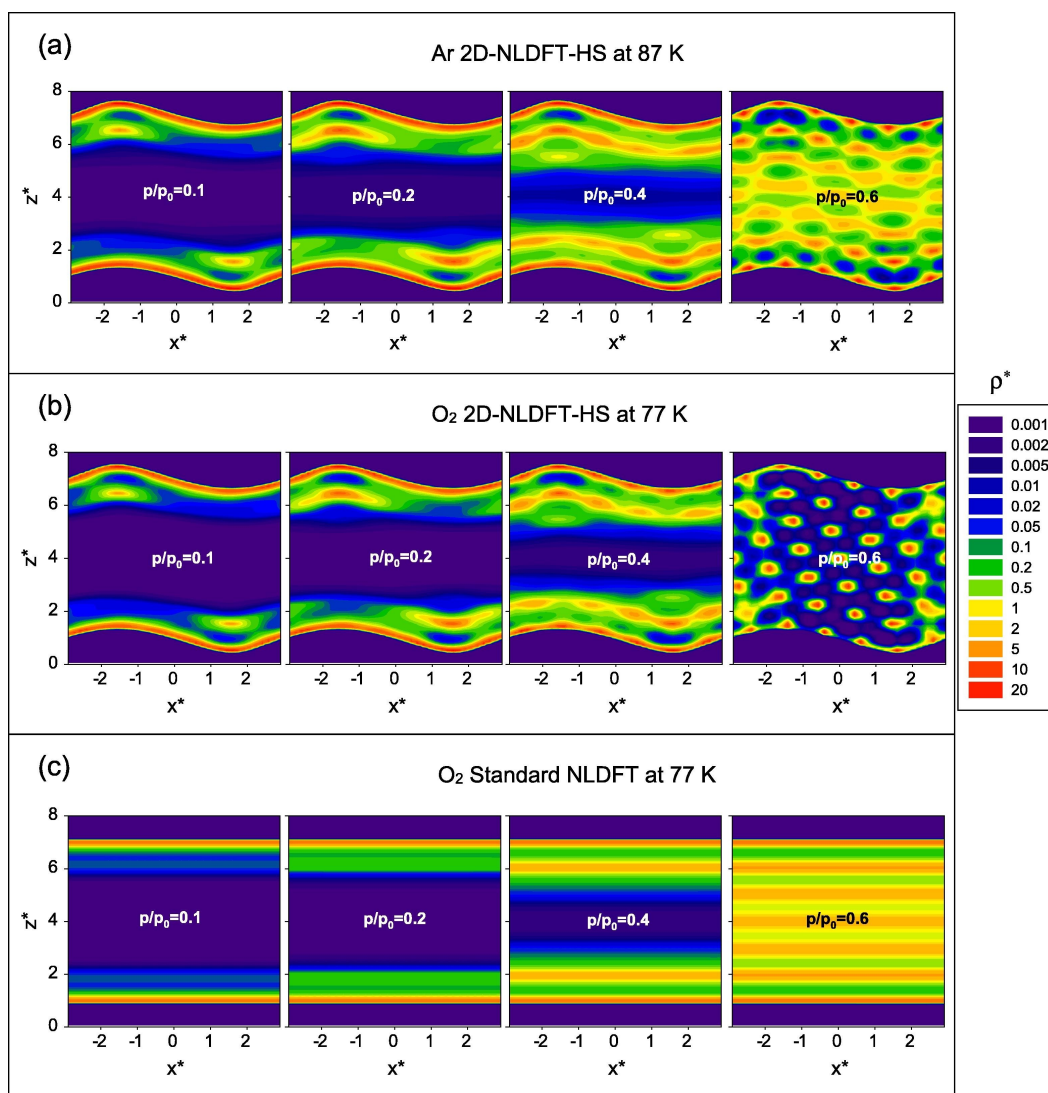
Figure A.1: NLDFT gas density calculations as a function of pressure in material cross-sections of Ar at 87 K in a heterogeneous surface (a), O_2 at 77 K in a heterogeneous surface (b) and a flat surface (c). Reproduced with permission from the copyright holder, Elsevier.[1]

cryostats) makes this method unsuitable for many laboratories and high-thoroughput experiments. The pore size distribution is determined by fitting the experimentally measured gas uptake with weights of gas uptake in individual pores. The pore size distribution kernel is essential in the determination of pore size distributions and is the gas density (in mmol/mL) as a function of pressure for each individual
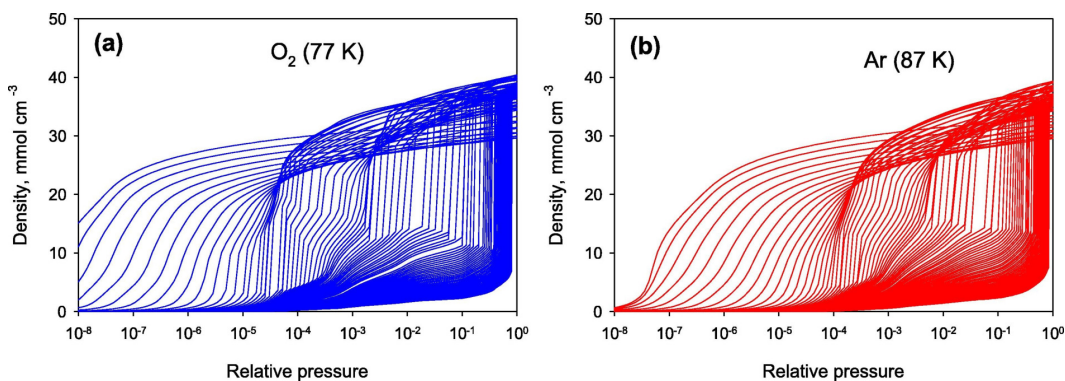
Figure A.2: NLDFT-HS slit-pore carbon kernels with pore widths from 3.6-100 Å for O_2 at 77 K (a) and Ar at 87 K (b). Reproduced with permission from the copyright holder, Elsevier.[1]

pore size. Recent work has been conducted in developing kernels using computational methods with accurate models of the gas density in pores for different probe molecules. Non-local density functional theory (NLDFT) methods for pore size determination have been actively developed for several decades. Recent iterations of these models include heterogeneous surface computations to account for rough surfaces in slit-pore carbons (such as KOH-activated carbon).[2, 1, 3] A comparison of the gas density in a flat slit pore and heterogeneous surface slit pore for different pressure loadings is shown in Fig. A.1. The NLDFT-HS kernel for O_2 at 77 K, Ar at 87 K, and CO_2 at 273 K is shown in Fig. A.2a, Fig. A.2b, and Fig. A.3a, respectively.

Certain probe gas molecules are better suited for certain ranges of pore size. Generally, nitrogen at 77 K is used for pore size distribution measurements due to the low cost and availability of liquid nitrogen. The relatively large size of nitrogen and its high polarizability, and sensitivity to surface functional groups, makes pore structure determination below 10 Å challenging, and inaccurate without high precision pressure transducers in state-of-the-art equipment. CO_2 at 273 K has
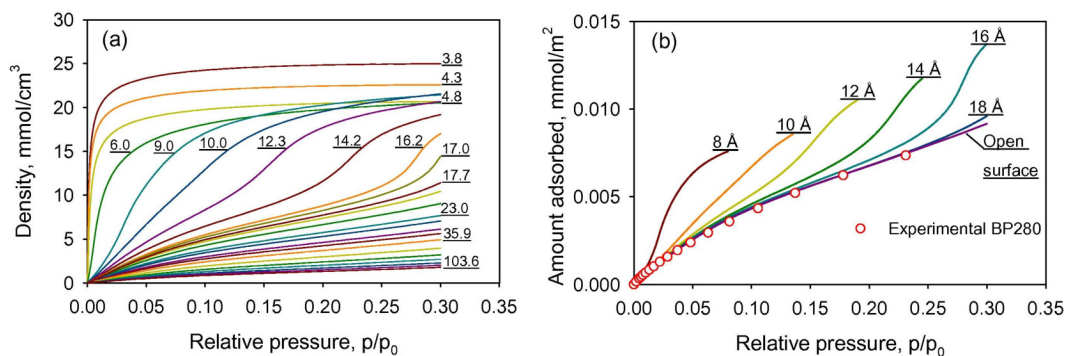
Figure A.3: NLDFT-HS Kernel for CO_2 at 273K (a) with pore widths labelled in A and adsorption amount per area (b) relative to a infinite-width pore (open surface).Reproduced with permission from the copyright holder, Elsevier.[3]

a low molecular diameter (due to the rod-like nature of the molecule), making it especially useful for accurate determination of ultramicropores over more reasonable pressure conditions than with N_2 or Ar. However, the models only support up to 10 bar (p/p_0=0.3), as adsorption measurements above this pressure begin to converge on the uptake of an infinite pore width (see Fig. A.3b), limiting pore determination to below 18 Å with carbon dioxide.[3] The maximum pressure of most commercial equipment is generally around 1 bar, limiting pore size determination to 10 Å.[4] Hydrogen as a probe molecule at 77 K faces many of the same challenges and obstacles as CO_2 for ultramicropore determination, with lower polarizability (and smaller diameter) than CO_2.

Recently, efforts have been made to combine the ultramicropore information from CO_2 or H_2 measurements with the micropore and mesopore information from N_2 or O_2 measurements to obtain accurate, full range pore size distribution information. This technique, called dual gas NLDFT, is currently implemented in Micromeritics' Microactive software, with specific emphasis on N_2/CO_2 and (more

Table A.1: Comparison of NLDFT, Langmuir, and BET Specific Surface Areas

Name	BET, N_2 m^2/g	NLDFT, N_2 m^2/g	NLDFT, N_2CO_2 m^2/g	BET, Ar m^2/g	NLDFT, Ar m^2/g	NLDFT, CO_2 m^2/g	Lang, CO_2 m^2/g
PC3K800C	2460	1950	2420	2450	1950	2340	2920
MSP20	2080	1730	2200	2060	1930	2070	2370
PC2K700C	1240	1310	1740	1250	1260	1530	1300

recently) O_2/H_2.[3, 5] Compared with the CO_2/N_2 pair, the lower polarizability and probe molecule size of the O_2/H_2 pair shows improvement with ultramicropores and insensitivity to polar surface groups.[5] Due to safety regulations around placing hydrogen tanks near oxygen tanks, and the availability of high resolution and high pressure CO_2 isotherms at 273 K in this dissertation, only the N_2/CO_2 isotherm pair was investigated.

Table A.1 shows the specific surface area values calculated with the NLDFT, BET, or Langmuir fits. The BET Ar surface area values are very similar to BET N_2 data. The NLDFT values, however, are more varying. Relative to the BET measurements, the N_2 NLDFT values are lower for PC3K and MSP20, and slightly higher for PC2K700C. While the NLDFT for the dual gas fit is close to the BET values for PC3K and MSP20, it is an outlier for the PC2K700C material, which is primarily ultramicroporous. The NLDFT Ar values are more in agreement with the BET measurements than the NLDFT N_2 values. The Langmuir fit of CO_2 overestimates the surface area for all three materials relative to the BET measurements, and deviates more for PC3K800C, which has the highest surface area and the largest average pore size.

The pore size distributions calculated with each technique for the materials
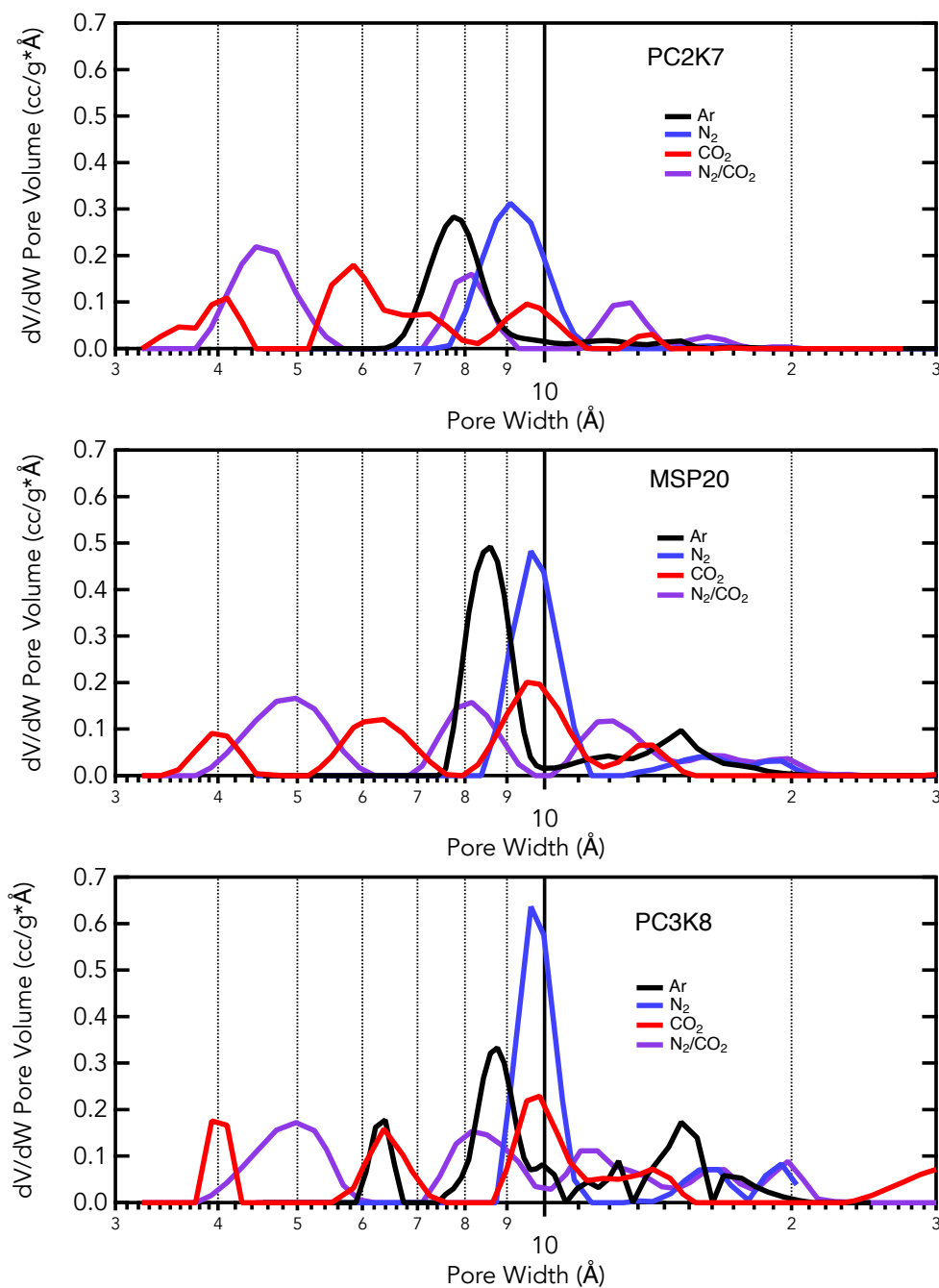
Figure A.4: Pore size distributions of PC2K700C (top), MSP20 (middle), and PC3K800C (bottom) calculated with 87 K Ar NLDFT-HS (black), 77 K N_2 NLDFT-HS (blue), 273 K CO_2 NLDFT-HS (red), and 77 K N_2/273 K CO_2 dual NLDFT-HS (purple).

described in Chapter 5 are shown in Fig. A.4. The nitrogen pore size distributions show a peak around $10\,\text{Å}$ for all samples, which area is proportional to the sum of ultramicropore area, when compared to the other techniques. This demonstrates the inability of the N_2 PSD to characterize ultramicropores without high resolution transducers. The Ar data shows improved ultramicroporous information over N_2, with the smallest pore feature around 6.5Å, which matches with the CO_2 data. The CO_2, while providing more ultramicropore information, fails to account for pores above 15Å, which is expected from the limitations of the model. These insights into single-gas NLDFT pore size determination are in agreement with studies on metal-organic framework materials. The N_2/CO_2 dual gas fit has pore features around the same pore sizes as the Ar calculations, with some additional features below $6\,\text{Å}$. However, the actual pore features in the dual calculation shift by 1-$2\,\text{Å}$ when compared to the Ar calculations. Overall, the dual gas fitting shows promise, especially with an extended range over single-component NLDFT calculations, but requires further refining to replace $87\,\text{K}$ Ar NLDFT-HS distributions.

References

[1] Jacek Jagiello and Jeffrey Kenvin. Consistency of carbon nanopore characteristics derived from adsorption of simple gases and 2D-NLDFT models. Advantages of using adsorption isotherms of oxygen (O2) at 77 K. *Journal of Colloid and Interface Science*, 542:151–158, 4 2019. ISSN 10957103. doi: 10.1016/j.jcis.2019.01.116.

[2] Jacek Jagiello and James P. Olivier. Carbon slit pore model incorporating surface energetical heterogeneity and geometrical corrugation. *Adsorption*, 19(2-4): 777–783, 4 2013. ISSN 09295607. doi: 10.1007/s10450-013-9517-4. URL `https://link.springer.com/article/10.1007/s10450-013-9517-4`.

[3] Jacek Jagiello, Conchi Ania, Jose B. Parra, and Cameron Cook. Dual gas analysis of microporous carbons using 2D-NLDFT heterogeneous surface model and combined adsorption data of N2 and CO2. *Carbon*, 91:330–337, 9 2015. ISSN 0008-6223. doi: 10.1016/J.CARBON.2015.05.004.

[4] Peter I Ravikovitch, Aleksey Vishnyakov, Ron Russo, and Alexander V Neimark. Unified approach to pore size characterization of microporous carbonaceous materials from N2, Ar, and CO2 adsorption isotherms. *Langmuir*, 16(5):2311–2320, 2000. ISSN 07437463. doi: 10.1021/la991011c.

[5] Jacek Jagiello, Jeffrey Kenvin, Conchi O. Ania, Jose B. Parra, Alain Celzard, and Vanessa Fierro. Exploiting the adsorption of simple gases O2 and H2 with minimal quadrupole moments for the dual gas characterization of nanoporous carbons using 2D-NLDFT models. *Carbon*, 160:164–175, 4 2020. ISSN 00086223. doi: 10.1016/j.carbon.2020.01.013.